Surface and electrical properties of GaN layers – Impact on GaN/AlInN FETs

Dissertation
zur Erlangung des akademischen Grades
doctor rerum naturalium
(Dr. rer. nat.)

genehmigt durch die Fakultät für Naturwissenschaften
der Otto-von-Guericke-Universität Magdeburg

von M.Sc. Phys. Aqdas Fariza
geb. am 14.01.1983 in Jhelum

Gutachter: apl. Prof. Dr. Armin Dadgar
Prof. Dr.-Ing. Thomas Mikolajick

eingereicht am: 07. Juni 2018
verteidigt am: 15. Februar 2019

Kurzfassung

Wegen ihrer vielversprechenden Eigenschaften, wie der großen Bandlücke, der hohen Durchbruchfeldstärke und Heterostrukturen, mit denen sich zweidimensionale Elektronengase erzeugen lassen, ist die Gruppe der Nitrid-basierte Halbleiter für Leistungselektronik-Anwendungen geeignet. Allerdings begrenzen Zuverlässigkeitsprobleme durch die Anwesenheit von Versetzungen und anderer nativer Defekte immer noch die Leistung von GaN-basierten Bauelementen, zum Beispiel aufgrund von hohen Gate-Leckströmen und einem früheren Durchbruch der Bauteile. In dieser Arbeit werden wesentliche Materialeigenschaften von MOVPE-gewachsenen GaN-Puffern und FET-Strukturen untersucht, die die Grundlage für das Verständnis der Leistungsfähigkeit dieser Bauelemente bilden.

Oberflächenpotentialstudien an semi-isolierenden GaN-Schichten zeigten, dass die durch Kohlenstoff eingeführten Akzeptorzustände bei einem C-Dotierungsniveau von über 1.6×10^{18} cm^{-3} ein Fermi-Level-Pinning unterhalb der Bandlückenmitte verursachen, während die Akzeptorzustände durch Eisenverunreinigungen energetisch immer oberhalb der Bandlückenmitte liegen. Der negative Oberflächenpotentialkontrast von Versetzungen, der in kohlenstoffdotierten GaN-Proben beobachtet wird, erhöht sich mit der Kohlenstoffkonzentration, während die Versetzungen in Fe-dotierten GaN-Proben einen neutralen oder nur schwach negativen Ladungskontrast unabhängig vom Dotierungsgehalt zeigen.

Bei der Untersuchung von GaN:C- und GaN:Fe-Schichten, die in GaN/AlGaN- und GaN/AlN/AlInN-FETs als hochohmige Puffer verwendet werden, zeigte sich, dass durch eine Kohlenstoffdotierung geringere Leckströme in vertikaler und lateraler Richtung erzielt und die Durchbruchspannungen und -feldstärken im Vergleich zu Eisen verbessert werden. Vertikale Transportmessungen zeigen, dass Kohlenstoff-dotierte GaN-Schichten mit einer Dotierstoffkonzentration von $4.6\text{x}10^{18}$ cm^{-3} einen um bis zu fünf Größenordnungen niedrigeren Dunkelstrom bei Raumtemperatur und eine signifikant höhere thermische Aktivierungsenergie aufweisen als Fe-dotierte Proben mit einer vergleichbaren Dotierkonzentration. AlInN- und AlGaN-basierte FETs mit C-dotierten Puffern bieten zudem höhere Durchbruchsspannungen als Strukturen mit Fe-dotierten Puffern. Dabei beträgt die elektrische Feldstärke etwa 2.6×10^{6} V/cm für laterale Pufferleckströme und über $2.4\text{x}10^{6}$ V/cm bei vertikaler Kontaktanordnung. Im Gegensatz dazu beträgt die Durchbruchfeldstärke bei FETs mit Fe-dotierten Puffern bei bis zu $1.5\text{x}10^{6}$ V/cm in lateraler Konfiguration und $1.9\text{x}10^{6}$ V/cm für vertikale Messungen. Durch die C- und Fe-Dotierung des GaN-Puffers lassen sich die Gate-Leckströme und die off-state-Leckströme in FET-Bauelementstrukturen wesentlich reduzieren. Gleichzeitig wird jedoch eine Verschiebung der Schwellenspannung zu einer höheren Sperrspannung bei Erhöhung der Dotierungskonzentration des Puffers beobachtet.

Bei der Untersuchung von GaN/AlN/AlInN Heterostrukturen mit einer SiN Passivierungsschicht wurde beobachtet, dass sich der Leckstrom mit zunehmender Dicke der Deckschicht reduziert. Zusätzlich wird dadurch eine Verbesserung der Schottky Barrierenhöhe und des Serienwiderstands von Bauelementstrukturen erreicht. Die Leckmechanismen werden durch Modelle, die defektunterstütztes Tunneln und Frenkel-Poole-Emission beinhalten, erklärt.

Abstract

Because of promising material properties, including large direct bandgap, high breakdown field strength, and heterostructures resulting in two-dimensional electron gas formation, the gallium nitride-based semiconductor family is ideally suited for power electronics applications. However, reliability issues due to presence of dislocations and other native defects still limit the performance of GaN-based devices causing gate leakage and early breakdown, for instance. In this work basic material properties of MOVPE grown GaN buffer and FET structures, which form the basis for understanding and elaborating device performance, are explored.

By surface potential investigations of semi-insulating GaN layers it is demonstrated that the acceptor states introduced by carbon cause Fermi-level pinning below the midgap position at C doping levels above $1.6x10^{18}$ cm^{-3}, whereas the acceptor-states by iron impurities were always energetically located above the midgap position. The negative surface potential contrast of dislocations, as observed in carbon doped GaN samples, was found to be increasing with carbon concentration, however the dislocations in Fe-doped GaN samples exhibit neutral or only weakly negative charge contrast independent of doping content.

In the study of GaN:C and GaN:Fe films, which are used as highly resistive buffers in GaN/AlGaN and GaN/AlN/AlInN FET devices, carbon doping is found to be more effective in achieving low buffer and vertical leakage currents, as well as improving the breakdown voltages and field strengths in comparison with iron. Vertical transport measurements reveal that precursor based C-doped GaN layers with a dopant concentration of $4.6x10^{18}$ cm^{-3} exhibit an up to 5 orders of magnitude lower dark current at room temperature and significantly higher thermal activation energy than Fe-doped samples with a comparable dopant concentration. AlInN and AlGaN FETs with a C-doped buffer offer higher breakdown voltages than for a Fe-doped buffers with electric field strength around $2.6x10^{6}$ V/cm for lateral buffer leakage and above $2.4x10^{6}$ V/cm for vertical contact arrangement. In contrast, the FETs with a Fe-doped buffer enhance the breakdown field strength up to $1.5x10^{6}$ V/cm in lateral configuration and $1.9x10^{6}$ V/cm for vertical leakage measurements through the device. Both FET device structures with C- and Fe-doped GaN buffers substantially reduce gate leakage and off-state leakage currents. However, a shift in the threshold voltage to a higher reverse bias is seen for an overall increase in buffer doping level.

In the study of GaN/AlN/AlInN heterostructures with SiN passivation layer, reverse leakage currents were alleviated substantially as a function of cap layer thickness. Also an improvement in the Schottky barrier height and the series resistance of device structures was achieved. The leakage mechanisms were explained by trap assisted tunnelling and Frenkel-Poole emission models.

Acknowledgments

My experience of working for a PhD degree at Otto-von Guericke University Magdeburg has been tremendously worthwhile. It was an amazing opportunity for me to stay in Germany and work with great scientists and professors. I feel pleasure to thank many people for their contribution to the work presented in this dissertation.

First and foremost, I am honoured to express my deep gratitude and sincere thanks to my advisor, Prof. Dr. André Strittmatter for his endless support, motivation, and guidance throughout my PhD term. It is obvious that without his supervision this work would never have reached completion. His research ethics, invaluable experience, and scientific approach have given a new life to my prospective career which would always help me professionally in the future.

Since I decided to continue my studies, it was Prof. Dr. Armin Dadgar who agreed to accept me as a PhD student in this research group. I am indebted to him for giving me opportunity to carry out research work here. His enormous corroboration, academic thinking, enthusiasm, and motivational conversations gave me ambition to start the research in challenging area of nitride semiconductors which was very new field to me.

Big thanks to Dr. Hartmut Witte for being such an amiable mentor. I am grateful to him for his continuous direction on operation of various experimental techniques to perform different measurements. His involvement, encouragement, and suggestions have always been stayed with me as an asset. I hereby would like to acknowledge and extend my heartfelt gratitude to Dr. Jürgen Bläsing and Dr. Peter Veit for providing their vital technical knowledge, provision, and vast expertise on XRD and TEM analysis with me for this work.

Huge thanks to my group mates Andreas Lesnik, Silvio Neugebauer, Matthias Wieneke, Christoph Berger, Jonas Hennig, Marc P. Hoffmann, Florian Hörich, and Seshagiri R. Challa who played an important role during the course of my PhD. I am obliged to them for continuously providing samples for characterizations and technical assistance during my work. I also would like to mention their immense cooperation, obliging suggestions, and scientific discussions during span of study. Without my colleagues, I could not be able to finish it up with beautiful memories.

I also want to acknowledge Mr. Mark Smith, who is a specialist on atomic force microscopy. He guided me how to operate AFM Nanoscope for SSPM measurements when I was unable to understand.

I would also like to gratefully appreciate Prof. Dr. Umar Saeed Qureshi, who is my former advisor in Pakistan. His motivation towards research and creativity always enriched my knowledge level and help me to work in a right direction.

Very special thanks to my friend Mr. Syed Ejaz Haider for his invaluable amity and good cheer over the past four years during my stay in Magdeburg.

Most importantly, I owe enormous debt to my parents for their unconditional love and boundless support throughout my life. I am immensely grateful to my siblings for their bountiful wishes, prayers, and their selfless affection and dedication for me over the years.

I would feel delight to acknowledge funding organizations, Federal Ministry of Education and Research (BMBF) in the framework of research collaboration ZuGaNG, and Higher Education Commission (HEC) of Pakistan, who gave me opportunity to develop my skills and knowledge in this area of study.

Finally I would like to remember Prof. Dr. Alois Krost who was the head of our research group when I joined this institute in April 2013. Unfortunately, I could not work with him long but at this moment I want to offer special regards to the person, who always stand as a role model for students and scientists over the course of his career by inspiring school of thought and contribution to science.

Acronyms

2DEG	Two Dimensional Electron Gas
AFM	Atomic Force Microscopy
AlGaN	Aluminium Gallium Nitride
AlInN	Aluminium Indium Nitride
BB(L)	Blue Band (Luminescence)
CBM	Conduction Band Minimum
CPD	Contact Potential Difference
C-V	Capacitance-Voltage
EFM	Electric Force Microscopy
EPD	Etch Pit Density
FET	Field Effect Transistor
FNT	Fowler Nordheim Tunneling
FP	Frenkel Poole
FWHM	Full Width at Half Maximum
GaN	Gallium Nitride
HEMT	High Electron Mobility Transistor
HFET	Heterojunction Field Effect Transistor
ICP-RIE	Inductively Coupled Plasma Reactive Ion Etching
I-V	Current-Voltage
LED	Light Emitting Diode
LF-HF	Low Frequency-High Frequency
MIS	Metal Insulator Semiconductor
MISFET	Metal Insulator Semiconductor Field Effect Transistor
MOS	Metal Oxide Semiconductor
MOSFET	Metal Oxide Semiconductor Field Effect Transistor
MOVPE	Metal Organic Vapour Phase Epitaxy
MS	Metal Semiconductor
PL	Photoluminescence
RMS	Root Mean Square
SCR	Space Charge Region
SIMS	Secondary Ion Mass Spectrometry
SSPM	Scanning Surface Potential Microscopy
RT	Room Temperature
TAT	Trap Assisted Tunneling
TDs	Threading Dislocations
TE	Thermionic Emission
TEM	Transmission Electron Microscopy
TLM	Transfer Length Measurement
TSC	Thermally Stimulated Current

Symbols

C_p	Parallel capacitance
D_{trap}	Trap density
E_a	Activation energy
E_F	Fermi energy
G_p	Parallel conductance
I_o	Reverse saturation current
k	Boltzmann constant
n	Ideality factor
$N_{A,}$ N_D	Acceptor, Donor concentration
n_s	Sheet carrier concentration
R_c, R_s	Contact, Series resistance
R_{sh}	Sheet resistance
$V_{contact}$	Contact potential
V_r	Reverse bias
V_{th}	Threshold voltage
W	depletion width
$\Delta\phi$	Band bending
ρ_s, ρ_e	Screw and Edge components of dislocations
χ_{GaN}	Electron affinity of GaN
ϕ_b	Barrier height
ϕ_m	Metal work function
ϕ_t	Trap activation energy
μ_H	Hall mobility
τ_{trap}	Trap emission time
ω	Angular frequency
ω_R	Resonance frequency

Table of Contents

List of Figures

List of Tables

Chapter 1

Introduction

1.1 Background and motivation

GaN-based heterojunction field effect transistors (HFETs) and metal insulator semiconductor field effect transistors (MISFETs) have become increasingly important for high power and high frequency applications.[1, 2, 3] The wide band gap of GaN facilitates promising material properties like large breakdown field strength, high current density, elevated operating temperature and high cut-off frequencies, which enable high-power and high-frequency operations. [4, 5, 6] GaN based devices offer an electric breakdown field strength (E_{br}) around 10 times higher than that of Si and GaAs,[7, 8] which allows the material to withstand high power levels. Because of a 2.7 times larger electron saturation velocity (v_{sat}) compared to Si and GaAs, GaN-based devices provide high frequency and current handling capability.[7] Table 1.1 compares different material properties of GaN with other semiconductors.

Table 1.1: Physical properties of GaN and conventional semiconductors related to power performance at high frequencies (at 300 K). [7]

	Si	**4H-SiC**	**GaAs**	**GaN**	**Diamond**
Band gap energy E_g (eV)	1.1	3.26	1.42	3.39	5.45
Relative permittivity ε_r	11.8	10	13.1	9	5.5
Electric breakdown field E_{br} (MV/cm)	0.3	3	0.4	3.3	5.6
Saturation velocity v_{sat} (10^7 cm/s)	1	2	1	2.5	2.7
Electron mobility μ_n (cm^2/Vs)	1350	700	8500	1200	1900
Thermal conductivity Θ_k (W/cmK)	1.5	4.5	0.43	1.3	20

Despite the attractive properties of nitride-based devices, there are, however, still some drawbacks that limit the growth of high-quality GaN epitaxial layers causing an efficiency drop in nitride-based devices. Due to the absence of homo-substrates GaN is usually grown on hetero-substrates like Si, sapphire, and SiC with lattice mismatches of 16.9 %, 14 % and 3.4 % respectively. [9, 10] The large lattice mismatch between GaN and the foreign substrate materials leads to a low quality of epitaxial films with high threading dislocation (TD) densities in the mid-10^8 cm^{-2} range to the order of 10^{10} cm^{-2},[11, 12, 13] which not only reduce the efficiency and performance but also have a negative influence on the lifetime of devices. [14, 15] The large thermal mismatch induces strain in the epitaxial films which may yield defects and crack formation in III-N heterostructures.[16] In addition, resistive electrical contacts are also issues for fabrication of nitride-based devices. Contact properties on nitride surfaces are generally influenced by dopant incorporation and activation but also by surface states.

The power performance of GaN/AlGaN and GaN/AlN/AlInN field effect transistors (FETs) requires large breakdown voltage and high electron velocity.[7] However, these devices suffer from the presence of impurities and defects that deteriorates electrical properties and in particular limits the operation voltage. Undoped GaN, which is widely used as buffer material below the channel region in FET structures, exhibits n-type doping levels of up to 10^{17} cm^{-3} and is the major source of high background conductivity. It is proposed that this n-type conductivity is due to impurities such as oxygen and silicon,[17] and to native defects. Therefore, to obtain better device characteristics and enable high voltage operation, highly resistive buffer structures[18] are prerequisite for power electronic devices.

In order to alleviate the background conductivity and to improve the breakdown voltage, GaN heterostructures can be doped with iron (Fe) or carbon (C) atoms. Iron doping allows for the growth of semi-insulating GaN on sapphire with high crystalline quality but also shows memory effects in metalorganic vapor phase epitaxy (MOVPE).[19] An alternative approach to attain highly resistive GaN buffer layers during MOVPE is the compensation of the background conductivity by the incorporation of carbon atoms. An increase in the layer's carbon concentration can be achieved by decreasing growth temperature, pressure, or the supply of ammonia (NH_3) during GaN layer growth by MOVPE,[20] which may all decline the crystalline quality of epilayers. Hence, semi-insulating GaN layers are favorably grown by introducing pyrolytically decomposing carbon-containing precursors in the reactor (intentional doping) that allow for GaN growth under optimum conditions.[21]

The compensating deep acceptor states introduced by iron or carbon impurities are located in the upper and lower half of the GaN band gap, respectively.[22, 23] However the incorporation of intentionally introduced impurities and the formation of native defects substantially influence the surface, electrical, and optical properties of wide band gap materials. The existence of acceptor-like defects and impurities in the vicinity of the two-dimensional electron gas (2DEG) channel has been attributed to current collapse,[24, 25] dispersion and kink effects[26] under high field and/or during high-frequency operation. The high electric field increases the electron trapping phenomena during switching operation which degrades the direct current (DC) and radio frequency performance (RF) of FET devices.[27]

In addition to the reliability issues originating from charge trapping and reemission from deep levels in the GaN buffer layer, GaN/AlGaN and GaN/AlN/AlInN heterostructures also suffer from trapping effects caused by surface charges.[28, 29] Surface states have been identified as the main reason of current collapse and gate-lag behaviour in III-nitride FETs. The deposition of dielectric passivation layers such as silicon nitride (SiN_x), AlN, Al_2O_3 or HfAlO minimize the surface induced trapping effects.[30, 31] Surface passivation restrains the creation of a virtual gate along the gate-drain region and improves the output drain current by reducing the on-state resistance (R_{ON}) during operation.[28, 29]

For these reasons, a comprehensive understanding of surface effects would be beneficial to optimize device performance. In previous studies, different groups have reported investigations by surface potential measurements of undoped,[32, 33] n-type, and p-type GaN layers,[34, 35, 36] but the discussion is still incomplete, especially as an investigation of highly resistive GaN layers is missing. Moreover, a direct comparison of the two common deep acceptor dopants carbon and iron for semi-insulating GaN layers does presently not exist. Therefore to explain the properties of GaN-based devices upon such doping to obtain semi-insulating properties, the surface and local electronic behaviour of GaN buffer structures in correlation with FET device structures need to be addressed. With regards to charge trapping processes caused by surface and interface states, an analysis of GaN-based FET structures upon surface nitridation may yield additional information.

1.2 Objective of this work

This work focuses on a study of the material properties of GaN-based device structures, to gain a better understanding of the role of impurities which will help to improve electrical performances of GaN/AlN/AlInN FETs, for high power and high-frequency operations. A substantial goal is to achieve large breakdown field strengths and to mitigate buffer (lateral) current leakage and vertical charge transport. For that purpose, Fe- or C-doped GaN buffer layers inserted between the AlInN barrier layer and the substrate are investigated. A major part of this work is therefore devoted to a comparative study of Fe- and C-doped GaN layers and of the influence of these dopants on the electrical properties of FET devices. The compensation effects and current transport properties of C- and Fe-doped GaN are investigated by employing electrical and optical measurement techniques. For reference undoped and conductive GaN layers (n- and p-type) are also studied where doping in conductive GaN layers is attained by Si-, Ge- or Mg- dopants. These investigations show the effect of dopants and doping levels on the surface, electrical, and optical properties of GaN.

To mitigate the surface leakage currents in GaN/AlN/AlInN heterostructures, SiN passivation layers with different thicknesses are deposited on top of AlInN barrier layers and their impact on current leakage mechanisms is explored. Another study has been performed on charge capture and emission processes from traps located in the barrier or GaN buffer layers and results are correlated to electrical device properties.

This thesis is organized as follows.

Chapter 2 presents relevant material properties such as crystal structure, doping and compensation effects, and the current understanding of GaN surface properties. This chapter also discusses polarization effects within nitride heterostructures which are responsible for the formation of a 2DEG in high electron mobility structures. An overview of defects in nitrides and their influences on device performance is included as well.

Chapter 3 describes the principles of the characterization techniques used in this work.

Chapter 4 deals with a detailed characterization of carbon and iron-doped GaN buffer structures with a focus on the surface potential distribution upon semi-insulating doping. The compensation effects of C and Fe are compared by scanning probe microscopy and photoluminescence techniques, whereas the leakage currents, transport properties, and breakdown voltages are studied by electrical techniques. For reference, undoped, n-, and p-type GaN layers are also characterized and compared to the resistive GaN samples.

The effect of a carbon or iron doped GaN buffer on electrical properties of GaN/AlN/AlInN and GaN/AlGaN FETs is presented in chapter 5. Hall-effect, current-voltage and capacitance-voltage techniques are applied to determine electrical device characteristics.

In chapter 6 the electrical characterization tools are adopted to discuss the effect of a SiN surface passivation layer on device properties of GaN/AlN/AlInN heterostructures. Analysis of gate leakage mechanisms is also reported providing insights into their possible origins.

Chapter 2

Properties of III-nitride materials

2.1 Introduction

Group III-nitride semiconductors with the binary compounds GaN, InN, and AlN and their alloys are of particular interest for radio frequency and power switching applications. The band gap of III-nitrides covers a wide range at room temperature from 0.7 eV for InN over 3.4 eV for GaN to 6.2 eV for AlN, which makes them potential candidates for the fabrication of power electronic and optoelectronic devices.[37, 38] This chapter is focused on the material properties of nitride semiconductors that give them an advantage in designing high electron mobility transistor (HEMT) applications. The key features like crystal structure, polarization effects, compensation mechanism, surface potential, and defects in III-nitrides will be discussed in detail in the next sections.

2.2 Crystal structure properties

Group III-nitride semiconductors mainly exist in wurtzite (Wz) and zinc-blende (ZB) crystallographic structures. However, the wurtzite is a thermodynamically more stable structure for bulk AlN, GaN, and InN under ambient conditions and GaN-based HFETs are primarily grown with Wz crystal structure.[38] The wurtzite crystal structure exhibits hexagonal symmetry and the unit cell holds six atoms of each type. It belongs to the space group $P6_3mc$ in the Hermann-Mauguin notation and C_{6v}^4 in the Schönflies notation. An ideal Wz crystal lattice consists of two hexagonal close-packed (hcp) sublattices, each composed of group-III elements and nitrogen atoms respectively, and offset along c-axis by 5/8 of the cell height.[39]

Figure 2.1 shows the GaN in wurtzite crystallographic structure represented by lattice parameter **a** in the basal plane, parameter **c** along the z-axis, and the internal parameter **u**, where blue and grey spheres indicate Ga and nitrogen atoms, respectively. The parameter **a** is the length of the basal hexagon along the $[11\bar{2}0]$ axis, while the lattice constant **c** denotes the axial lattice parameter perpendicular to the basal plane which depicts the height of a unit cell along the [0001] axis. In the basic unit, an interatomic distance is described by the parameter **u**, which is define as a ratio between anion and cation bond length and lattice parameter **c**.[38]

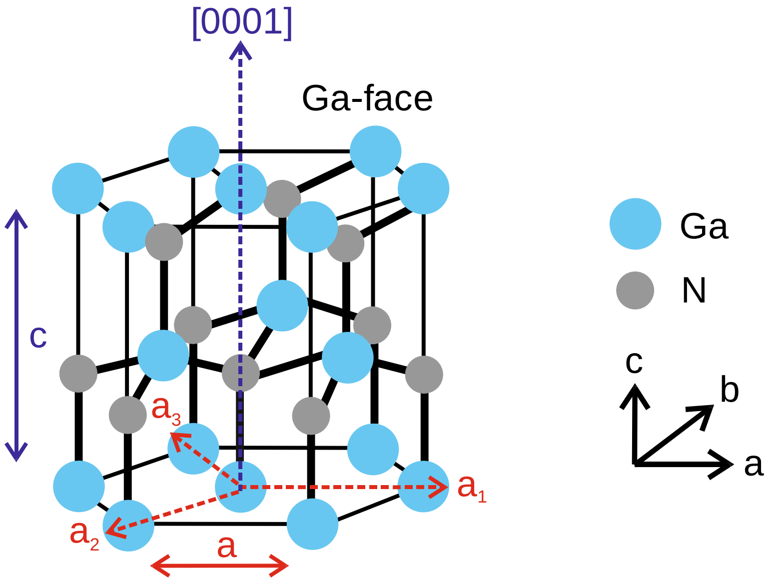

Figure 2.1: Wurtzite Ga-face terminated crystal structure of GaN

To specify the crystal planes and directions of the hexagonal wurtzite III-nitrides, the notation for the four-index Miller indices (hkil) is assigned where i = $\overline{h+k}$ (the overline is used to specify a negative quantity). The lattice parameters (**c** and **a**) exhibit temperature dependence which can be expressed by thermal expansion coefficients, $\Delta a/a=\alpha_a$ for in-plane and $\Delta c/c=\alpha_c$ for out-of-plane configuration using the Debye model.[40] Table 2.1 presents the values of the structural parameters, axial ratio c/a, and the mean values of thermal expansion coefficients of III-nitrides in the c- and a-plane.

Table 2.1: Basic properties of bulk InN, GaN and AlN [38, 40]

	InN	**GaN**	**AlN**
c (Å)	5.703	5.185	4.982
a (Å)	3.545	3.189	3.112
c/a ratio	1.609	1.626	1.601
u	0.377	0.376	0.380
E_g (eV)	0.78	3.42	6.2
$\Delta a/a$ (K^{-1})	$4\text{x}10^{-6}$	$3.43\ \text{x}10^{-6}$	$4.35\ \text{x}10^{-6}$
$\Delta c/c$ (K^{-1})	$3\ \text{x}10^{-6}$	$3.34\ \text{x}10^{-6}$	$3.48\ \text{x}10^{-6}$

All group III-nitride materials favor partially iconicity and partially covalent nature.[38] Figure 2.1 depicts that in the Wz structure, there are pairs of cation and anion atoms connected by thick solid lines along the [0001] direction and attracted to each other by electrostatic force.[40] It is considered that these electrostatic interactions make the Wz crystal structure more stable than the ZB crystal structure. The inherent anisotropy of crystalline structure results in polar characteristic of the atomic configurations. Material grown along the [0001] direction have group III-element (Al, Ga, or In) polarity also referred as Ga-polar whereas the material is grown in the opposite direction $[000\bar{1}]$ are called N-polar. Ga-polar structure is just a mirror image of the N-polar structure. The polarity of GaN is usually acquired by the substrates, nucleation layer and also the growth method. Surface properties of GaN are deeply influenced depending on whether the structure is Ga or N polar. Commonly the Ga-polar surface is preferred for GaN based structures because it favours the two-dimensional growth while the N-polar GaN typically exhibits rough surface morphology. To identify the polarity of the films different methods like wet chemical etching and convergent beam electron diffraction etc can be used.[38, 41]

2.3 Imperfection of crystal structure

The crystal structure of group III-nitride materials may contains some linear imperfections or dislocations around which atoms are misaligned from their regular arrangement within a crystal. These imperfections are originated in the epitaxial material due to a large lattice mismatch between the III-nitride layers itself or the substrate. One major issue that is still associated with the growth of GaN-based heterostructures is that they contain a high density of dislocations.[9-11] They often behave as electrically active crystalline defects in nitride materials which play an influential role on the electrical properties of devices.[42, 43] In GaN-based power electronic applications, dislocations act as current leakage paths and scattering centers inside the channel, hence control the device properties by lowering carrier mobility. In optical devices dislocations degrade the efficiency of light emitting diodes (LEDs) and lasers through non-radiative recombination paths. Despite the presence of high dislocation densities, GaN-based LEDs, in contrast to conventional III-V LEDs, exhibit a higher radiative recombination rate enabling better device efficiencies.

The dislocations are typical line defects where a discontinuity within the crystal structure forms broken bonds known as dangling bonds while the edge of the broken plane can be viewed as a line with dangling bonds. They are classified into two basic types; edge and screw type dislocations and one which is a combination of both types called mixed dislocation. Figs. 2.2 (a) and (b) respectively show the atomic arrangement surrounded by edge and screw dislocations which is distorted from the regular periodicity of the lattice. Dislocations are expressed by two properties a line direction "*l*", which is the direction of the dislocation and the Burgers vector **b** which describes the magnitude and direction of the lattice distortion. For edge-type dislocation $\mathbf{b}=1/3\langle 11\bar{2}0\rangle$ is orthogonal to *l* whereas for screw-type dislocation $\mathbf{b}=\langle 0001\rangle$ is parallel to *l*. Mixed dislocations with $\mathbf{b}=1/3\langle 11\bar{2}3\rangle$ are characterized by $0° < \alpha(b, l) < 90°$. [33, 44]

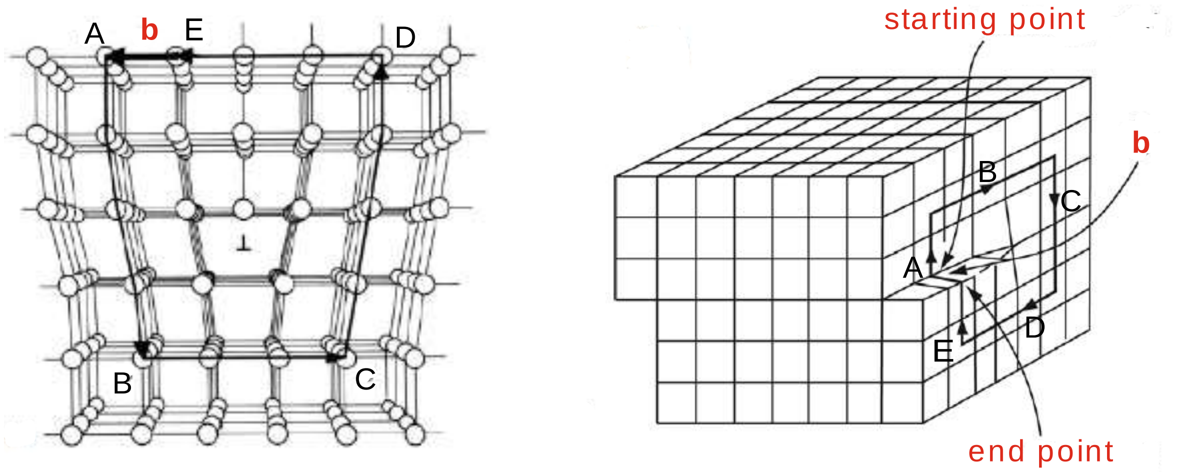

(a) (b)

Figure 2.2: (a) Edge and **(b)** Screw dislocations: Arrangement of atoms and Burgers vector **b** that produces closure of circuit ABCDE.[44]

The geometry of an edge type dislocation is relatively easy to visualize that can be imagined as an extra half-plane of atoms terminating at the dislocation line perpendicular to the plane and passing through the symbol ⊥ as shown in fig. 2.2 (a).[44] Burgers vector **b** shows the deformation of the periodic atomic arrangement by a circuit ABCDE created around the dislocation line. Here (in fig. 2.2 (a)), the movement of an edge dislocation in its slip plane is along the direction of the **b** (slip direction). Fig. 2.2 (b) depicts the Burgers circuit ABCDE containing a screw component of dislocation, where the dislocation moves in the slip plane perpendicular to the Burgers vector (slip direction). It is found that the dislocations with an edge component, introduce acceptor centers along the dislocation line which trap electrons, thus the dislocation lines become negatively charged creating a space charge around it. The charge transport process across the dislocations is affected by scattering at dislocation regions causing a decrease in electron mobility. [45]

2.4 Doping and compensation

This section deals with the influence of doping on the conductivity of a semiconductor and the mechanism behind compensation doping. In an intrinsic semiconductor, intentionally introduced impurities influence the electrical behaviour of the material. The negative or positive free charge carriers introduced by doping lead to excess electrons or holes in the conduction or valence band, respectively.

Figure 2.3 shows the energetic positions for shallow donor and acceptor states (before and after ionization) within the band gap, while E_i represents the intrinsic Fermi level position when $n = p = n_i$. Here n is the electron concentration in the conduction band, p is the hole concentration in the valence band, while n_i is the intrinsic carrier concentration. In the case of n-type material, a small amount of energy (E_C-E_D) is required to excite electrons from the donor level (E_D) to the conduction band. Typically, at room temperature the thermal energy (25 - 34 meV) is sufficient to ionize all shallow donors as, e.g. Si or Ge in GaN.[38, 46] If donors and acceptors are present in a material in similar concentration, they partly compensate each other. In order to calculate the carrier concentration for a non-degenerate semiconductor, the charge neutrality relation is used that is described as:

$$\mathrm{n} + \mathrm{N}_\mathrm{A}^{-1} = \mathrm{p} + \mathrm{N}_\mathrm{D}^{+1} \tag{2.1}$$

where $\mathrm{N}_\mathrm{D}^{+1}$ and $\mathrm{N}_\mathrm{A}^{-1}$ are ionized donor and acceptor concentrations.

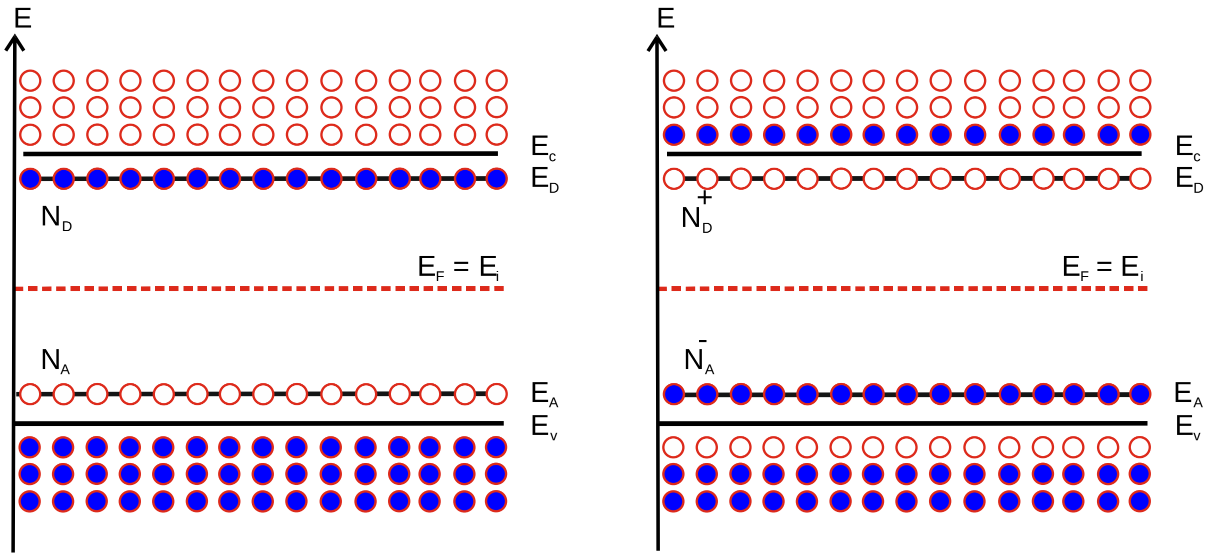

(a) before ionization

(b) after ionization

Figure 2.3: Band diagram illustrating donor and acceptor distribution within the band gap

The charge carrier densities with respect to its Fermi level under local charge neutrality conditions can be expressed as after re-writing Eq. 2.1 as: [47]

$$\mathrm{N_c}\exp\left(\frac{\mathrm{E_c}-\mathrm{E_F}}{\mathrm{kT}}\right)+\sum_{\mathrm{i}}\frac{\mathrm{N_{Ai}}}{1+\mathrm{g_{Ai}}\exp\left(\frac{\mathrm{E_F}-\mathrm{E_{Ai}}}{\mathrm{kT}}\right)}$$
$$=\mathrm{N_v}\exp\left(\frac{\mathrm{E_F}-\mathrm{E_v}}{\mathrm{kT}}\right)+\sum_{\mathrm{i}}\frac{\mathrm{N_{Dj}}}{1+\mathrm{g_{Dj}}\exp\left(\frac{\mathrm{E_{Dj}}-\mathrm{E_F}}{\mathrm{kT}}\right)} \tag{2.2}$$

Here the left side is the net contribution of negatively charged electron and ionized acceptor densities, and the right side is the sum of the positively charged hole and ionized donor densities. N_c and N_v are the effective densities of states in the conduction and valence band respectively, N_D and N_A are the donor and acceptor concentrations (summed over i or j), E_c, E_v, and E_F are the conduction band minimum (CBM), the valence band maximum (VBM), and the Fermi level, g_{Ai} and g_{Di} are degeneracy factors for respective acceptor and donors.[47] Under the assumption $E_D–E_F >> kT$ or $E_F–E_A >> kT$, all donor/acceptor states are completely ionized that is all donor impurity atoms N_D are empty after donating free electrons to the conduction band and vice versa [Fig. 2.3 (b)]. For a material to exhibit n-type conductivity under complete ionization, $n \approx N_D >> N_A$ while the free electron concentration in the conduction band can be calculated accordingly:

$$\mathrm{n}{\approx}\mathrm{N_D}=\mathrm{N_D^{+1}}=\mathrm{N_c}\exp\left(\frac{\mathrm{E_c}-\mathrm{E_F}}{\mathrm{kT}}\right) \tag{2.3}$$

Hence for n-type:

$$\mathrm{E_F}=\mathrm{E_c}-\mathrm{kT}\ln\left(\frac{\mathrm{N_c}}{\mathrm{N_D}}\right) \tag{2.4}$$

Here donors are located at an energy E_D within the energy gap while the Fermi level position is energetically below E_D and most of the donor states are empty i.e. ionized. Similarly, in case of p-type conductive materials, majority carriers are holes and $N_A >> N_D$ while n=0. Therefore for a non-degenerate material at thermodynamic equilibrium, the position of the Fermi level with respect to valence band can be described as:

$$\mathrm{E_F}=\mathrm{E_v}+\mathrm{kT}\ln\left(\frac{\mathrm{N_v}}{\mathrm{N_A}}\right) \tag{2.5}$$

For p-type doping of GaN, Mg_{Ga} acceptor impurity usually provides 0/−1 transition level around (0.2 - 0.3) eV above the valence band maximum. However the Mg_{Ga}-V_N complex, the nitrogen vacancy (V_N), and magnesium interstitial (Mg_{inter}) behave like counteracting donors in heavily Mg-doped materials causing self-compensation. Hence the charge compensation equation is described as: [48, 49]

$$[\mathrm{Mg}_{\mathrm{Ga}}^{-}] = 2[\mathrm{Mg}_{\mathrm{inter}}] + \mathrm{V}_{\mathrm{N}} + \mathrm{p} \qquad (2.6)$$

Fig. 2.4 (a) illustrates the energetic position of different impurities along with carbon and iron related compensating acceptor levels. Undoped GaN without intentional compensation of impurities is intrinsically n-type due to a native electron concentration $n \geq 5\mathrm{x}10^{16}$ cm^{-3} stemming from impurities as O or Si and nitrogen vacancies.[50] In undoped GaN the intrinsic carrier concentration is rather low due to large band gap energy, therefore to construct a p-n junction it is required to incorporate dopants inducing shallow donor or acceptor energy level. On the other side, high power/frequency applications require semi-insulating GaN layers to provide high breakdown voltages, hence high resistivity may be achieved by compensation of residual donors with $\mathrm{C}_{\mathrm{N}}^{-1}$ or $\mathrm{Fe}^{+3/+2}$ acceptors. When C or Fe atoms are added in undoped GaN, the free electron concentration will decrease relative to the acceptor concentration, therefore the position of the Fermi level shifts from the CBM towards midgap.

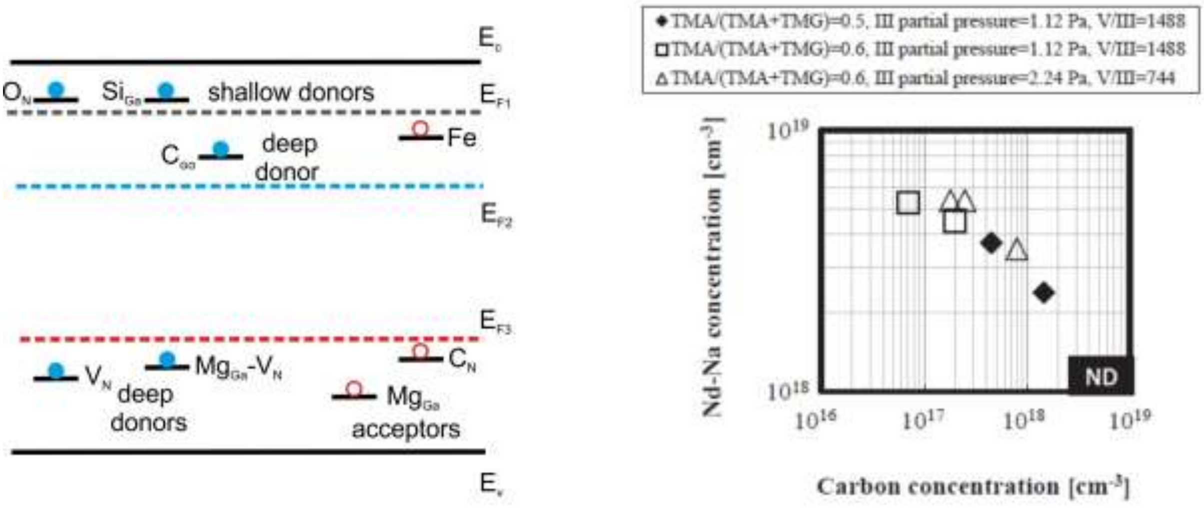

(a) (b)

Figure 2.4: (a) The compensation model exhibiting various donors and acceptors level; **(b)** Correlation between carrier concentration and carbon concentration.[51]

According to fig. 2.4 (a) the shallow and deep donor states are located at various energetic positions within the band gap in undoped GaN; therefore the Fermi-level position is determined by the relative concentrations and activation energies of both donors and acceptors. In undoped GaN the Fermi level is assumed to be located below conduction band minimum at energetic position of shallow donors, however as the electron concentration decreases, the E_F moves farther below E_c. For low C or Fe concentrations only the shallow donors near the valence band are compensated and the Fermi-level will be pinned to the position E_{F1}. With further increase in acceptor concentration the next deep donors also take part in the compensation mechanism shifting the Fermi level position towards midgap (for Femi level position E_{F2}).[52] It is in agreement with Eq. 2.4 which proposes that the Fermi level must move away from the CBM when reducing the electron concentration. Therefore the compensation model follows the step like behaviour for different acceptor concentrations as illustrated in fig. 2.4 (a), and the Fermi level position after compensation is determined by considering not only the total acceptor concentration N_A but also the energetic distribution of the donors.[52]

Figure 2.4 (b) presents the decrease in net carrier concentration (N_D-N_A) with increasing carbon concentration for different growth parameters.[51] The compensation model defines the compensation ratio $r = N_D/N_A$ as $r = 1$ if all carbon atoms are activated as acceptors (C_N) below midgap region, while for $r = -1$ all C atoms must act as donors (C_{Ga}) above midgap.[53] Moreover the auto-compensation process of substitutional C_N and C_{Ga} also affects the compensation ratio. To achieve high resistivity material or to decrease the free electron carrier concentration the compensation ratio should be close to 1. An incorporation efficiency of carbon as an acceptor can be expressed as $K=[C]^-/[C]$, where [C] is the total carbon concentration and $[C]^-$ are the ionized C-acceptors.[50]

2.5 Surface properties of GaN

The knowledge of localized surface properties of the GaN system is of fundamental interest for understanding the physics and performance of devices. This section explains the surface potential distribution and the metal contact formation on semiconductor surface.

2.5.1 Surface potential in III-nitrides

The surface potential of semiconductors depends on the doping species and doping concentration, hence dopants in epitaxial layers as well as surface states affect the surface behaviour.[54] In general, negatively charged surface states introduce an upward band bending in n-type GaN whereas positive charged surface states cause downward band bending in p-type GaN due to Fermi level pinning at the GaN surface.

It has been demonstrated that the surface Fermi level position substantially affect the formation and concentration of the 2DEG at the heterointerface, which is the foundation of HEMT structures.[55] The position of the Fermi energy relative to the conduction band minimum can be determined by measuring the surface potential, which is directly associated with the electrostatic potential and electric field strength of the material. In GaN/AlGaN high electron mobility transistors, the two-dimensional electron gas exists within a few nanometres below the surface. The accumulation of polarization-induced surface and interface charges establish an electric field which introduces band bending at the GaN/AlGaN hetero interface.[56, 57] Moreover donor states on the AlGaN surface change the sheet carrier density, consequently the surface potential distribution. In order to describe surface potential metal insulator semiconductor (MIS) structure is considered, because in potential measurement by scanning surface potential microscopy the metal probe (cantilever) and semiconductor material surface separated by a constant distance form an MIS capacitor. The surface potential V_S in the case of MIS structure can be expressed as: [58, 59]

$$eV_S = \phi_m - \chi_S - \chi_D - (E_c - E_F) - \Delta\phi \tag{2.7}$$

here ϕ_m is the metal work function of the tip coating, χ_S is the electron affinity of the surface, χ_D is the electron affinity due to a dipole effect, and $\Delta\phi$ is the band bending caused by surface states.[59, 60] Thus the surface potential study allows determining the relative change in the Fermi level position at the semiconductor surface upon doping with reference to metal probe including band banding and dipole effects. It can be quantitatively measured by recording the contact potential difference (CPD) between a reference probe and the semiconductor surface after placing a metallic probe above the surface (see also chapter 3). Usually, the surface effects originate in the crystallographic characteristics like the surface morphology, dopant impurities, interfaces and defects, polarization fields, and dangling bonds at the surface.

2.5.2 Metal-semiconductor contact formation

The theory of metal-semiconductor junctions was first presented by W. Schottky to discuss the properties of contact between metal and semiconductor surface. When a metal is brought into contact with an n-type semiconductor, the Fermi-levels of both materials exchange charges to achieve equilibrium (in this case) by transferring electrons from the metal to the conduction band of the n-type semiconductor. Matching the Fermi levels leads to a potential barrier and introduces band bending of the conduction and valence band close to the metal-semiconductor interface. Here the difference in work functions between metal and semiconductor and the electron affinity of the semiconductor play an important role. According to the Schottky-Mott theory the difference in the values of metal and semiconductor work functions creates a potential barrier ϕ_b called the Schottky barrier. Such rectifying metal-semiconductor contact is also referred as Schottky contact. Figs. 2.5 (a) and (b) respectively show schematic diagrams of a Schottky barrier for n- and p-type GaN after a contact has been formed and equilibrium is achieved.

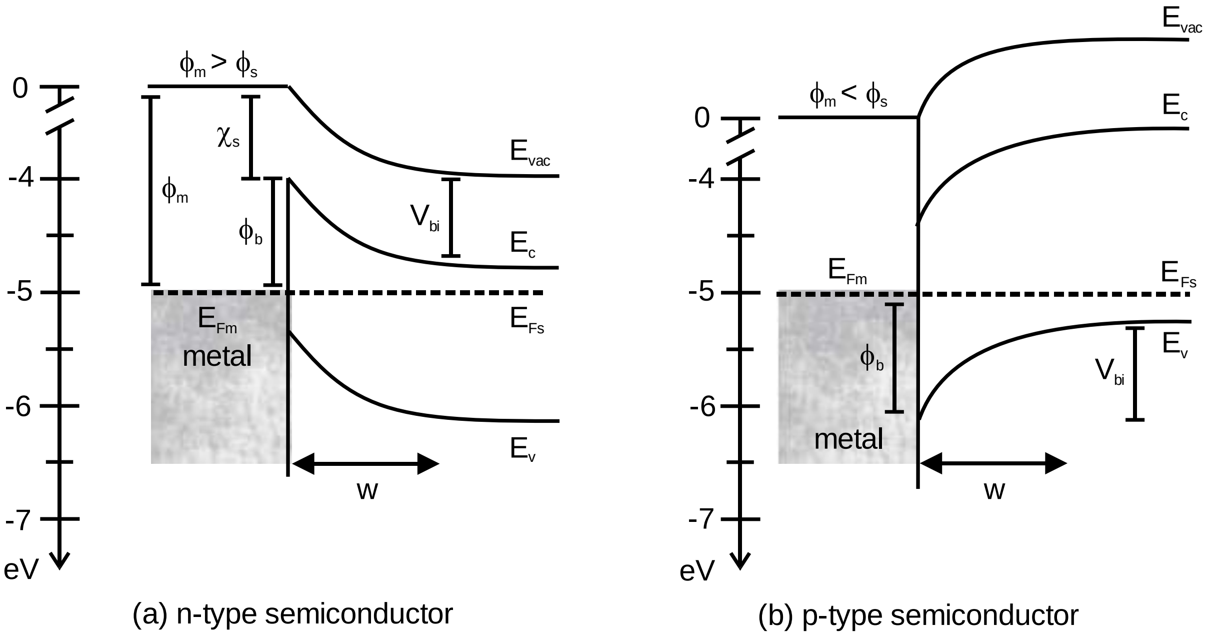

Figure 2.5: Schematic diagrams of an ideal metal-semiconductor contact for **(a)** n-type and **(b)** p-type GaN.

According to the Schottky-Mott theory: [61]

$$\phi_b = \phi_m - \chi_s = qV_{bi} + \Delta E_{fn} \tag{2.8}$$

$$\phi_s = \phi_m - qV_{bi} = \Delta E_{fn} + \chi_s \tag{2.9}$$

where $\Delta E_{fn} = E_c - E_F$ is the energy difference of the Fermi-level and the conduction band, ϕ_b is the barrier height, ϕ_s semiconductor work function, q the electronic charge, and V_{bi} the built-in potential of the junction. In this simplified approach it is assumed that surface dipole contributions to the barrier height and the electron affinity remain unchanged when the metal and the semiconductor are brought into contact. Also no physical strains or chemical reactions are created between the two materials at the interface. However, in reality surface dipole layers always influence the contact formation by altering the potential difference between metal and semiconductor.

The above model is applicable to an n-type semiconductor where $\phi_m > \phi_s$ [Fig. 2.5 (a)] because the metal-semiconductor contact exhibits a rectifying behaviour if the work function of the metal is higher than that of the semiconductor. Electrons will flow from the metal to the semiconductor until the Fermi levels are aligned on both sides. In the case of p-type materials holes are majority charge carriers hence the opposite behaviour results i.e. (if $\phi_m < \phi_s$) there exists a potential barrier for holes to cross from the metal to the semiconductor and the alignment of the Fermi levels create a downward band bending. However, if $\phi_m > \phi_s$ (for p-type semiconductors) or $\phi_m < \phi_s$ (for n-type semiconductors) the potential barrier at the metal-semiconductor interface will vanish and a non-rectifying (ohmic) electrical behaviour of the contact is obtained.

2.6 Properties of high electron mobility transistors

GaN based AlGaN and AlInN high electron mobility transistors grown by metal organic vapour phase epitaxy or molecular beam epitaxy systems are the topic of interest for high frequency and high power solid-state devices, due to their large 2DEG mobility and high breakdown voltages. Some important characteristics of high electron mobility transistors are discussed below.

2.6.1 Spontaneous and piezoelectric polarization effects

Nitride based heterostructures show strong polarization effects that are taken into account for design and device engineering.[58] There are two sources of polarization in III-Ns known as spontaneous ($\mathbf{P}_{sp}$) and piezoelectric ($\mathbf{P}_{pz}$) polarization, which are equally important to determine the electrical properties of devices as HEMTs. In the absence of external electric fields the total polarization field $\mathbf{P}_{total}$ is the sum of the spontaneous and strain-induced piezoelectric polarization: [62, 63]

$$\mathbf{P}_{\text{total}} = \mathbf{P}_{\text{sp}} + \mathbf{P}_{\text{pz}} \tag{2.10}$$

The spontaneous polarization in III-nitrides is associated to an intrinsic asymmetry of the bonding in the equilibrium crystal structure. The hexagonal geometry of the wurtzite structure of nitrides lacks an inversion symmetry, which plays important role for polarization effects to occur in a crystal.[64, 65] The spontaneous polarization of the wurtzite crystal structure of III-nitrides along c-axis can be simply expressed as $\mathbf{P}_{sp} = P_{sp}\,\hat{z}$.

The strain-induced piezoelectric polarization exists in GaN/AlGaN heterostructures, due to the distortion of crystal lattice as a result of mechanical stress.[62] Since the lattice constant of GaN is larger than AlGaN, when an AlGaN layer is grown on top of a GaN buffer, the lattice mismatch introduces tensile strain in the barrier layer. This strain results in the piezoelectric field, expressed by the piezoelectric coefficients e_{ij} and the strain tensor ε_j as $\mathbf{P}_{pz} = \Sigma e_{ij}\varepsilon_j$.[62] The strength of piezoelectric polarization can be calculated according to the following expression: [64]

$$\mathbf{P}_{\mathrm{pz}} = \mathrm{e}_{33}\varepsilon_3 + \mathrm{e}_{31}(\varepsilon_1 + \varepsilon_2) \tag{2.11}$$

where $\varepsilon_3 = (c - c_0)/c_0$ is the strain along the c-axis, and $\varepsilon_1 = \varepsilon_2 = (a - a_0)/a_0$ is the in-plane strain that is assumed to be isotropic, a_0 and c_0 are the equilibrium values of the lattice parameters.[64] Using the relation between the lattice and elastic constants of hexagonal GaN, the amount of piezoelectric polarization along the c-axis can be calculated as:

$$\mathbf{P}_{\mathrm{pz}} = 2\,\frac{\mathrm{a} - \mathrm{a}_0}{\mathrm{a}_0}\left(\mathrm{e}_{31} - \mathrm{e}_{33}\frac{\mathrm{C}_{13}}{\mathrm{C}_{33}}\right) \tag{2.12}$$

where C_{13} and C_{33} are elastic constants. Hence, the total polarization $\mathbf{P}_{total}$ is the sum of both components $\mathbf{P}_{sp}$ and $\mathbf{P}_{pz}$ and the gradient of polarization in space is associated with the polarization induced charge density ρ_{pol} given as: [63]

$$\nabla\mathbf{P}_{\mathrm{total}} = \nabla.\left(\mathbf{P}_{\mathrm{sp}} + \mathbf{P}_{\mathrm{pz}}\right) = -\rho_{\mathrm{pol}} \tag{2.13}$$

Here the negative sign is only for a convention to show that a polarization field in a solid goes from the negatively charged to the positively charged interface. Table 2.2 describes the experimentally measured values for spontaneous and piezoelectric polarization coefficients and elastic constants reported in previous studies.

2.6.2 Formation of 2DEG in HEMTs

The total polarization fields along with a large band gap offset of GaN/AlGaN high electron mobility transistor structures enables the formation of a 2DEG at the heterointerface without intentional doping of the barrier layer.[66] Due to polarization induced positive and negative charges an electric field is established within the AlGaN layer [Fig. 2.6 (a)],[58] which introduces band bending in both the AlGaN and GaN layers. Hence the conduction band edge of GaN at the interface to AlGaN shifts below E_F as depicted in figure 2.6 (b), depending on Al concentration and with it strength of the electric field. The difference in band gap energies between AlGaN and GaN leads to offsets ΔE_c and ΔE_v, at conduction and valence bands.

Table 2.2: Spontaneous polarization, piezoelectric coefficients and elastic constants. [40, 62]

	InN	**GaN**	**AlN**
P_{sp} (C/m^2)	– 0.032	– 0.029	– 0.081
e_{31} (C/m^2)	– 0.57	– 0.49	– 0.60
e_{33} (C/m^2)	0.97	0.73	1.46
C_{13} (GPa)	92	106	108
C_{33} (GPa)	224	405	373

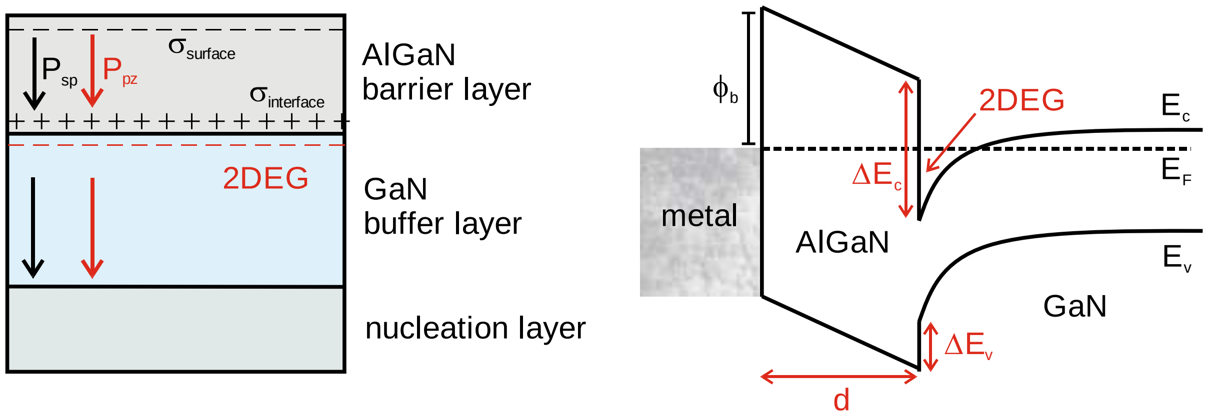

(a) (b)

Figure 2.6: (a) Polarization effects; and **(b)** Energy band diagram of GaN/AlGaN HEMT

At the heterointerface, the structure formed typically is very narrow and thus a quantum well containing the 2DEG where electrons accumulate from the donor like surface states or bulk GaN material.[67] Because of the electrons being confined in the triangular shaped quantum well they are free to move within a plane along the interface. The electron densities can be controlled by the choice of the materials and their alloy compositions. Sheet carrier concentration of a 2DEG at an $Al_xGa_{1-x}N$/GaN interface for a nominally undoped heterostructure can be approximated as: [58, 68]

$$n_s = \frac{\sigma_{pol}}{e} - \left(\frac{\epsilon_{AlGaN}}{e^2\, d}\right)(e\phi_b + E_F - \Delta E_c) \tag{2.14}$$

where $\sigma_{pol} = \sigma_{AlGaN} - \sigma_{GaN}$ is the net polarization-induced charge density at the surface, ϵ_{AlGaN} is the dielectric constant of AlGaN, e is the elementary charge, E_F is the Fermi-level position at the hetero-interface, ΔE_c is the conduction band discontinuity between AlGaN and GaN as shown in fig. 2.6 (b), and d is the thickness of the $Al_xGa_{1-x}N$ barrier layer.

2.6.3 Device characteristics

To enhance the power handling capability of an electronic device, the breakdown voltage (which causes device to enter the breakdown region) is an important parameter which depends on the electric field distribution within the structure. Fig. 2.7 (a)[69] and (b)[29] show the device structure for AlGaN, and the DC current-voltage (I-V) characteristics of an ideal HEMT where V_{DS} and I_{DS} are drain-source voltage and current, respectively.

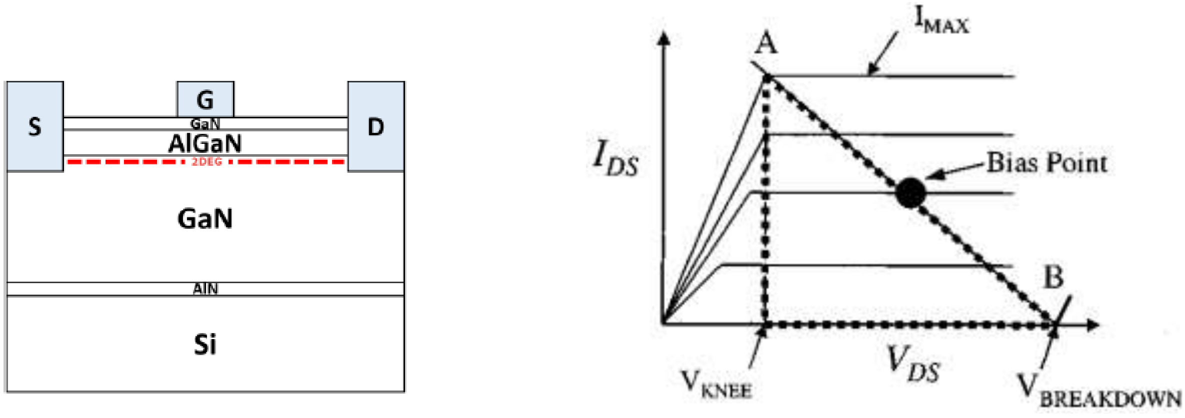

(a) (b)

Figure 2.7: (a) Device structure for AlGaN HEMT; [69] **(b)** DC current-voltage characteristics of an ideal HEMT.[29]

The maximum output power of the device during operation is given by the relation: [29]

$$P = \frac{I_{MAX}}{8} \text{ x } (V_{BR} - V_{KNEE}) \tag{2.15}$$

Here I_{MAX} is the maximum drain current of the device, while 'V_{KNEE}' is the voltage at which drain current saturates. The current leakages between gate and drain contacts reduces breakdown voltages of device. Such currents are associated to vertical and lateral tunnelling leakage paths in GaN-based heterostructures which can be suppressed by surface passivation techniques using dielectric layer on barrier.[28, 29] Besides the device breakdown happening between the gate and drain contacts, the leakage current flow in the GaN buffer region and buffer-substrate interface also results the breakdown mechanism.[70, 71] In order to avoid such breakdown, semi-insulating GaN buffer layers are essential which support the large blocking voltages required in high power electronic devices.

2.7 Defects in III-nitride semiconductors

In a real semiconductor crystal structure entropy and trace impurities will always create imperfections which are defined as defects. Nitride semiconductors grown on foreign substrates typically contain a high density of extrinsic defects. As the results obtained in this work are to be discussed with regard to defects this chapter categorize them by their dimension and localization within the band gap.[72]

2.7.1 Point defects

These are zero-dimensional defects associated with an isolated crystal site which alter the crystal periodicity at one lattice site or at most at a few atoms. These defects are classified as either intrinsic defects which appear in a pure crystal, or as extrinsic defects which are due to foreign atoms sitting on a lattice or interstitial site of the host crystal. In order to understand how point defects alter or control the local electronic and electrical properties of semiconductors, it is important to identify them as shallow or deep defects within the band gap. If the defect states are close to the conduction or valence band edges (few tens of meV from the respective band edges), then they are called shallow defects. However, if the energy position of the defects is close to mid-gap, then they are deep defects which can trap excess charge carriers, depending on their type (acceptor or donor). Impurities that create shallow levels are used for p- or n-type doping. Deep traps shift the Fermi-level towards their respective energetic position and increase the resistivity of the material. Deep acceptors in GaN close to the mid gap position with higher concentration than the free electron background concentration create semi-insulating behaviour by trapping free electron.[72]

Figure 2.8 shows shallow and deep defects located within the band gap of GaN relevant for this thesis. The role of electron and hole traps in photoluminescence (PL) spectra observed in GaN is of great importance, because the defect PL bands determine the crystalline and optical quality of GaN. The yellow luminescence (YL) band at 2.15 eV in GaN is attributed to transitions involving the $(V_{Ga}\text{-Si})^{2-}$ or $(V_{Ga}\text{-O})^{2-}$ complexes. At the same time, the optical transitions involving C_N acceptor or its complexes with oxygen are also proposed for the famous YL band in GaN.[48, 73] A broad blue luminescence (BL) band near 2.7 eV often appeared for Mg acceptors in GaN while for Mg acceptor complexes with nitrogen vacancy in GaN, the existence of a broad red PL band peaked near 1.8 eV is predicted.[48] Photoluminescence experiments on C-doped GaN also exhibit BL involving +/0 optical transition level associated with C_N defect state.[74] Iron related deep states in GaN are found to behave both as radiative and nonradiative recombination centers.[75]

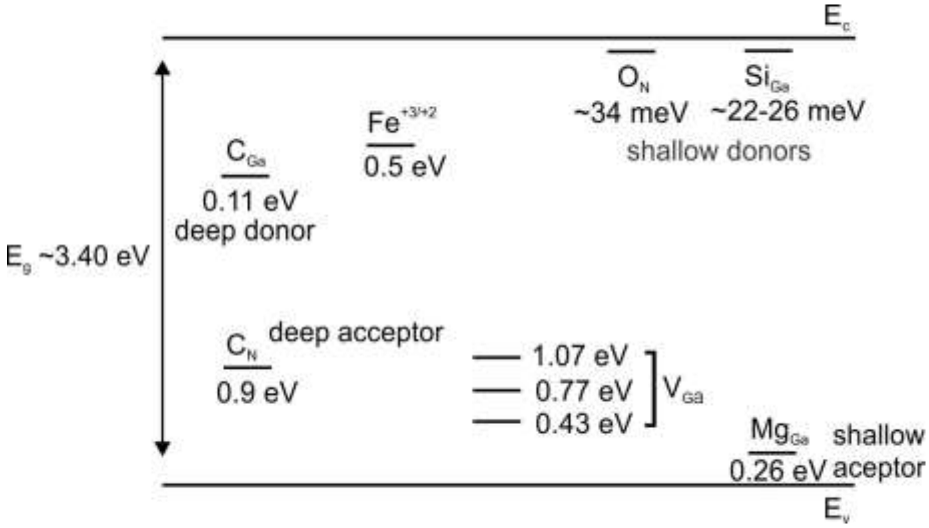

Figure 2.8: Energetic positions of shallow and deep level defects in GaN. [46, 48, 73, 76]

2.7.2 Interfaces, Grain boundaries, and Stacking faults

Two dimensional defects in crystals can be identified as free surfaces or interfaces, stacking faults and intercrystalline boundaries where crystallites are joined together. Surface or interface states are electronic states formed due to a change of the electronic band structure between two phases or layers. These defects influence the Schottky barrier formation at the metal semiconductor interface by Fermi level pinning and introduce heterojunction band offsets. Crystalline solids are, usually, composed of many small crystallites called grains and contain several distinct phases of different composition and crystal structure. The interfaces that distinguish two distinct grains are called grain boundaries. Other kind of planar defects are stacking faults, which are the aberrations in the sequence of atomic planes in the crystal.[72]

2.8 Current transport mechanisms

The transport properties of metal-semiconductor (MS), metal-oxide semiconductor (MOS) or MIS devices can be controlled by various parameters which can be described best in terms of current leakage mechanisms observed over a wide temperature range. This section shortly describes different carrier transport mechanisms in MIS and Schottky diodes according to their temperature and bias dependent behaviour.

2.8.1 Thermionic emission theory

Thermionic emission (TE) is one of the dominating transport mechanisms at high temperatures where electrons are driven across the potential barrier by thermal energy. Figure 2.9 illustrates the thermionic emission of carriers over the potential barrier from the metal into GaN region. The thermionic emission theory follows the assumption that the current flow is exclusively controlled by the barrier height and temperature. Accordingly, the forward bias current-voltage characteristics of a Schottky diode with the series resistance (R_S) can be described as follows: [77, 78]

$$I = A \cdot A^{*}\, T^{2} e^{-\frac{q\phi_b}{kT}} \left[\exp\left(\frac{q(V - IR_s)}{nkT} \right) - 1 \right] \tag{2.16}$$

where $I_0 = A \cdot\ A^{*}\, T^{2} e^{-\frac{q\phi_b}{kT}}$, is the reverse saturation current, T is the absolute temperature, q is the electron charge, n is the ideality factor, k is the Boltzmann constant, A is the junction area of the diode, A^* is the effective Richardson constant (55.86 A cm^{-2} K^{-2} for AlInN),[79] ϕ_b is the barrier height of the junction, V is the applied bias voltage, and IR_s is the voltage drop due to device series resistance. Thermionic emission theory suggests that barrier height and the ideality factor exhibit very weak temperature dependence.

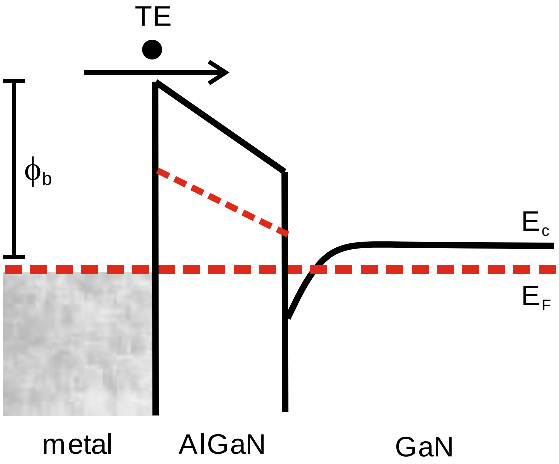

Figure 2.9: Schematic band diagram of metal/AlGaN/GaN structure for charge transport via thermionic emission mechanism.

The series resistance of device is the sum of resistances of all semiconductor layers and a voltage applied across the contacts is shared between interfacial layers and series resistance. In order to determine device parameters ϕ_b, n, and R_s a method developed by Cheung and Cheung is adopted.[80, 81] Eq. 2.16 can be re-written as:

$$V = IR_s + n\phi_b + n\left(\frac{kT}{q}\right)\ln\left(\frac{I}{A \cdot A^* T^2}\right) \tag{2.17}$$

Differentiating Eq. 2.17 with respect to "I" and re-arranging terms as: [80]

$$\frac{dV}{d(\ln I)} = IR_s + n\left(\frac{kT}{q}\right) \tag{2.18}$$

Eq. 2.18 plots a straight line for the forward bias I-V characteristics. The series resistance can be extracted from the slope of the dV/dln(I) versus I plot, while the intercept n(kT/q) is used to obtain the value of ideality factor. In order to find barrier height Cheung's function H(I) is defined as: [80]

$$H(I) = V - n\left(\frac{kT}{q}\right)\ln\left(\frac{I}{AA^* T^2}\right) \tag{2.19}$$

Using Eq. 2.17 in above equation:

$$H(I) = IR_s + n\phi_b \tag{2.20}$$

The plot of H(I) versus I is also a straight line, thus the barrier height can be determined from y-axis intercept of H(I)-I graph using value of ideality factor as determined from Eq. 2.18.

2.8.2 Tunneling mechanisms

The trap assisted tunneling (TAT) transport model is shown in fig 2.10 (a), which is considered as another dominant transport process in metal-semiconductor diodes. High defect densities and trap states located at the metal-semiconductor interface and within the depletion region are considered to enable electrons to flow from the semiconductor region to the metal. The tunneling current through the Schottky barrier diode is then given by: [79]

$$I_{tunnel} = I_{0(tunnel)}\left\{\exp\left(\frac{q(V - IR_s)}{E_0}\right) - 1\right\} \tag{2.21}$$

where $I_{o(tunnel)}$ is the tunneling saturation current and E_0 is a tunneling parameter expressed as:

$$E_0 = E_{00}\coth\left(\frac{E_{00}}{kT}\right)$$

E_{00} is related to material properties of the semiconductor as:

$$E_{00} = \frac{qh}{4\pi} \cdot \sqrt{\frac{N_D}{m_e^* \varepsilon_0 \varepsilon_r}}$$

where E_{00} is an energy related to the tunneling probability with q being the elementary charge, Planck's constant h, N_D being the donor concentration, and m_e^* being the effective mass of electrons. Trap assisted tunneling current density (J_{TAT}) is related to the electric field (**E**) by: [82]

$$\ln(J_{TAT}) = \ln(A) - \frac{B}{\mathbf{E}} \tag{2.22}$$

where A is a temperature dependent parameter and:

$$B = \frac{8\pi\sqrt{2qm *}}{3h} \phi_{t\_TAT}^{\frac{3}{2}}$$

ϕ_{t_TAT} is the trap activation energy with respect to conduction band and corresponding to TAT conduction process (as shown in fig. 2.10 a) which can be extracted from the slope of $\ln(J_{TAT})$ plotted versus 1/**E**. The trap assisted tunneling is a temperature dependent transport process since E_{00} depends on temperature. If the leakage current becomes more or less independent of temperature the current may be carried by Fowler-Nordheim tunneling (FNT).

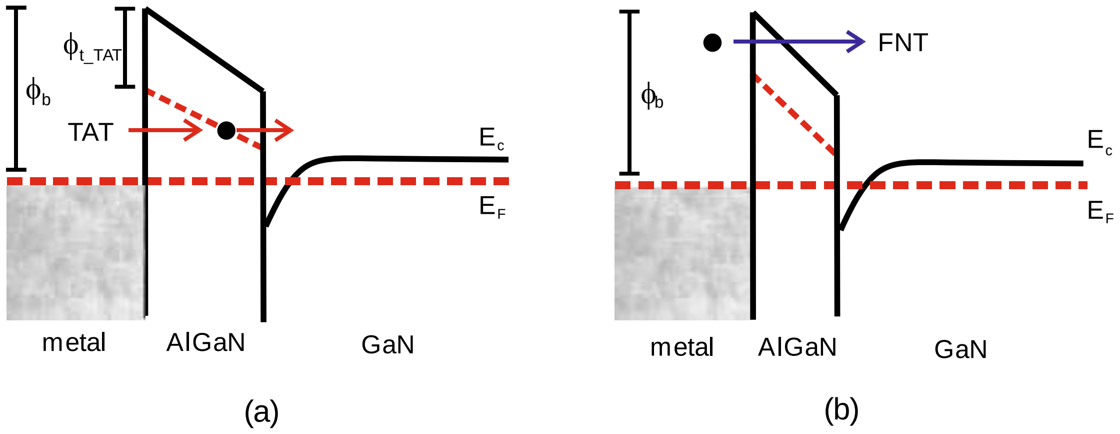

Figure 2.10: Schematic band diagram for two dominant transport mechanisms in GaN-based devices: **(a)** Trap assisted tunneling; and **(b)** Fowler-Nordheim tunneling.

The Fowler-Nordheim tunneling effect arises when the electron wave function penetrates through the triangular potential barrier into the conduction band of the semiconductor when the barrier thickness is below 10 nm [fig. 2.10 (b)]. The electric field (**E**) dependence of the Fowler-Nordheim tunneling current density (J_{FNT}) can be expressed as: [83, 84]

$$\ln\left(\frac{J_{FNT}}{E^2}\right) = \ln(C) - \frac{D}{\mathbf{E}} \tag{2.23}$$

where C is a proportionality constant and:

$$D = \frac{8\pi\sqrt{2qm*}}{3h}\phi_{eff}^{3/2}$$

while ϕ_{eff} is the effective barrier height for electrons following the Fowler-Nordheim tunneling conduction mechanism.

2.8.3 Frenkel-Poole effect

As described before defect related electronic states localized in nitride based devices give rise to frequently observed electron trapping phenomena. The physical properties of the trapping centers can be strongly affected by applying electric field. Thus field-assisted emission characteristics provide a unique way to determine electron dynamics through the trapping centers.[85] Frenkel-Poole (FP) emission refers to an electric field enhanced electron transfer mechanism by which an electrical insulator or semiconductor gets conducting. Therefore particularly in metal-oxide semiconductors or metal-insulator semiconductor heterostructures, macroscopic current-voltage measurements allow to determine if the Frenkel-Poole mechanism rules electrical conduction through an insulating layer.

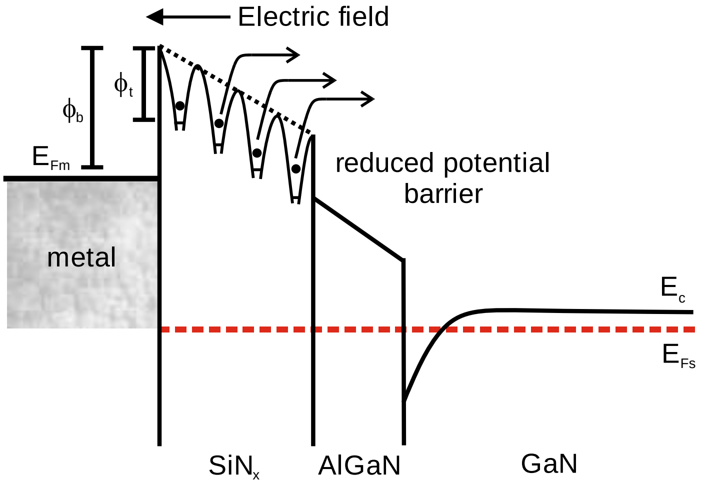

Figure 2.11: Schematic conduction band edge diagrams of GaN/AlGaN/SiN_x heterostructure for Frenkel-Poole emission. [82]

The local charge transport in field-assisted emission occurs from one trap state into a continuum of electronic states.[86] Generally it is assumed that the emission process is thermally activated and the electron or hole emission rate from the trap (e_t) into the conduction or valence band is related to the ionization energy E_i as, $e_t = A\,T^2 e^{-E_i/kT}$.[85] Figure 2.11 demonstrates the conduction band diagram for Frenkel-Poole conduction in MIS structure having multiple Coulombic traps. When an electric field is applied the potential barrier is lowered hence trapped electrons can escape from the dielectric layer and flow across the AlGaN/SiN$_x$ interface into the semiconductor conduction band edge. The current density associated with Frenkel-Poole emission is described as: [86]

$$J_{FP} = CE\exp\left[-q\left(\frac{\phi_t - \sqrt{\frac{qE}{\pi\varepsilon_0\varepsilon_r}})}{kT}\right)\right] \tag{2.24}$$

Above equation shows that for a current transport ruled by Frenkel-Poole emission, the ln(J/E) should be a linear function of $E^{0.5}$: [86]

$$\ln\left(\frac{J_{FP}}{E}\right) = m(T)E^{0.5} + b(T) \tag{2.25}$$

$$m(T) = \frac{q}{kT}\sqrt{\frac{q}{\pi\varepsilon_0\varepsilon_r}} \tag{2.26}$$

$$b(T) = -\frac{q\phi_t}{kT} + \ln(C) \tag{2.27}$$

In the presence of an applied field the barrier height decreases by an amount proportional to the square root of the applied electric field E.

2.9 Space charge effects in semiconductors

When applying a metal-semiconductor contact, charges are induced at the surface and hetero-interfaces which affect the electric field and the energy band distribution, and subsequently the electrical properties of electronic devices. The Schottky contact exhibits a rectifying behaviour as a consequence of a space charge region on the semiconductor region. Studying the capacitance-voltage (C-V) characteristics of a Schottky contact allows determining net carrier concentration, depletion layer width, trapping concentration and characteristics of electrically active centers in the bulk and near the surface of semiconductors.

The basic principle of C-V measurements works on the fact that the depletion or space charge region width changes with an applied bias [Figure 2.12].[87] However, the measured capacitance can be influenced by leakage current, electronic trap states in the sample or interface states. A dc bias applied to an n-type semiconductor with a donor concentration N_D changes the width of the space charge regime W by the amount dW as presented in fig. 2.12. The differential capacitance is defined as C = dQ/dV, where Q is the magnitude of the charge within the space charge region which determines the capacitance by applying an ac voltage of 10 to 20 mV with a frequency between 10 kHz to 1 MHz.[87]

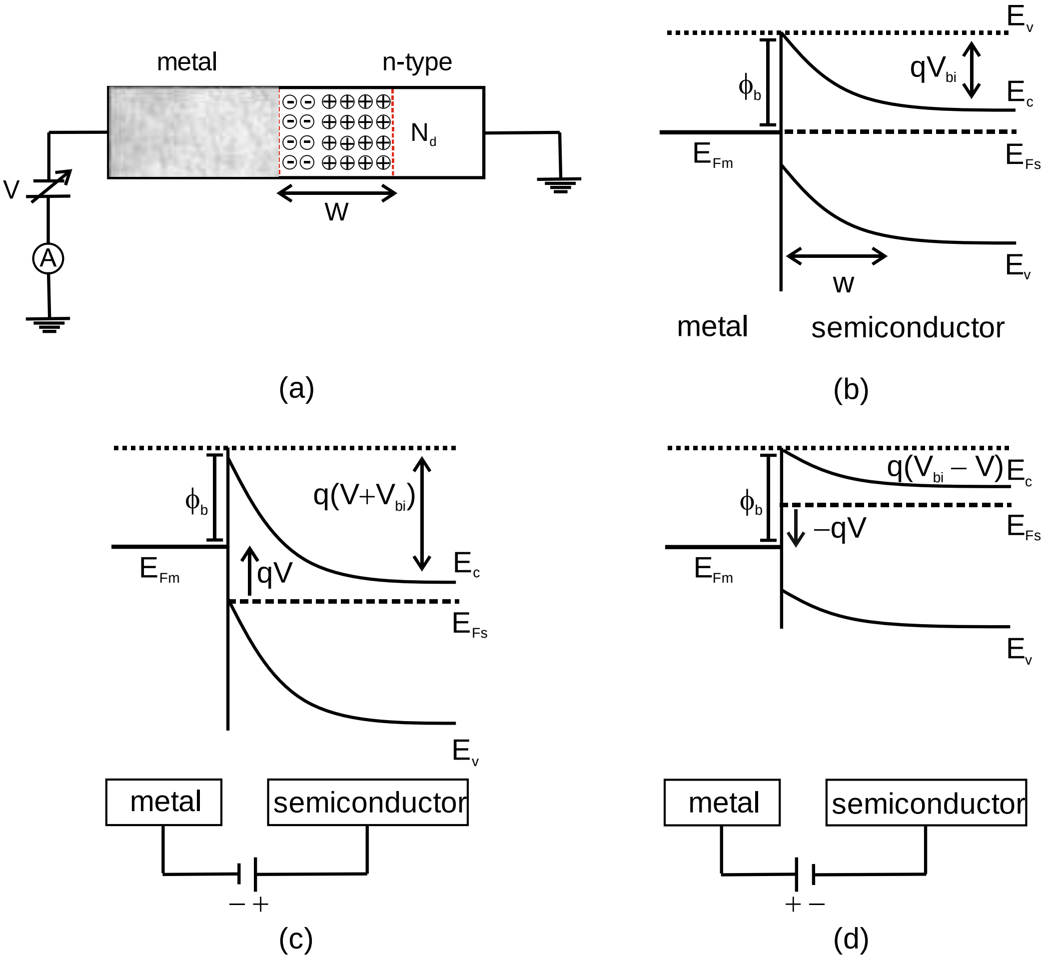

Figure 2.12: (a) A reverse-biased metal-semiconductor diode, **(b)** Metal-semiconductor junction for an applied voltage V=0; under reverse bias **(c)** and forward bias **(d)**. [87]

A p-n as well as a Schottky junction gets characterized by applying a reverse dc bias plus a sinusoidal ac voltage increasing from zero to a small amplitude of voltage (0 to ± *x* mV). The charging process of acceptors or donors adds a charge increment of magnitude dQ to the semiconductor which must be balanced by an equal but opposite charge increment to the metal to obtain overall charge neutrality. The semiconductor charge is given by: [87]

$$Q = eA \int_0^W (p - n + N_D^+ - N_A^-)\, dx \;\approx\; eA \int_0^W N_D^+ \, dx \qquad (2.28)$$

with the approximation for an n-type semiconductor that $N_A = 0$ and $p \approx n \approx 0$ and all donors are ionized. The charge increment slightly increases the width of the depletion regime. The depletion capacitance referred to the depletion regime can be obtained as: [87]

$$C = eA \frac{d}{dV} \int_0^W N_D^+ \, dx = eAN_D(W) \frac{dW}{dV} \qquad (2.29)$$

Thereby, the change in depletion capacitance (or space charge width) by imposing small change in the applied reverse bias determines a local value for the carrier concentration in the material. The barrier capacitance of the layer measured as a function of depletion width is expressed as:

$$C = \frac{\varepsilon_0 \varepsilon_r A}{W} \;; \quad \text{or} \qquad W = \frac{\varepsilon_0 \varepsilon_r A}{C} \qquad (2.30)$$

Hence, differentiating above equation with respect to voltage and substituting dW/dV into Eq. 2.29 net carrier concentration can be estimated as:

$$N_D(W) = \frac{2}{\varepsilon_0 \varepsilon_r e A^2 \left[\frac{d\left(\frac{1}{C^2}\right)}{dV}\right]} = -\frac{C^3}{\varepsilon_0 \varepsilon_r e A^2 \left[\frac{dC}{dV}\right]} \qquad (2.31)$$

For a homogeneously doped semiconductor the plot of $1/C^2$ versus reverse applied bias V is linear and the slope determines the net carrier concentration while the intercept gives the built-in voltage. The depth at which the doping density is evaluated is obtained from the dependence of space charge region width on the capacitance in accordance with Eq. 2.30. MOS, MIS capacitors and field effect transistors can also be used for C-V profiling, however the capacitance of the barrier layer (C_b) or an oxide layer (C_{ox}) must also be considered in the equation because of an additional gate voltage drop across the barrier or oxide layer. Eq. 2.31 can be directly applied to obtain device characteristics of heterostructures however the depletion depth can be obtained by introducing C_b or C_{ox} in Eq. 2.30: [87]

$$W = \varepsilon_0 \varepsilon_r A \left(\frac{1}{C} - \frac{1}{C_{ox}}\right) \qquad (2.32)$$

2.10 Analysis of trap states in GaN-based heterostructures

The trap states in GaN/AlGaN and GaN/AlInN heterostructures are systematically studied by capacitance or conductance measurements as both provide similar information of traps using equivalent circuit models. In this section, extraction of defect density distribution using these methods is explained.

2.10.1 High-Low frequency method

High-low frequency method was developed by Castagne and Vapaille by combining both low and high frequency capacitance values to calculate defect densities. It is based on the absence of any contribution of the defect states to capacitance at high frequency, thus no theoretical calculation is needed for evaluation. By comparing the low-frequency with the high-frequency capacitance the density of defects can be extracted from the C-V data. At sufficiently low frequencies traps and minority charge carriers are able to respond to the ac probe frequency. The trap density D_{trap} can be obtained using relation: [87, 88]

$$D_{trap} = \frac{1}{q^2}\left[\left(\frac{1}{C_{LF}} - \frac{1}{C_b}\right)^{-1} - \left(\frac{1}{C_{HF}} - \frac{1}{C_b}\right)^{-1}\right] \tag{2.33}$$

where C_b is the barrier capacitance or capacitance of the insulating layer in the case of MIS structures, C_{LF} is the capacitance measured at low-frequency, and C_{HF} is the values of device capacitance obtained at high-frequency. The zero bias capacitance is approximately equal to the barrier capacitance C_b, and is in ideal case unaffected by the frequency variations.[88]

2.9.2 Conductance method

Another sensitive technique developed by Nicollian and Goetzberger, is widely used to determine the trap density D_{trap} and emission times τ_{trap}. This technique is based on measuring the equivalent parallel conductance G_P of an MOS or MIS capacitor as a function of frequency and applied bias.[89] Since the surface capacitance depends strongly on the frequency and applied bias voltage, bias and frequency dependent conductance-voltage (G/ω-V) profiling has been used to measure trap densities. The conductance method can extract D_{trap} in the depletion and weak inversion regime of band structure.

Fig. 2.13 illustrates simplified equivalent circuit models representing the basic principles of MOS conductance technique. The impedance of MOS or MIS capacitor is measured by a bridge across the capacitance terminals. [87, 90] Here C_{ox} is the capacitance of insulating layer which is equal to the barrier capacitance C_b, semiconductor capacitance is C_s, and C_{trap} is the trap capacitance. Resistance R_{trap} represents the loss mechanism during the capture and emission of carriers from the trap states. [87]

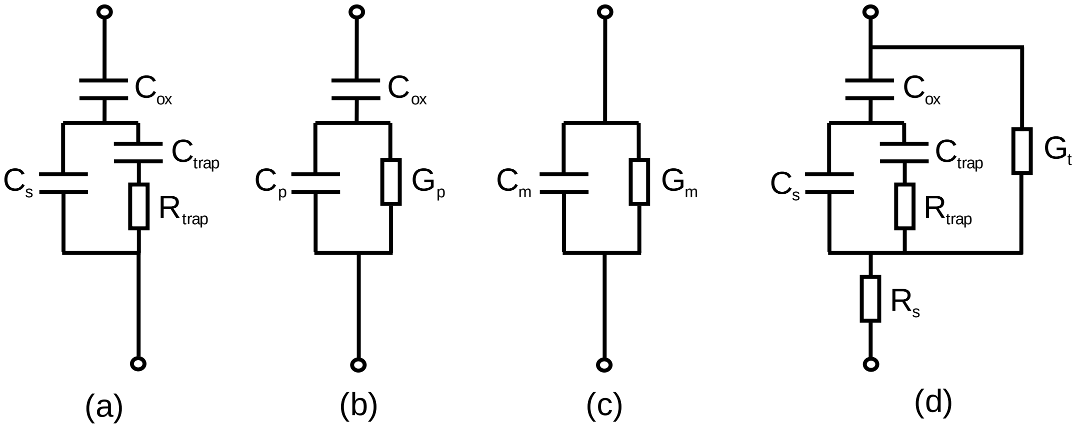

Figure 2.13: Equivalent circuits for conductance measurements; **(a)** MOS-C with trap time constant $\tau_{trap} = R_{trap} C_{trap}$, **(b)** simplified circuit of (a), **(c)** measured circuit, **(d)** including series R_s resistance and tunnel conductance G_t. [87]

Parallel capacitance C_P and parallel conductance G_P are expressed as: [87, 90]

$$C_p = C_s + \frac{C_{trap}}{1 + \left(\omega\tau_{trap}\right)^2} \tag{2.34}$$

$$\frac{G_p}{\omega} = \frac{q\omega\tau_{trap}D_{trap}}{1 + \left(\omega\tau_{trap}\right)^2} \tag{2.35}$$

where $C_{trap}=q^2 D_{trap}$, $\tau_{trap}=R_{trap}C_{trap}$, and $\omega=2\pi f$ is the angular frequency, τ_{trap} is the time constant of trap states. The trap density D_{trap} and τ_{trap} are the two main extracted parameters after fitting above two equations.

Chapter 3

Experimental Techniques

3.1 Introduction

In this chapter the basic measurement techniques used for the characterization of GaN buffer layers doped with different impurities, GaN/AlN/AlInN and GaN/AlGaN heterostructures are explained. The chapter discusses x-ray diffraction (XRD) analysis, photoluminescence and scanning probe microscopy (SPM) techniques to describe structural, optical and surface properties of GaN structures. Electrical characterization methods like current-voltage, Hall-effect, capacitance-voltage and defect characterization techniques are described as tools to determine electrical properties of GaN/AlN/AlInN and GaN/AlGaN heterostructures.

3.2 X-ray diffraction analysis

X-ray diffraction is the primary, non-destructive tool to analyse crystalline material for determining various parameters like lattice constants, material composition, crystallographic orientation, strains, and dislocation densities.[91] To evaluate the screw and edge components of threading dislocations in GaN layers x-ray omega (ω) scans are determined.

The analysis of epitaxial layers is executed using the mosaic model of crystals where the layer is supposed to be made of small crystallites called mosaic blocks. The lateral and vertical dimensions of these mosaic blocks are described by definite coherence lengths parallel and perpendicular to the growth plane respectively.[92] However these crystallites or mosaic blocks are not perfectly vertically and laterally aligned to each other. The out-of-plane rotation of the blocks is expressed by the angle of tilt that the crystallites have with respect to the surface normal, while the in-plane rotation around the surface normal is the mosaic twist.[93] Edge and screw component of dislocations are directly related to mosaic twist and tilt values because at the coalescence boundary of two mosaic blocks they are introduced to close the misorientation gaps between the crystallites. Their density thus depends on the twist and tilt values which broaden the Bragg diffraction curves.[92]

Figs. 3.1 (a, b) show the geometry of x-ray analysis measurements to obtain tilt and twist distributions for out of plane and in-plane rotations respectively. In order to measure the x-ray diffraction profile for an out of plane rotation, the detector is set at a Bragg angle 2θ and the sample is tilted with respect to the beam path plane (χ). Incident x-ray beam hits the sample at the angle ω, and diffracted by 2θ from the sample surface were then measured with the x-ray detector.[94] The ω-scan curves measure the scattered x-ray intensity as a function of omega. For a perfect crystal, the ω-scan will plot a very sharp peak broadened by the limited penetration depth of the primary beam. Any broadening in excess of this natural broadening is associated to defects like mosaicity, dislocations etc. [92]

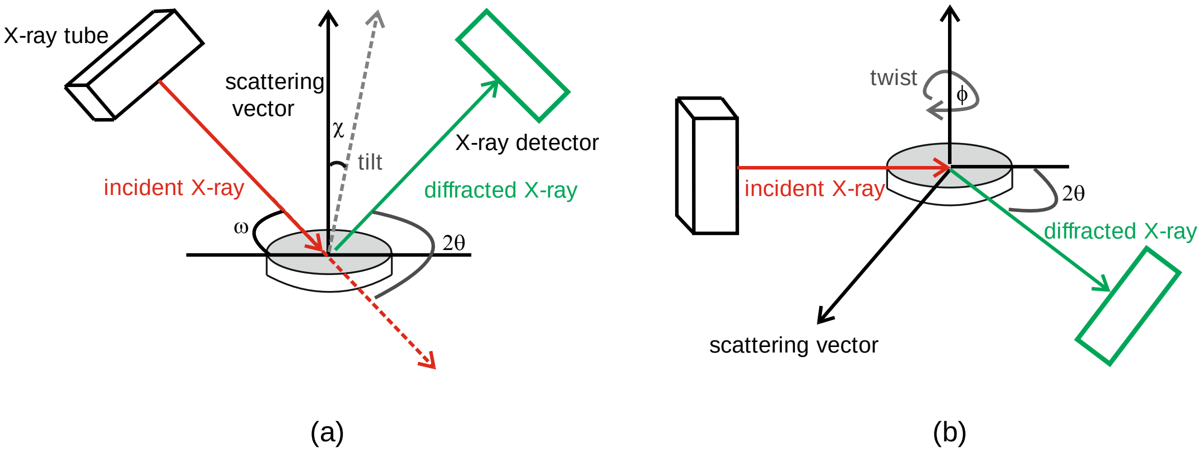

Figure 3.1: X-ray geometry for (a) out of plane rotation for tilt; and (b) in-plane rotation for twist determination.[94]

The FWHM of the omega scan for in-plane rotation is the measurement of the twist which is not as simple as for the out-of-plane component. To obtain in-plane measurements the grazing incidence geometry (GID) is used as depicted in figure 3.1 (b), where a parallel incident x-ray beam strikes the sample surface through a very small critical angle, while the sample is rotated around the surface normal (ϕ) until a particular lattice plane lying perpendicular to the surface fulfils the Bragg condition.[95]

In this work, x-ray diffraction measurements have been carried out providing a measure of tilt and twist in the samples by the full-width at half maximum of out-of-plane and in-plane GaN-related reflections recorded in ω-scan mode, respectively. The result of out-of-plane measurements around the GaN(0002) reflection is used for determining the tilt. The twist angle is obtained from in-plane measurements around the GaN($10\bar{1}0$) using grazing incidence diffraction geometry. By applying a small angle grain boundary model for the GaN layer structure one can calculate the screw (ρ_s) and edge (ρ_e) components of mixed dislocations from the FWHM using Eq. 3.1 and 3.2: [92]

$$\rho_s = \frac{\Delta\omega_s^2}{4.35 b_s^2} \tag{3.1}$$

$$\rho_e = \frac{\Delta\omega_e^2}{4.35 b_e^2} \tag{3.2}$$

Herein, $\Delta\omega_s$ and $\Delta\omega_e$ denote the FWHM of the in-plane GaN (e.g. GaN($10\bar{1}0$)) and the out-of-plane GaN (e.g. GaN(0002)) reflections, respectively. b_s and b_e are the Burger's vectors of screw- and edge-type dislocations ($b_s = 0.5189$ nm and $b_e = 0.3189$ nm) in GaN.[92]

3.3 Scanning probe microscopy imaging

A family of surface analysis tools is designed to image atomic structures on the nanoscale by scanning an atomically sharp probe over a surface at a distance of a few angstroms or nanometres. Electric force microscopy (EFM) and scanning surface potential microscopy (SSPM) are the scanning probe microscopy based techniques, applied to determine the localized electronic properties and potential distribution of different GaN sample series along with topography.[96, 97]

3.3.1 Electric force microscopy

This is a secondary imaging mode derived from atomic force microscopy (AFM) used to explore electric field gradient distribution above the sample surface, by probing the local electrostatic interaction between a conductive tip and locally charged regions on a surface.[97] Since the SPM-based techniques provide high spatial resolution characterization of the electronic properties of the III-nitrides, the potential mapping can be affected by short-range forces between tip and sample.[96] In order to minimize the influence of the topography on the EFM signal, the imaging is performed in the lift mode which is a two-pass scan method as illustrated in fig. 3.2. In the first pass the surface topography is measured in tapping mode, and then the tip lifts up to a certain scan height above the surface where electrostatic interactions dominate. Following the previously recorded topography, the electric field gradient distribution above the sample surface is mapped while both an AC voltage (V_{AC}) and a DC voltage (V_{DC}) are applied to the AFM tip.[54, 98]

When a V_{DC} signal is applied between the cantilever tip and the sample to modulate the electrostatic field, the cantilever is vibrated near the surface by a small piezoelectric element near its resonant frequency. By varying an applied bias, the electrostatic force gradient is changed which causes tip deflection during scanning. The corresponding change in the resonance frequency and phase of the cantilever provides the EFM image contrast.[99]

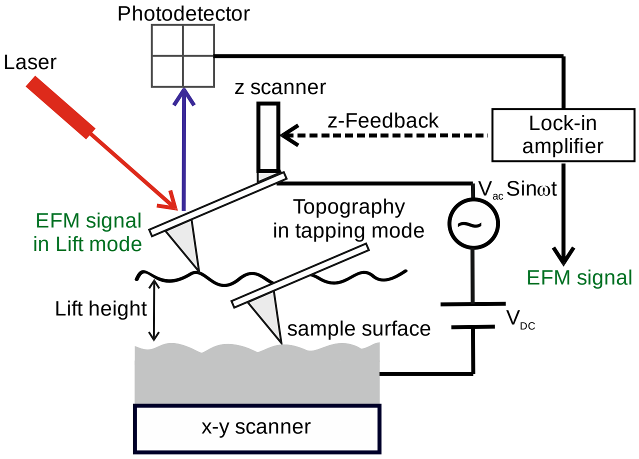

Figure 3.2: Schematic diagram for EFM operation in lift mode

Since the metal probe and sample with the separation between them forming a capacitor, the capacitive electrostatic force arises due to the difference in work functions between tip and semiconductor surface. This force is proportional to the net surface charge density and change of contact potential $V_{contact}$ as given by: [60, 97]

$$\mathrm{Force} = \frac{q_S\, q_t}{4\,\pi\,\varepsilon_0\, z^2} + \frac{1}{2}\cdot\frac{dC}{dz}\left(V_{applied} - V_{contact}\right)^2 \tag{3.3}$$

The first term is a constant electrostatic force whereas the second term depends on the difference of the applied tip voltage $V_{applied}$ and the contact potential $V_{contact}$. dC/dz is the capacitance gradient of the capacitor formed by the sample-tip system, z is the tip-sample distance which is 30 nm in these experiments, q_S is the surface charge, q_t the charge induced on the tip. A contact potential difference arises between the AFM tip and a semiconductor due to difference in work functions which is described by the following equation: [35]

$$eV_{contact} = \phi_m - \chi_{GaN} - \Delta E_{fn} - \Delta\phi \tag{3.4}$$

According to Eq. 3.3, a minimum of the EFM signal should exist for tip voltages equal to the contact potential difference. This can be identified by minimum contrast in respective images of either the EFM-amplitude or phase signal. Figure 3.3 schematically illustrates the band structure of GaN showing the contact potential $V_{contact}$ with reference to metal work function.[96] Here ϕ_m is the metal work function for the tip coating, χ_{GaN} is the electron affinity of the surface, and $\Delta\phi$ is the resulting band bending in the semiconductor material due to surface charges.

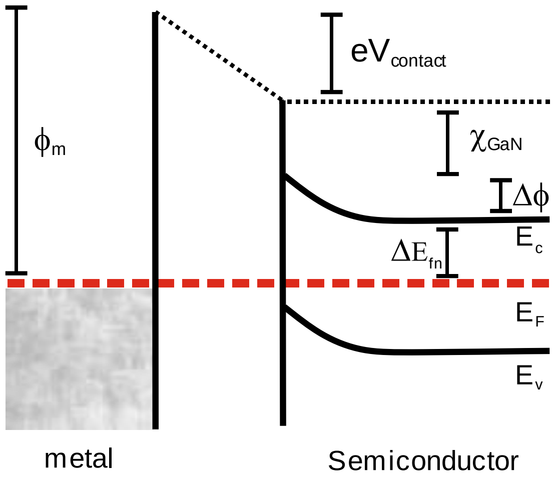

Figure 3.3: Band structure of GaN exhibiting the contact potential with respect to metal probe

The SPM characterizations presented in this thesis were performed on a commercial instrument Digital Instruments Dimension 3100 Nanoscope using a metal coated etched silicon probe (MESP) yielding the tapping mode resonance frequency of 70 kHz. The EFM measurements were performed on conductive and semi-insulating GaN layers. The change in contrast as a function of applied bias was equally observed in both amplitude and phase signals. However, in order to avoid artifacts and influence from topography, the EFM-phase signal images were chosen. The root mean square (rms) roughness is calculated from the phase signal across 3x3 μm^2 scan areas at different tip voltages and fitted parabolic curves to these data for a determination of the contact potential.

3.3.2 Scanning surface potential microscopy

The basic principle of SSPM is similar to EFM with enhanced DC bias feedback control system as shown in figure 3.4. A bias voltage $V_{DC}+V_{AC}\sin\omega t$ applied to the tip, with close to the cantilever resonance frequency, generates a total force which is combination of electrostatic and capacitive forces. This force can be nullified by applying a DC voltage on the tip through a built-in feedback control loop. The applied bias is equal in magnitude and opposite in direction as the potential difference between metal probe and sample so that it counteracts the electrostatic force. This external DC bias that nullifies the electrostatic force multiplied with the elementary charge is the value of surface potential.[35]

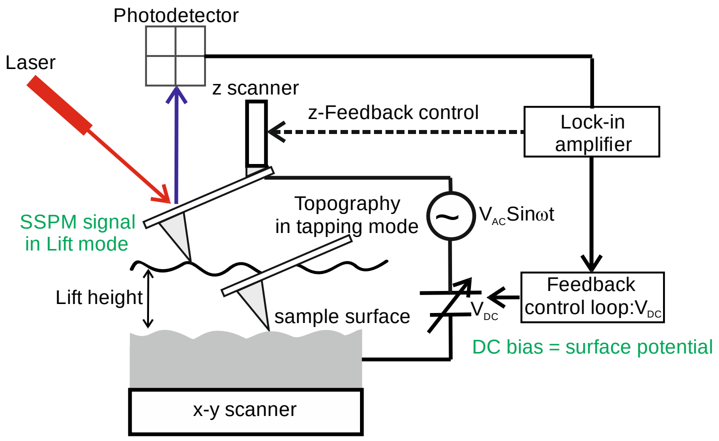

Figure 3.4: Operation scheme of an AFM along with a corresponding SSPM measurement. A topographic image is obtained in tapping mode, while the surface potential is subsequently measured in lift mode at a constant distance to the surface.

The output signal shows two contributions from the surface-tip interaction and can be described by: [34, 59]

$$V_{DC} = V_S + \frac{q_S\, C}{4\, \pi\, \varepsilon_0\, z^2} \cdot \frac{dz}{dC} \tag{3.5}$$

It can be seen from Eq. 3.5 that in the absence of coulomb’s charges the output signal V_{DC} is equal to the surface potential V_S of the layer. As the output signal counteracts the force exerted from a surface charge onto the cantilever tip, a positive SSPM signal corresponds to a negative surface charge and vice versa.

The SSPM measurements were conducted on etched GaN surfaces and the surface potential mapping of the sample along with corresponding height profile is obtained in lift mode at a constant lift height of 30 nm above the surface. The etch pit density was calculated from simultaneously recorded AFM images.

3.4 Hall-effect measurements

To extract the sheet resistance R_{sh}, carrier concentration n_s and electron mobility μ of samples the Hall-effect measurements were applied. The contact geometry of the investigated samples was a square of size 1 cm x 1 cm with contacts at the four corners as shown in fig. 3.5. The ratio of the voltage applied across the terminals C and D, and the current flowing through terminal A and B determine the resistance $R_{AB,CD}$. Similarly the value for $R_{BC,DA}$ is obtained while the resistivity of the material in the absence of magnetic field is defined by the relation:

$$\rho = \frac{\pi d}{\ln 2} . \frac{\left(R_{AB,CD} + R_{BC,DA}\right)}{2} \cdot f \tag{3.6}$$

where d is the thickness of semiconductor film, and f is the correction function.

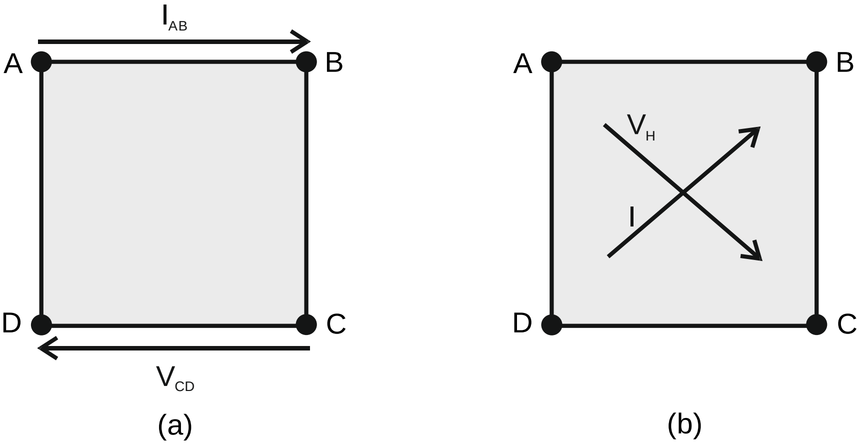

Figure 3.5: Schematic illustrations of sample geometry with current and voltage directions for **(a)** resistivity; **(b)** Hall-effect measurements.

When a magnetic field **B** is applied perpendicular to the sample surface while a current I is flowing across it, the resulting Lorentz force will deflect charge carriers perpendicular to both magnetic field and current flow. This will give rise to a Hall voltage (V_H) of magnitude IB/qnd as illustrated in fig. 3.5 (b).[100, 101] Thus by measuring the V_H and from the known values of I, B, d, ρ, and q, the carrier concentration and mobility of charge carriers can be obtained accordingly as: [101]

$$n_s = \frac{IB}{V_H de} \tag{3.7}$$

$$\mu = \frac{V_H d}{IB\rho} \tag{3.8}$$

3.5 Current-voltage characterization

Electrical performance of semiconductor devices is generally analyzed in terms of current-voltage characteristics. The current-voltage measurements have been performed on C- and Fe-doped GaN buffer structures and GaN/AlN/AlInN heterostructures. From the analysis of

I-V data, the breakdown field strength of semi-insulating GaN layers, current transport processes in GaN/AlN/AlInN structures and important device parameters are evaluated.

In order to investigate the compensating nature of carbon and iron dopants in GaN buffer structures, the I-V measurements were conducted on resistive GaN layers at room temperature using a Keithley 4200-SCS semiconductor system. For these characterizations two 180 µm x 100 µm Ti/Al/Mo/Au contacts at a distance of 20 µm were evaporated on the sample surface and annealed at 850 °C for 50 s in nitrogen ambient. No mesa etching or surface passivation was applied. Figure 3.6 (a) explains the contact geometry of these measurements.

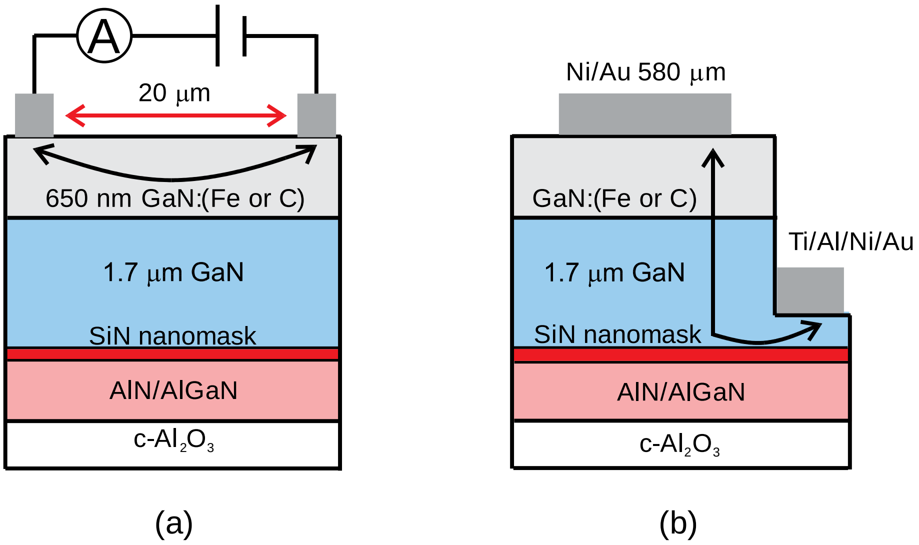

Figure 3.6: Schematic of the test device structures for lateral and vertical I-V measurements

Vertical current transport through the device structures was explored by executing conductivity measurements in dark ambience from room temperature to 400 K using another I-V measurement setup illustrated in figure 3.7 (c). Here, test devices consisted of a mesa structure 580 µm in diameter with a Ni/Au top contact. The mesa structures were etched by inductively coupled plasma reactive ion etching (ICP-RIE) using a chlorine/argon plasma down to the un-intentionally Si-doped region of the GaN layer above the SiN nanomask. A dot-like bottom contact out of Ti/Al/Ni/Au (20/50/15/100 nm) metallization was deposited 5 µm apart from the mesa boundary. The bottom contact was annealed at 750 ºC in a N_2 ambient for 1 min, while the Ni/Au (10/50 nm) metal stack was realized without subsequent annealing resulting in Schottky-type contact properties. Fig. 3.6 (b) illustrates the schematic diagram of the GaN buffer samples doped with iron or carbon that is used to obtain I-V characteristics in vertical contact layout.

In electrical characterization of GaN/AlN/AlInN heterostructures, the FET device structures were processed according to fig. 3.7 (a) with gate widths of 50 µm, gate lengths of 6 µm and source/drain contact size of 50 µm x 100 µm. The metallization of ohmic contacts (source/drain) was obtained by depositing a Ti/Al/Ni/Au (20/50/15/100 nm) metal stack using an electron beam and thermal evaporation setup and subsequently alloyed by rapid thermal annealing at 650 °C while the gate contact consisted of a Ni/Au (15/100 nm) metal stack. Here test devices were not passivated which results in relatively high values of gate leakage current. A Keithley 4200-SCS semiconductor system was used to characterize the transistor device characteristics. The transfer characteristics of FETs at room temperature were obtained by plotting the drain currents as a function of the gate-source voltage.

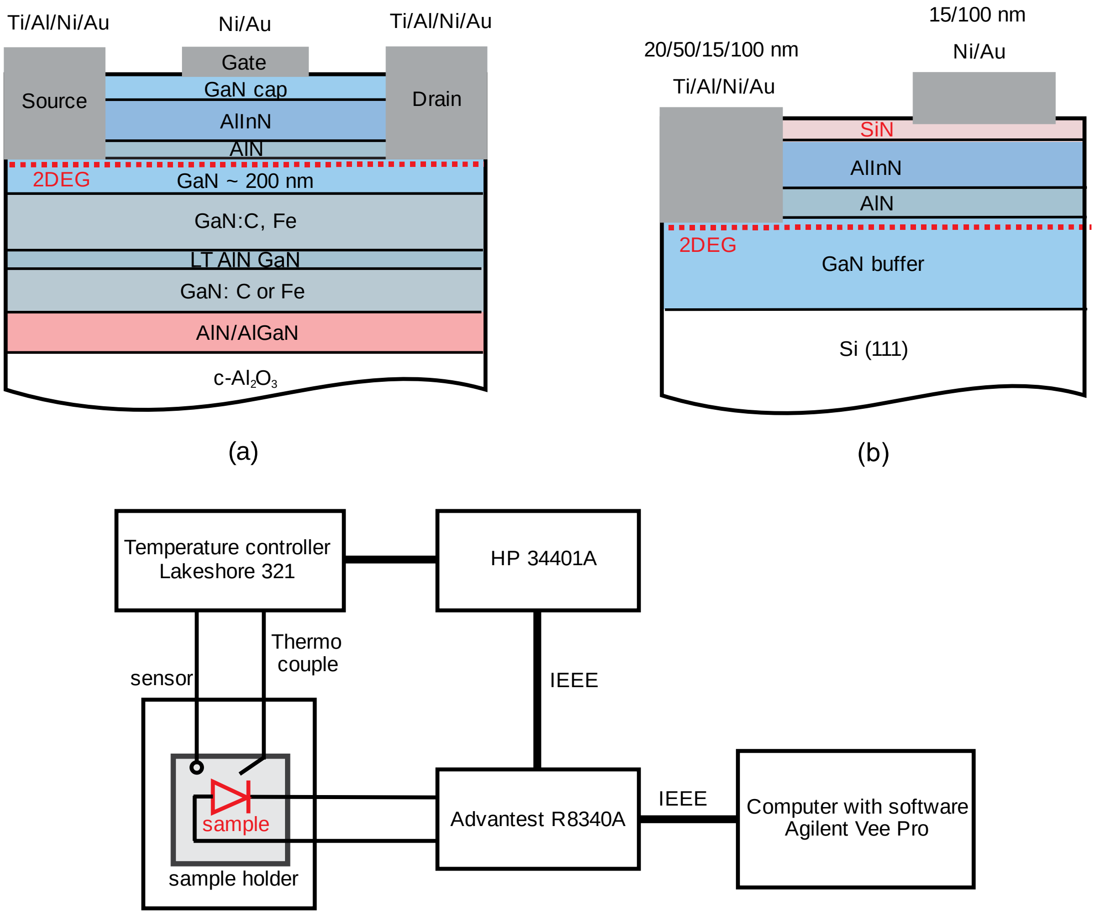

(a) (b)

(c)

Figure 3.7: (a, b) Schematic of the test device structures for electrical characterization of GaN/AlN/AlInN heterostructures; and **(c)** block diagram of the I-V measurement setup.

To investigate electrical properties of SiN passivated GaN/AlN/AlInN structures, an ohmic Ti/Al/Ni/Au (20/50/15/100 nm) and a Schottky Ni/Au (10/50 nm) contact were deposited according to fig. 3.7 (b). The ohmic contact was 1 mm in diameter and annealed at 400 °C in a nitrogen atmosphere, whereas the Schottky contact was un-annealed metal dots of 300 µm in diameter. Current-voltage characteristics at various temperatures were obtained using a commercial I-V measurement setup Advantest R8340A along with a temperature controller Lakeshore 321 and a multimeter HP34401A, following the arrangement described in figure 3.7 (c). These electrical investigations were carried out in the range of 50 - 400 K using a closed-cycle type refrigerator based on ^{4}He cryostat under high vacuum environment. The closed system was first cooled down to the temperature about 50 K and then required characteristics were recorded by controlling temperature in the desired temperature range.

3.6 Thermally stimulated current spectroscopy

With regard to view the electrical properties of defects in GaN based devices, thermally stimulated current (TSC) measurements on GaN buffer and GaN/AlN/AlInN heterostructures were conducted. To obtain the TSC spectra, the samples were cooled from room temperature to 50 K at a constant reverse bias, and then illuminated at 50 K by above band gap light for 20 minutes to fill electron and hole traps. After turning off the light source, the TSC spectra were recorded in the dark upon heating at a constant rate of 2K/min.[102] By gradually increasing the temperature thermally stimulated current was produced due to carrier emission from traps.[103] For reference, a dark current spectrum without any optical excitation of carriers was also obtained in the same temperature range and at similar reverse applied voltage, while the reference data was subtracted from the measured TSC current data.

3.7 Capacitance-voltage and admittance measurements

The capacitance-voltage profiling is a complementary method to Hall-effect measurement to extract net donor concentration ($N_D - N_A$) as a function of depletion depth. On the other side, voltage dependent admittance spectroscopy where the capacitance measurements are carried out as a function of frequency, yields quantitative information on defects within band gap of a semiconductor.[104] Admittance and C-V characteristics were obtained for GaN/AlN/AlInN FET structures grown with Fe- or C-doped buffer layers and SiN passivated GaN/AlN/AlInN heterostructure, to provide a qualitative investigation of the space charge region. The device schematics and contact geometry were similar to that used for I-V measurements as depicted in figs. 3.7 (a, b). For FET device structures measurements were recorded between gate and drain contacts.

Figure 3.8 demonstrates the block diagram of the measurement setup for two contact geometries used in admittance and C-V profiling. Bias and frequency dependent capacitance-voltage and admittance measurements were carried out using an LCR precision meter HP4282A. The C-V data was collected at different frequencies while the admittance measurements were obtained in the frequency range from 20 to 1 MHz at different reverse applied biases. The current-voltage characteristics were recorded prior to measuring the C-V profiles to verify the quality of the contacts.

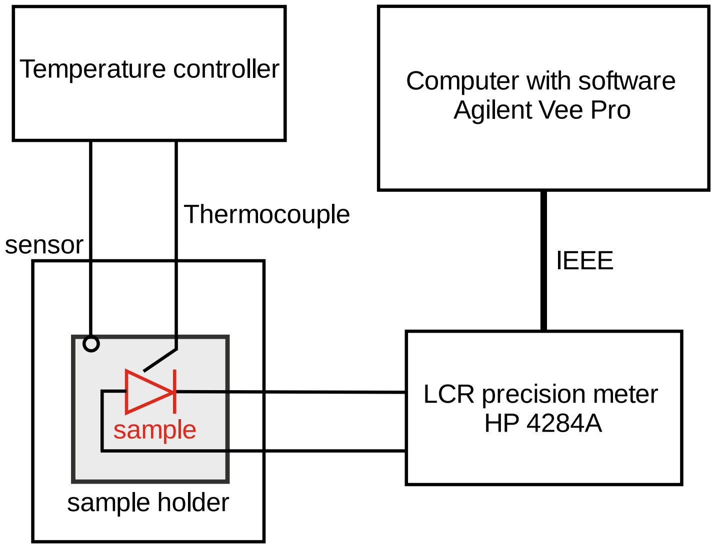

Figure 3.8: Block diagram of C-V measurement setup

3.8 Photoluminescence spectroscopy

This is a non-destructive tool used for the characterization of optically-active defects within the band gap of semiconductor. Photoluminescence spectroscopy involves the excitation of semiconductor film with photons of energy greater than the band gap energy ($h\nu > E_g$) of that material. The incident photons generate electron-hole pairs, while the recombination energy of these electrons and holes results into non-radiative and radiative emissions. The optical characterization of the carbon and iron doped GaN buffer structures under study were performed by PL spectroscopy, where optical spectra were obtained at 10 K, using a HeCd laser operating at wavelength of 325 nm as excitation source.

The point defects in GaN, for example native defects, impurities, and their complexes significantly contribute to the luminescence and may influence the optical properties of a material. Photoluminescence spectrum of undoped GaN typically exhibits a broad yellow luminescence band at about 2.2 eV, in addition to the near band edge emission due to bound and free exciton transitions and their phonon replicas.[105] Although the YL band is the most reviewed defect luminescence in GaN, it is still not clear that how many type of defects contribute to this notorious yellow luminescence emission. Many experimental results reveal the origin being a native compensating defects, like carbon (C_N) and its complex with other impurities, or $V_{Ga}O_N$ defect with two different charge states as shown in figure 3.9.[73, 106] The green luminescence (GL) band at about 2.4 eV is attributed to another charge state of the same defect responsible for the YL band, however the GL band is usually observed in high quality GaN samples, containing low density of carbon and oxygen defects.[106]

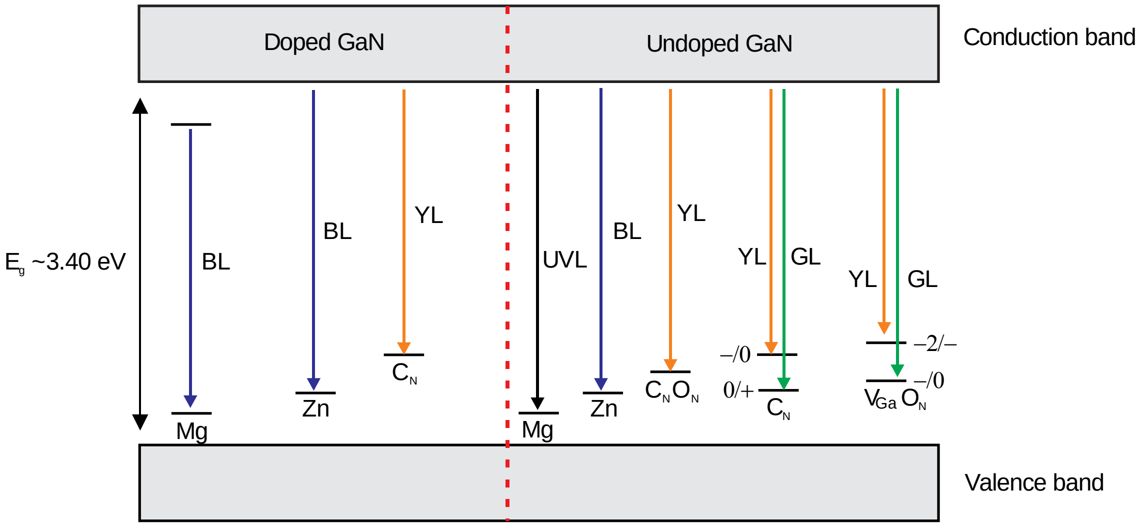

Figure 3.9: Radiative transitions associated with common doping impurities and unintentionally introduced defects in GaN. [105, 106]

Another defect related band often seen in the low-temperature PL spectrum at about 2.9 eV is the blue luminescence band, while the PL spectrum of undoped GaN sometimes contain a red luminescence (RL) band is at about 1.8 eV. Due to a large value of hole capture cross section, the BL band in undoped GaN is frequently argued to be associated to the Zn_{Ga} acceptor.[105] Blue PL spectrum peaking around 2.9 eV is also seen in highly Mg-doped MOVPE grown GaN layers.[107] An ultraviolet luminescence (UVL) band with peak at around 3.26 eV is often observed in GaN samples, and is related to Mg_{Ga} acceptor related transitions. Fig. 3.9 shows some radiative transitions associated with common doping impurities and unintentionally introduced defects with the positions of energy levels within the band gap of GaN.[105, 106]

3.9 Transfer length measurement

High contact resistance (R_c) of an electronic device is detrimental to the performance because it drops the drain current and enhance the turn-on resistance of the device. Therefore it is essential to determine the contact resistance between a metal and a semiconductor. Transfer length measurement (TLM) technique is an important tool to estimate the contact resistance and sheet resistance (R_{sh}) of the devices. This method involves an array of metal-semiconductor contacts of similar contact size separated by different spacings (L_1, L_2, etc) as shown in figure 3.10.

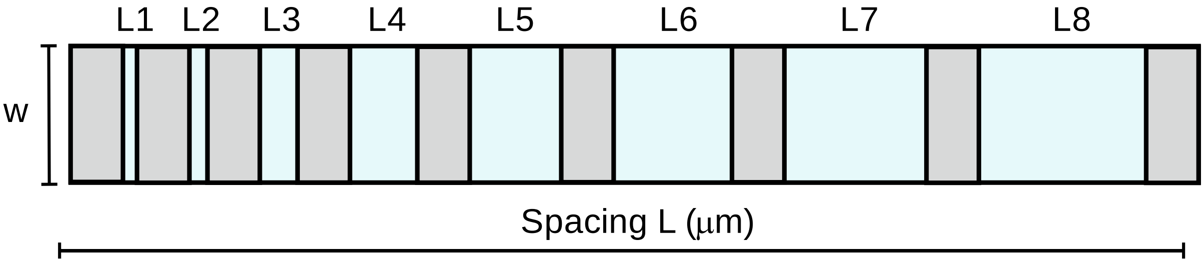

Figure 3.10: Schematic diagram of the TLM structures

The resistance measured between each contact pair is plotted against the spacing distance to extract the contact parameters R_{sh} and R_c. The total resistance (R_T) is related to contact and sheet resistances by the expression as: [108, 109]

$$R_T = 2R_c + L * \frac{R_{sh}}{W} \tag{3.9}$$

The total resistance versus the spacing (L) plot typically exhibits a linear behaviour and the intercept $2R_c$ returns the value of the contact resistance. In this work the sheet resistances estimated from the slopes adopting TLM method has been compared to the R_{sh} values measured by traditional Hall-effect.

Chapter 4

Properties of semi-insulating GaN buffer layers

4.1 Introduction

Highly resistive GaN layers are indispensable to mitigate buffer leakage in GaN-based power FETs. In this chapter undoped, C-doped and Fe-doped GaN buffer layers are characterized with a focus on structural, electrical, and surface properties as well as compensation effects. Undoped, Si- or Ge-doped (n-type), and p-type GaN (Mg-doped) GaN layers are also explored in the context of their surface and local electronic behaviour. The results of conductive GaN layers are used as a reference for comparison with the properties of semi-insulating GaN structures. Moreover properties of extrinsically C-doped GaN layers, achieved using propane as precursor source, are studied in comparison with intrinsically C-doped series grown by changing growth temperature and V/III-ratio. X-ray diffraction analysis, scanning probe microscopy techniques, photoluminescence spectroscopy, current-voltage, and temperature dependent conductivity measurements have been used to explore various properties of GaN layers upon carbon and iron doping.

4.2 Sample details and growth information

Semi-insulating carbon and iron doped GaN samples were grown by metalorganic vapor phase epitaxy in a horizontal AIXTRON AIX-200/4 RF-S reactor on 2-inch c-plane sapphire substrates using trimethylgallium (TMGa) and ammonia precursors with H_2 as carrier gas. The layer arrangement contains a sequence of a thin low temperature AlN nucleation and AlN/AlGaN buffer layers, followed by 1.7 μm thick, fully coalesced un-doped GaN layer above a SiN in situ nanomask.[50] On top of this layer, Fe- and C-doped layers of about 650 nm in thickness were grown with different dopant concentrations. Undoped and conductive GaN layers were also grown as reference for comparative investigations with semi-insulating GaN layers where the top layer is doped with Ge- or Si- to obtain n-type conductivity and Mg- for p-type conductivity. Figure 4.1 shows the schematic diagram of templates used in this chapter for different investigations.

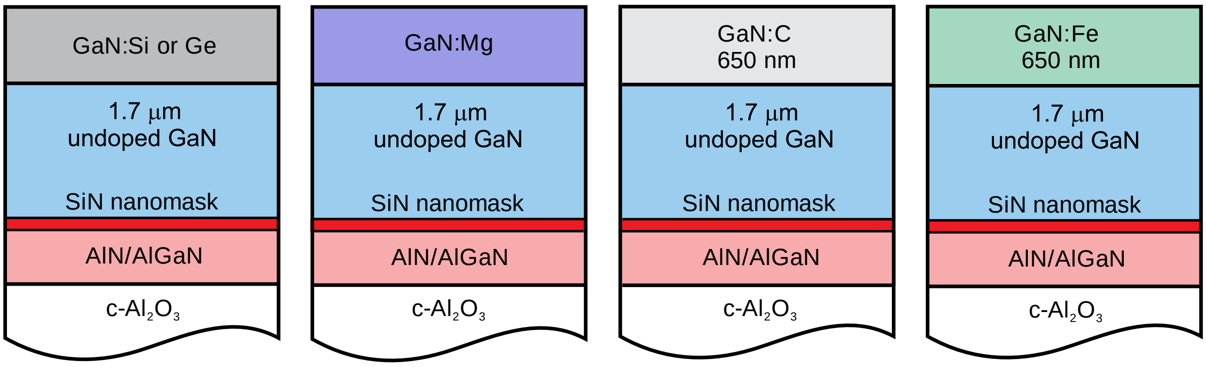

Figure 4.1: Scheme of the layer arrangement of conductive and semi-insulating GaN samples

All doped layers except the Mg-doped ones were grown at a V/III ratio of ~900, a substrate pocket temperature of 1070 ºC as determined with a Laytec EpiTT in-situ instrument, and a total pressure of 200 mbar. Extrinsic carbon doping is achieved using diluted propane (C_3H_8:H_2, [C_3H_8]=10 %) gas with a molar flow of 0 - 6 mmol/min (amount of propane) as precursor source during growth of GaN:C layers. The flow of TMGa and NH_3 was 96.4 µmol/min and 89 mmol/min respectively. The bis-cyclopentadienyl-iron (Cp_2Fe) molar flow rate for Fe doping was varied between 0.23 and 10.3 nmol/min in the top GaN:Fe layer. For a comparison with precursor-based GaN:C, intrinsically C-doped GaN samples were also grown. There, the carbon doping was achieved by reducing the growth temperature and V-III ratio. Ge doping was achieved using isobutylgermane (IBGe) as Ge source in the molar flow range from 7 to 31.6 µmol/min, while diluted silane (SiH_4) (100 ppm SiH_4, in 6N H_2) in the molar flow range from 4 to 16 µmol/min was used for silicon doping.[50] For p-type doping the bis-cyclopentadienyl-magnesium (Cp_2Mg) molar flow was varied from 3.25 to 65 pmol/min at a V/III ratio of ~3700, a substrate temperature of 990 ºC and a total pressure of 200 mbar. The flow rates of TMGa and NH_3 were 24 µmol/min and 90 mmol/min respectively. The details of the growth parameters for propane based C-doped GaN, Fe-doped and the conductive GaN series are given in table 4.1.

In all sample series a SiN nanomask was grown proceeding to the growth of undoped GaN buffer layer because this technique is found to improve structural and optical properties of GaN significantly.[110] A part of this work is devoted to determine the influence of the SiN nanomask on structural and electrical properties of GaN layer while the thickness of the SiN was controlled by changing the growth time from 0 to 150 s. Sample details for these investigations are described in section 4.3.3.

Table 4.1: Growth parameters for Fe-doped, propane based C-doped, n- and p-type GaN

Samples	V/III ratio	substrate temperature	TMGa/ NH_3 flows	doping source	molar flow rate
Fe-doped	930	1064 ºC	0.096/ 90 mmol min^{-1}	Cp_2Fe	0.23 - 10.3 nmol/min
C-doped	900	1070 ºC	0.096/ 89 mmol min^{-1}	C_3H_8	0 - 6 mmol/min
Ge-doped (n-type)	900	1070 ºC	0.096/ 90 mmol min^{-1}	IBGe	7 - 31.6 µmol/min
Si-doped (n-type)	900	1070 ºC	0.096/ 89 mmol min^{-1}	SiH_4	4 - 16 µmol/min
Mg-doped (p-type)	3700	990 ºC	0.024/ 90 mmol min^{-1}	Cp_2Mg	3.25 - 65 pmol/min

The carbon and iron contents in the top GaN layer for the intentionally doped samples were determined by secondary-ion mass spectrometry (SIMS) using Cs^+ as a primary ion source, for which a carbon detection limit of $2x10^{17}$ cm^{-3} was determined. Concentrations of carbon atoms in the range from $8x10^{17}$ cm^{-3} to $6.7x10^{18}$ cm^{-3} are found while the Fe-contents in the series vary from $1.1x10^{17}$ cm^{-3} to $5x10^{18}$ cm^{-3}. Undoped GaN has a carrier concentration of $5x10^{16}$ cm^{-3} as determined by C-V measurements.

For AFM, EFM and SSPM investigations, all samples were cleaned using acetone and isopropanol, rinsed in de-ionized water and blown dry with N_2 before measurement. The visibility of different dislocations was enhanced by a wet chemical etching treatment in hot phosphoric acid (H_3PO_4) at 200 ºC for 10 minutes to identify different types of dislocation by AFM.[41, 111] The unetched GaN surfaces were used for EFM measurements while the etched samples were further used to obtain high resolution AFM and SSPM mapping profiles near dislocations.

4.3 Structural properties of GaN

4.3.1 Surface morphology

X-ray diffraction analysis and scanning transmission electron microscope (STEM) measurements were executed to analyze the samples with carbon doping for dislocations. A cross-section STEM specimen of a highly C-doped sample (C = $4.6x10^{18}$ cm^{-3}) was prepared to obtain in addition a cross-sectional view of the GaN:C layer. The propagation of dislocations from the undoped GaN buffer layer into the C-doped GaN region is depicted in figure 4.2 (a). Threading dislocations are revealed as dark lines using bright field imaging along the $[1\bar{1}00]$ zone axis. The initially high density of dislocations at the sapphire/AlN interface is effectively reduced with the help of an in-situ deposited SiN nanomask. Within the undoped GaN buffer layer, the dislocation density drops to a value of about $2x10^9$ cm^{-2} due to three-dimensional island growth promoting dislocation annihilation. There is no discernible boundary between the C-doped and undoped GaN material and dislocations do not change their propagation direction. In summary there are no visible changes in the dislocation structure upon C-doping.

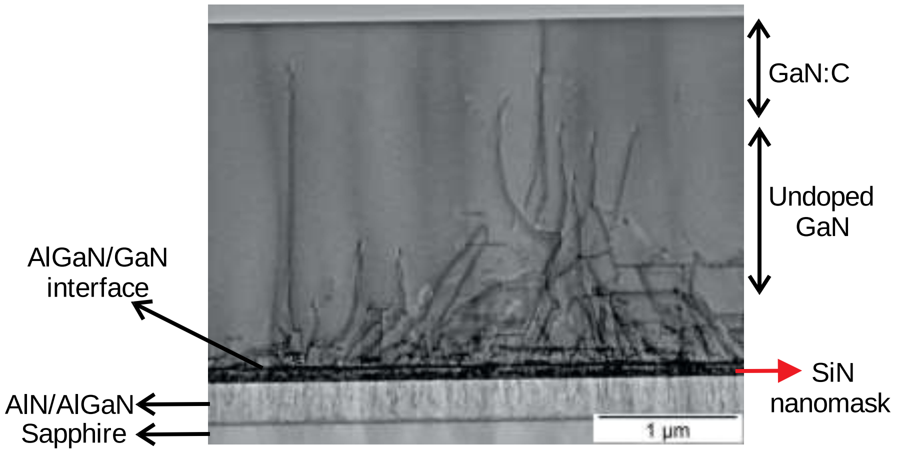

(a)

Figure 4.2: (a) Cross-section TEM view along the $[1\bar{1}00]$ zone axis of a GaN:C sample with (C = $4.6x10^{18}$ cm^{-3}); **(b)** Comparison of edge- and screw- components of dislocations obtained by XRD and AFM measurements plotted as a function of doping content and dopant type. In fig. (b) for simplicity AFM EPDs measured only for C-doped GaN series are plotted.

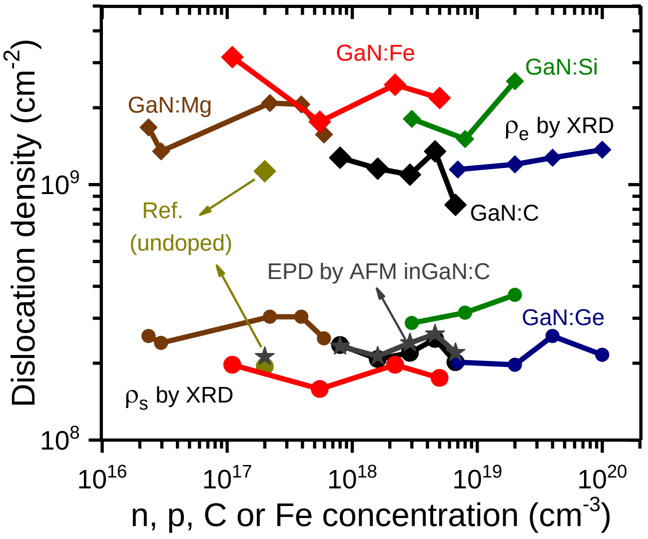

(b)

Screw- (ρ_S) and edge- (ρ_e) components of dislocations are obtained from full width at half maximum of XRD omega scans of out-of plane (0002) and in-plane ($10\bar{1}0$) reflections for GaN layers using Eqs. 3.1 and 3.2. Furthermore, the etch pit densities (EPDs) are also determined from AFM images of area 5x5 μm^2 by counting the hexagonally shaped pits related to screw- or mixed- type dislocations (discussed in next section). The densities of edge and screw type dislocation as a function of doping concentration are plotted in figure 4.2 (b). It is obvious that the edge-type dislocation densities measured by XRD are around 10^9 cm^{-2}, which is about one order of magnitude higher than the screw-type dislocation densities. More importantly, dislocation densities are not dependent on doping level and doping type.

The values of edge-type dislocation densities are in the same range of that obtained from TEM characterization. While the etch pit densities for carbon doped GaN series determined by AFM are close to the density of screw component of dislocations acquired from XRD measurements, the pure edge type dislocations in AFM images are not resolved (see section 4.3.2). In fig. 4.2 (b) only for carbon doped GaN samples, EPDs obtained by AFM are plotted however for all sample series the values lie in the same range. These findings are in good agreement with literature.[112, 113] The structural analysis suggests an overall good structural quality of carbon and iron doped samples in the doping range of up to $5x10^{18}$ cm^{-3}.

4.3.2 Defect etching

To investigate correlations between the surface morphology of different GaN samples and to estimate the density of structural defects which terminate at the surface (e. g. dislocations), AFM topographic measurements were analyzed. All GaN samples exhibit similar surface features. However the root mean square roughness values of semi-insulating layers are higher than for conductive samples.

Figs. 4.3 (a, b) show the surface morphology of un-etched C-doped GaN surface with C = $4.6x10^{18}$ cm^{-3} and Fe-doped GaN layer with Fe = $5x10^{18}$ cm^{-3} respectively. The AFM images of 3x3 μm^2 area exhibit well-arranged steps characteristic for a two dimensional growth regime. For C-doped GaN samples, rms values for the surface roughness on a 3x3 μm^2 area increase with carbon concentration from 0.26 nm for the undoped reference sample to 0.32 nm for an heavily C-doped GaN layer (C = $4.6x10^{18}$ cm^{-3}). According to the topographic contrast of AFM height images, the growth steps at the surface are assigned to bright areas while the small dark pits or depressions are associated to the termination of surface steps at dislocations.[41] Because the dislocations intersect the layer surface, the termination of dislocations at the surface results in small pits which can be observed in high resolution AFM images.[114]

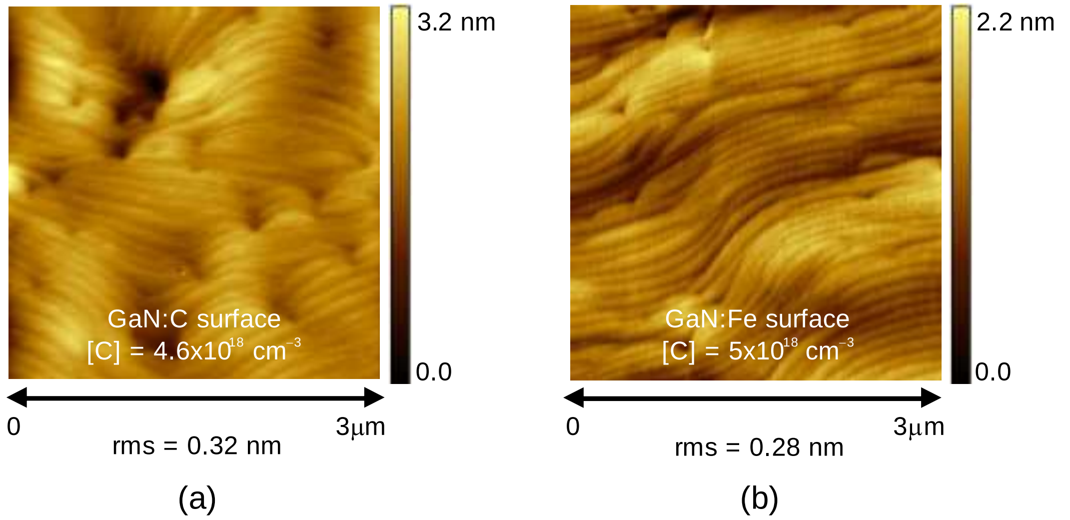

Figure 4.3: 3x3 µm^2 AFM images: **(a)** un-etched GaN:C layer with C = 4.6x10^{18} cm^{-3}; and **(b)** GaN:Fe layer with Fe = 5x10^{18} cm^{-3}.

The tapping mode AFM images of GaN layers described in figure 4.3 show surface pits or depressions however the dimension and morphology of these pits in un-etched samples are not well distinguishable in AFM measurements. Hence all samples were etched in hot phosphoric acid at 200 °C for 10 minutes to enhance their visibility.[41, 111] In figs. 4.4 (a, b) respectively, 2x2 µm^2 AFM image of the un-etched and etched GaN:C layers with C= 4.6x10^{18} cm^{-3} are presented.

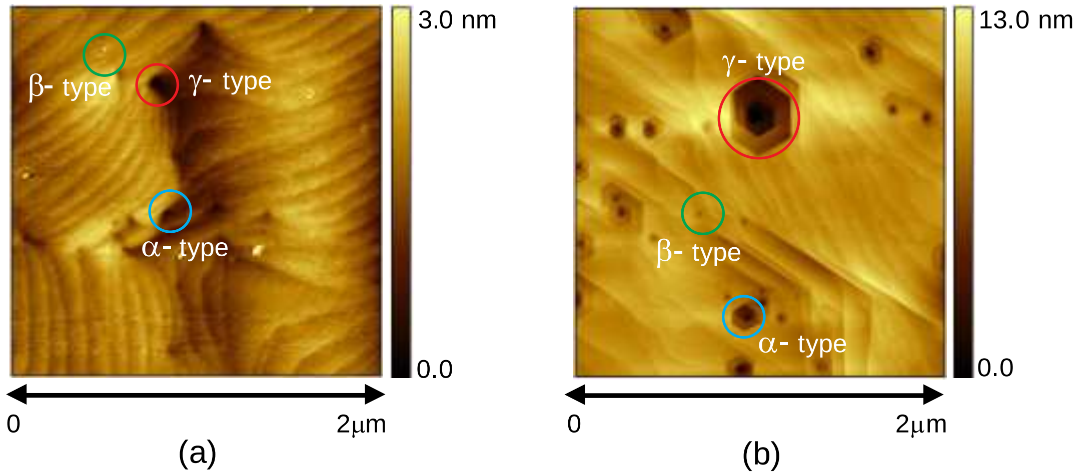

Figure 4.4: **(a)** 2x2 µm^2 AFM image of the un-etched GaN:C layer with C= 4.6x10^{18} cm^{-3}; **(b)** 2x2 µm^2 AFM image of the etched GaN surface.

Three kinds of dislocation related pits, labeled as α, β, and γ can be identified as shown in fig. 4.4 (a). For the un-etched GaN surface, α- and γ-pits are associated with the termination of growth steps or terrace structures whereas β-pits appear as small depressions on terraces.[111, 115] The morphology and size of the α- and γ-pits changes after hot wet etching while the β-type pits exhibit no significant change except a slightly increase in size. The etched surface in fig. 4.4 (b) indeed shows hexagonally shaped pits (α- and γ-) of different diameters and small dark spot like depressions (β). The anisotropic wet etching mechanism that enlarges the size of the pits helps in classifying different kinds of dislocations according to the individual etch pit structure and size.[41, 111]

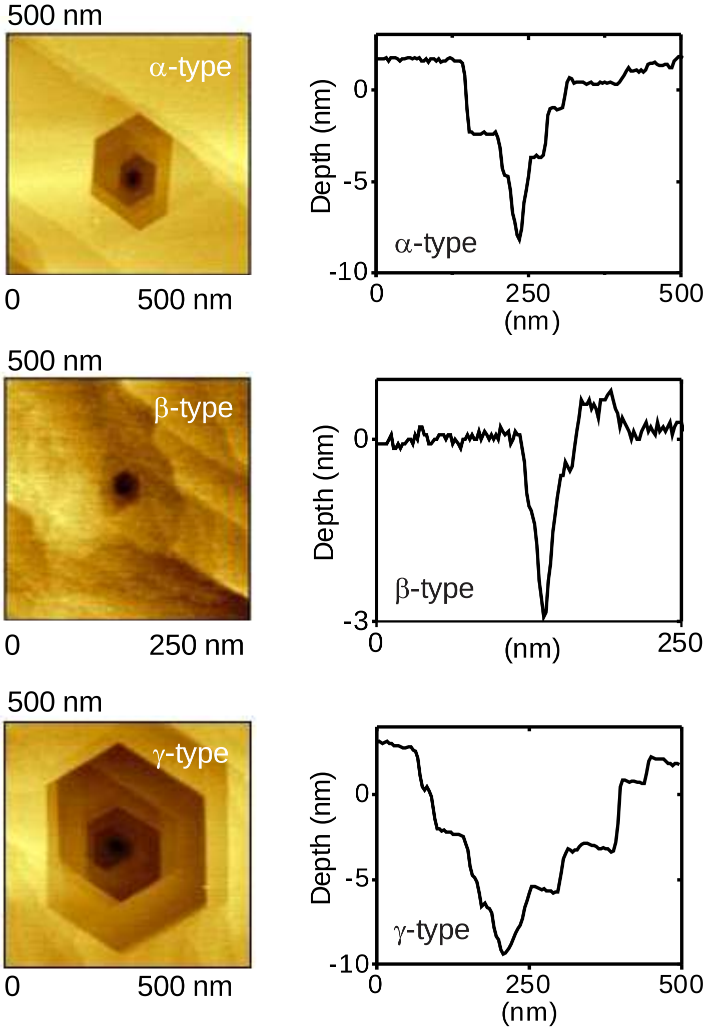

Figure 4.5: Schematic depth profiles of α-, β-, and γ-type etch pits

In figure 4.5 the individual surface morphologies for each pit type are shown on the left and respective depth profiles as obtained from line scans across each etch pit type are given to the right. Etching tends to enlarge the size of α- and γ-pits revealing few spiral growth steps, which can be related to termination of mixed or screw- dislocations at GaN surface.[111, 115] In contrast, the size and shape of β-type pits is not strongly altered by the etching treatment. As these pits are independent of growth steps namely appear on terraces only, their origin can be attributed to edge-type dislocations.[33, 116] However pure edge dislocations in our AFM images are not well resolved due to their smaller size, thus there is a possibility that hexagonal pits may contain clusters of edge type dislocations.

Most of the hexagonal shaped pits (around 70 %) observed in all samples are of α-type which can be classified as either screw- or of mixed- kind. The respective joint dislocation density with screw- or mixed-type character is estimated by counting the α- and γ-pits in 5x5 μm^2 AFM images of wet-etched undoped and carbon-doped samples. The dislocation densities are in the range of (2-2.6) x 10^8 cm^{-2}, independent of doping concentration [Fig. 4.2 (b)]. The comparison validates the assignment of hexagonally shaped pits seen in AFM images to screw-component dislocations as similar densities of about $\rho_s \sim (2\text{-}3) \times 10^8\ cm^{-2}$ are obtained both by XRD and AFM measurements. For β-type pits which might be related to edge-type dislocations, the etch pit counting method is not reliable enough due to their smaller size which yields in an underestimation of the pit density.

4.3.3 Influence of SiN nanomask on properties of GaN

Reduction of threading dislocations is pivotal for improving the structure quality of GaN films to achieve high performance devices. The deposition of a thin SiN layer alleviates structural defects and improves structural quality of GaN layers. In this section the effect of SiN nanomask on surface and electrical properties of GaN layer is explored. The details of investigated samples are described in table 4.2. All undoped GaN samples of this series follow the same layer sequence as shown in fig. 4.1, except for the different deposition times (between 0 to 150 s) of the SiN nanomask.

A crystallographic analysis by XRD omega scans of out-of plane (0002) and in-plane $(10\bar{1}0)$ reflections for GaN layers with different SiN growth times is illustrated in figure 4.6. It is notable that the FWHM for out-of-plane and in-plane reflections decreases with longer deposition time of the nanomask. The broad curves for sample A without a nanomask as shown in figs. 4.6 (a, b), result in large FWHM values and are in agreement with a high dislocation density typically observed for such simple sample structures. Whereas the sharper peaks indicate a reduced dislocation density after the insertion of a SiN nanomask.[41, 117]

Table 4.2: Structural and electrical parameters of samples determined from XRD, AFM and Hall-effect measurements as a function of SiN deposition time.

Sample	SiN deposition time (s)	ρ_s (10^8 cm^2)	ρ_e (10^8 cm^2)	AFM EPD (10^8 cm^2)	μ_H (cm^2/Vs)	n_{sh} (10^{17} cm^{-3})
A	0	8	570	20		
B	75	0.9	7.2	2.3	151	3.74
C	100	1.1	5.1	1.5	228	3.62
D	125	1.8	8.3	1.4	238	4.73
E	150	1.5	3.9	1.1	286	4.85

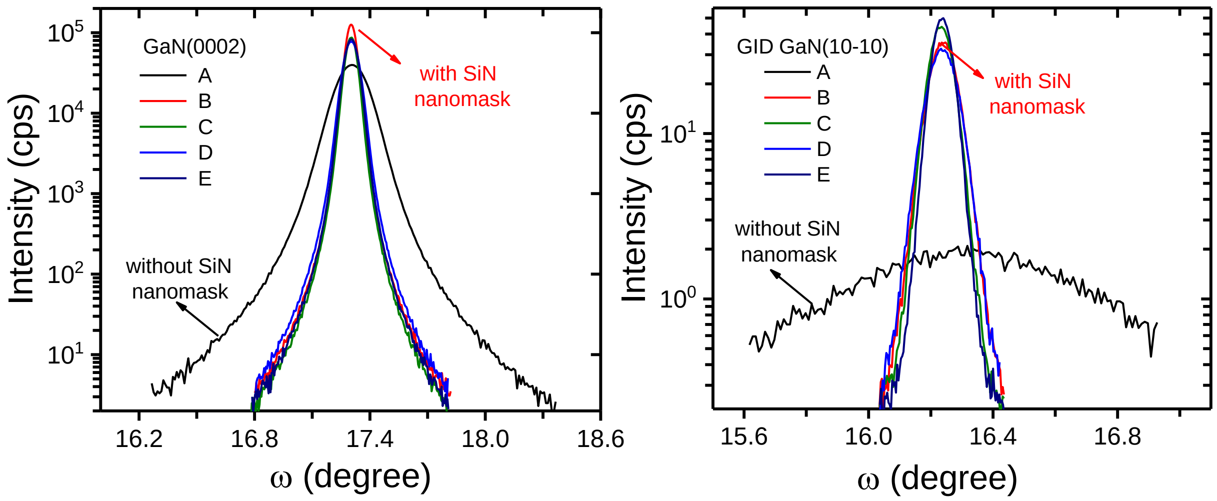

(a) (b)

Figure 4.6: (a, b) FWHM of x-ray ω-scans for (0002) and ($10\bar{1}0$) reflections for sample series detailed in table 4.2.

The screw and edge components of dislocations were quantitatively determined from the FWHMs of omega scans for respective (0002) and in-plane ($10\bar{1}0$) reflections using Eqs. 3.1 and 3.2. For sample A without any SiN nanomask, the measured density of edge component of dislocations (ρ_e) is above 10^{10} cm^{-2} while the dislocation density for screw components (ρ_s) is found to be in the range of 10^9 cm^{-2}. On the other hand, densities of both types of dislocations from samples B to E with SiN nanomask are significantly lower than for reference sample A as presented in table 4.2 and plotted in fig. 4.7 (c).

The AFM topography images of samples A and E, without and with SiN nanomask deposited for 150 s are shown in figs. 4.7 (a) and (b) respectively. The AFM image of the sample without nanomask shows an irregular GaN surface with poor quality. The reference sample (A) contains a high degree of surface pits which corresponds to a high density of threading dislocations, whereas GaN layers with SiN nanomask reveal much smoother and more uniform surfaces with a few intermittent pits.[117] There is a substantial improvement in the surface morphology after the insertion of a SiN nanomask. The density of submicron pits is found to be reduced, while the root mean square roughness is decreased from 0.74 nm to 0.23 nm for the reference sample and a GaN layer grown with a SiN nanomask deposited for 150 s, respectively.

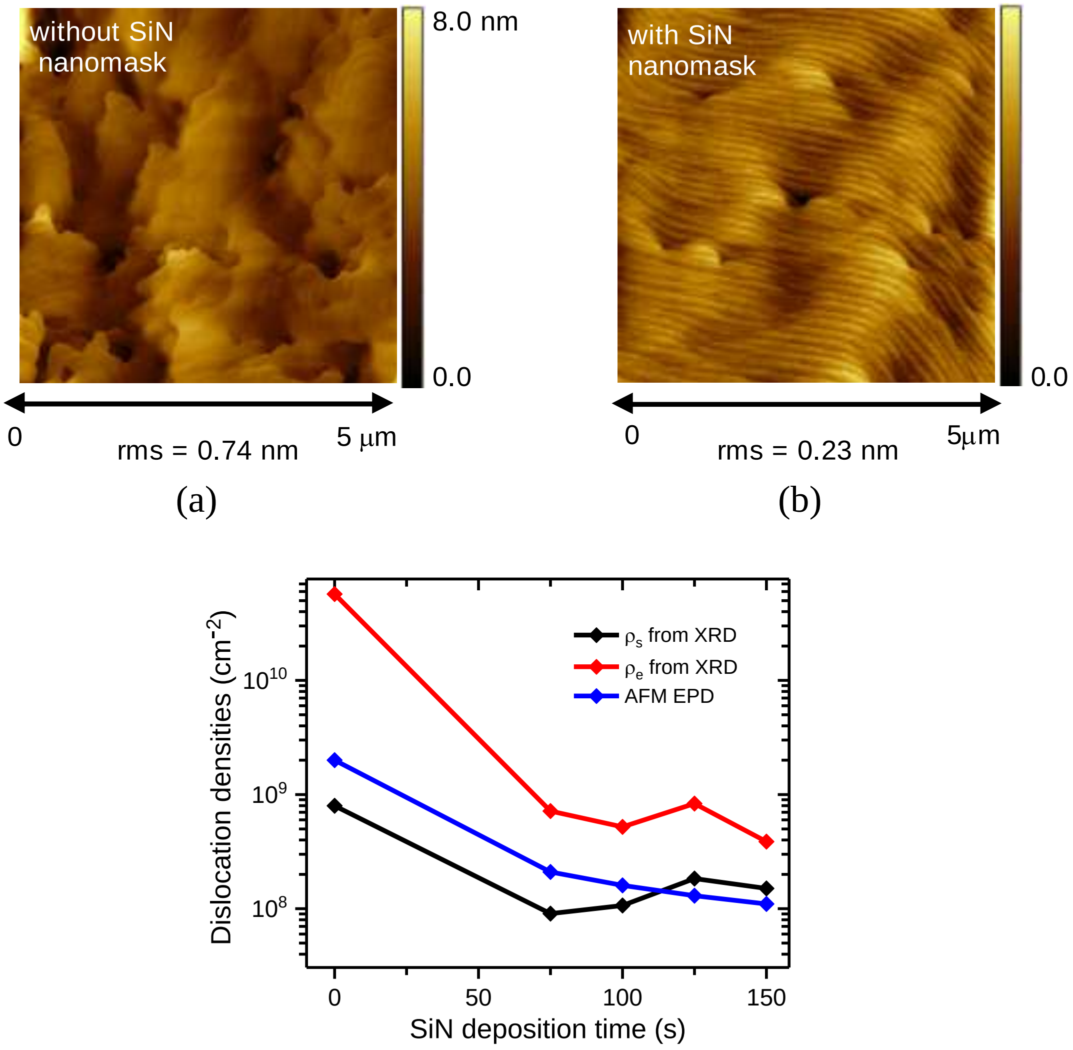

(a) (b)

(c)

Figure 4.7: 5x5 µm^2 AFM topographic images for GaN **(a)** without SiN nanomask; **(b)** with SiN nanomask deposited for 150 s (sample E); **(c)** EPD determined by AFM, and screw-type and edge-type dislocation densities determined by XRD as a function of SiN deposition time.

The etch pit density measurement is also used to obtain the dislocation density of the GaN samples. Wet etching treatment carried out on samples reveals hexagonally shaped pits as discussed in section 4.3.3, which are counted on 5x5 μm^2 AFM images to calculate etch pit densities. Fig. 4.7 (c) and table 4.2 compare the values of screw- and edge- type dislocation densities determined by XRD to the EPDs as a function of SiN deposition time. There is a decrease in dislocation densities after inserting a thin SiN nanomask however ρ_e is always higher than ρ_s. Kim et al.[110] also found reduction in threading dislocation density from $3.21 x 10^9$ cm^{-2} to $9.7 x 10^8$ cm^{-2} after a SiN mask deposition.

The Hall-effect measurements are performed on 1x1 cm^2 samples in van der Pauw contact geometry with four Indium dots at the edges of samples as illustrated in fig. 4.8 (a). The In dots are not surface contacts but, due to their position at the edges, they come in contact with the nanomask layer. Therefore Hall-effect parameters may have a contribution from the nanomask as well as the GaN epilayer. Hall mobilities (μ_H) are observed to be increasing from 151 cm^2/Vs (for sample B) to 286 cm^2/Vs (for sample E) with SiN deposition time, which can be associated to a better crystallographic quality deduced from the decrease of the ω-FWHM of the in-plane and out-of plane GaN Bragg reflections and an increase in Si-doping level.[118] Undoped GaN layers exhibit an increase in sheet carrier concentration (n_s) and decrease in sheet resistance with enhanced deposition times of the SiN mask as shown in fig. 4.8 (b).

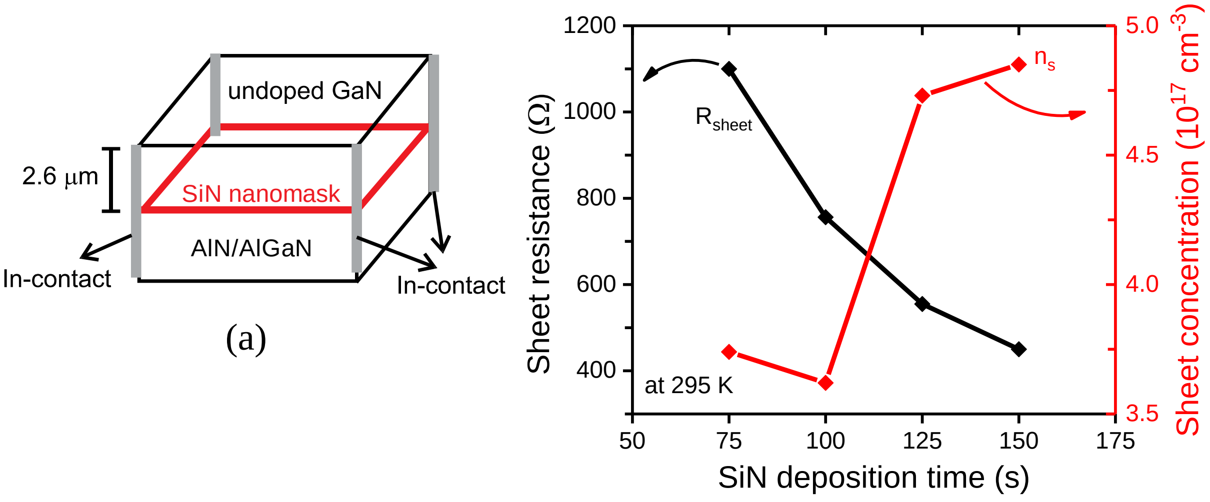

(a)

(b)

Figure 4.8: (a) Contact schematic of In-dots for Hall-effect measurements, **(b)** Sheet resistance and sheet carrier concentration.

The values of Hall mobilities and sheet carrier densities are described in table 4.2. The reference GaN sample without a SiN nanomask has large surface roughness and is supposed to have a specific resistivity of more than 10^6 Ω-cm as it is not possible to conduct Hall-effect measurements due to the highly resistive layer. Thus a dissolution of the SiN nanomask during the growth of the GaN layer is likely to be responsible for Si incorporation in subsequently grown GaN layers until coealescence.[118]

Figure 4.9 (a) displays the Si-concentration profile in undoped GaN layers with a SiN nanomask as obtained by SIMS plotted against depth. Si incorporation within the GaN layer happens up to around 700 nm thickness, and the Si-concentration falls off from $5\text{x}10^{17}$ cm^{-3} to $2\text{x}10^{17}$ cm^{-3}. The thickness of 700 nm corresponds with the thickness required to re-establish a 2D growth mode after 3D growth induced by the SiN mask.

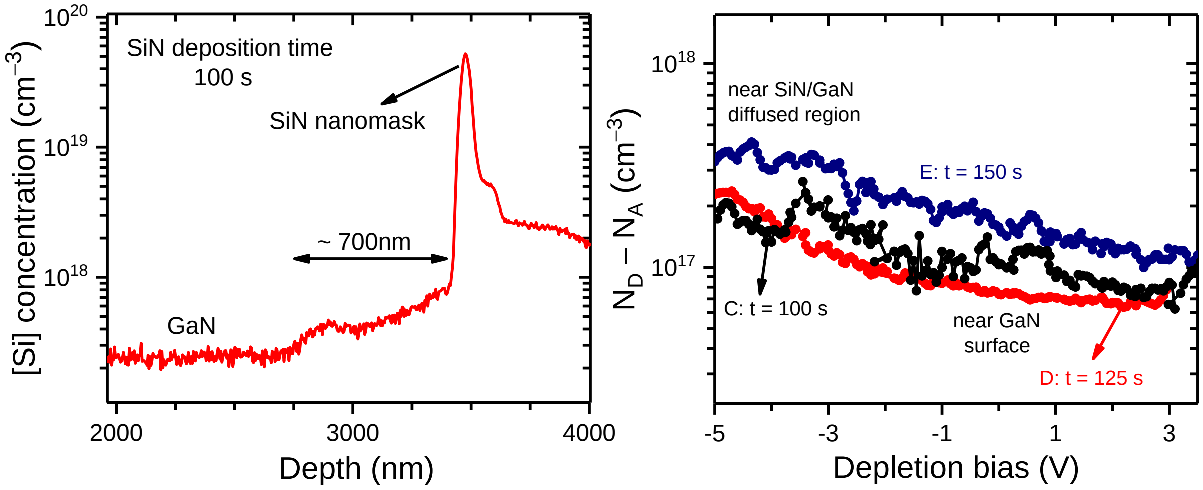

(a) (b)

Figure 4.9: (a) SIMS measurement for depth profile of the Si-concentration for undoped GaN layer with SiN masking layer with deposition time of 100 s; **(b)** Net donor concentration profiles determined by C-V data recorded at 295 K and 1 MHz for the samples C, D, and E.

The net carrier concentration profile for samples C, D and E as obtained from capacitance-voltage measurements using Eq. 2.31, plotted as a function of depletion bias is demonstrated in figure 4.9 (b). Here, the capacitance-voltage measurements are conducted in vertical arrangement between two contacts; an indium dot at the top GaN layer is used while the other at the edge of the sample makes a contact with the Si-doped GaN layer region. Around zero bias, the depletion regime extends only near the GaN surface while at reverse bias of –5 V the depletion regime penetrates into the Si-doped GaN are expected. Again the donor concentration increases from the surface towards the Si diffused region. The obtained values are in the range of (0.5 - 1) x 10^{17} cm^{-3} close to the surface and around $3x10^{17}$ cm^{-3} in the doped region.

4.4 Compensation effects in GaN

In this section semi insulating Fe-doped and extrinsically C-doped GaN series are compared to each other using unintentionally doped GaN as reference. To investigate compensation effects electrical and optical measurement techniques are employed.

4.4.1 Breakdown voltage properties of semi-insulating GaN layers

Compensation effects were analyzed by current-voltage measurements at room temperature on C- and Fe- doped samples using contact arrangements as described in figure 3.6 (a). The current-voltage characteristics of carbon and iron-doped GaN samples are respectively shown in figs. 4.10 (a, b), while figure 4.10 (c) demonstrates the leakage currents at 50 V bias plotted against iron and carbon concentration.

The comparison to the undoped reference sample shows an increasing reduction of free carriers with increasing carbon and iron doping concentrations. Since C-V measurements of the undoped reference sample yields net donor concentrations of $5x10^{16}$ cm^{-3}, acceptor-like compensation behaviour of Fe- and C-impurities is confirmed. For highly doped samples of both series with a doping concentration above 10^{18} cm^{-3}, a decrease in current leakage up to three orders of magnitude is measured. For heavy doping concentrations C-doped samples ($C=4.6x10^{18}$ cm^{-3}) show a resistivity around $9x10^{9}$ Ω-cm whereas Fe-doped sample with ($Fe=5x10^{18}$ cm^{-3}) have resistivities of about $2x10^{7}$ Ω-cm at 50 V bias. Therefore, semi-insulating behaviour for carbon and iron doped samples is concluded.

The net carbon or iron concentration required to compensate the background donor concentration is supposed to be below 10^{17} cm^{-3} as we have determined donor concentrations of $5x10^{16}$ cm^{-3} in the reference sample. Although both the GaN:C and GaN:Fe samples with doping concentrations in the range of ~10^{17} cm^{-3} limit the leakage current as compared to the undoped (reference) sample, a doping level above 10^{18} cm^{-3} significantly reduces leakage currents and increases breakdown voltages further. Most importantly, for all intentionally carbon and iron doped samples the doping concentration exceeds by far the background carrier concentration which is below 10^{17} cm^{-3} in un-doped GaN.

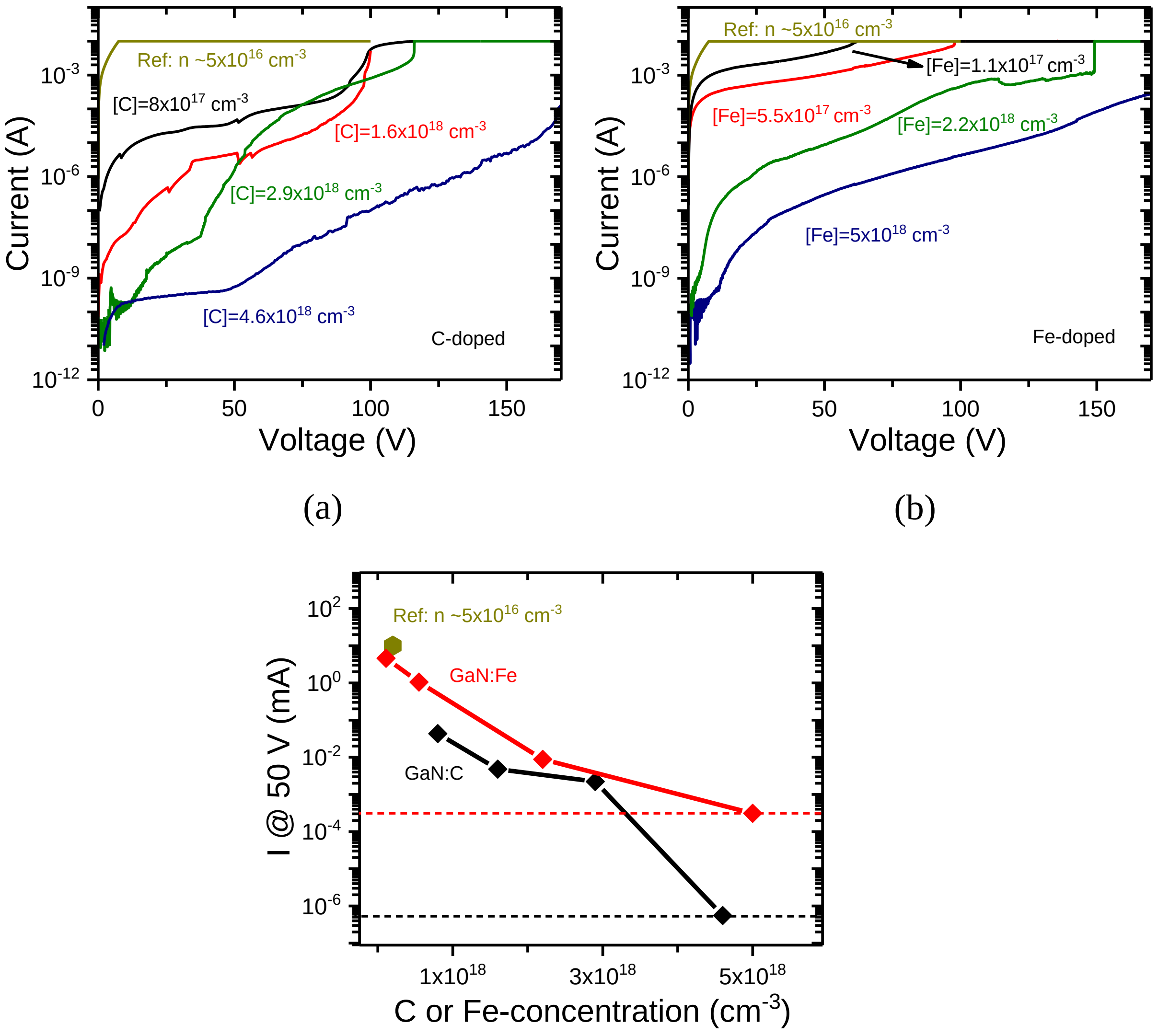

(a) (b)

(c)

Figure 4.10: (a, b) I-V characteristics of C-doped and Fe-doped samples in lateral configuration; **(c)** Leakage currents obtained at 50 V as a function of doping density for C-doped and Fe-doped GaN samples.

Carbon doped samples with C=2.9x10^{18} cm^{-3} exhibit large current leakage above 50 V in comparison with lower C-doped samples, however this behaviour can be attributed to an inferior contact quality. For C-doped samples fig. 4.10 (c) proposes that at 50 V the heavily carbon-doped GaN sample with C=4.6x10^{18} cm^{-3} reduces the leakage current by more than three orders of magnitude as compared to the sample with C=2.9x10^{18} cm^{-3}.[50, 119] Also the buffer breakdown voltage of our test structures increases from around 100 V for intentionally C-doped samples with C $\leq$ 2.9x10^{18} cm^{-3} to 170 V and above for C $\geq$ 4.6x10^{18} cm^{-3}.

On the other side, Fe-doping also substantially enhances breakdown voltages by reducing current leakages from ~10^{-3} A for Fe $\leq$ 5.5x10^{17} cm^{-3} to 3x10^{-7} A for Fe=5x10^{18} cm^{-3} at 50 V as shown in fig. 4.10 (b). However, for comparable doping concentrations (~5x10^{18} cm^{-3}) C-doped GaN sample results in nearly 3 order of magnitude suppression in current leakage than Fe-doped GaN sample at low applied biases around 50 V [Fig. 4.10 (c)]. Obviously, higher breakdown voltages can be achieved by introducing C or Fe acceptor impurities in GaN buffer above the background donor impurity level. Moreover, for a similar concentration C-doping has proved to be more effective than iron doping to reduce lateral leakage currents. This is further discussed in the next section.

4.4.2 Vertical transport properties of semi-insulating GaN

This section focusses on current transport through Fe- and C-doped GaN layers in vertical contact geometry using test samples with a layer structure schematically shown in fig. 3.6 (b). The graphs show the dark currents (I_{dark}) at constant reverse bias voltage measured in dark ambience from room temperature to 400 K both for the C-doped [Fig. 4.11 (a)], and the Fe-doped sample series along with an undoped reference sample [Fig. 4.11 (b)]. In comparison to the undoped reference sample, the dark current at room temperature and reverse bias of 10 V was reduced from 10^{-9} A to 10^{-13} A in C-doped samples whereas in Fe-doped samples dark currents at reverse bias of 2 V were already above 10^{-9} A. Accordingly, specific resistances of 10^{15} Ω-cm for GaN:C and 10^{10} Ω-cm for GaN:Fe were obtained. At 400 K, the values of specific resistances of C-doped GaN were found to decrease by two orders of magnitude while for Fe-doped layers the decrease is below one order of magnitude.

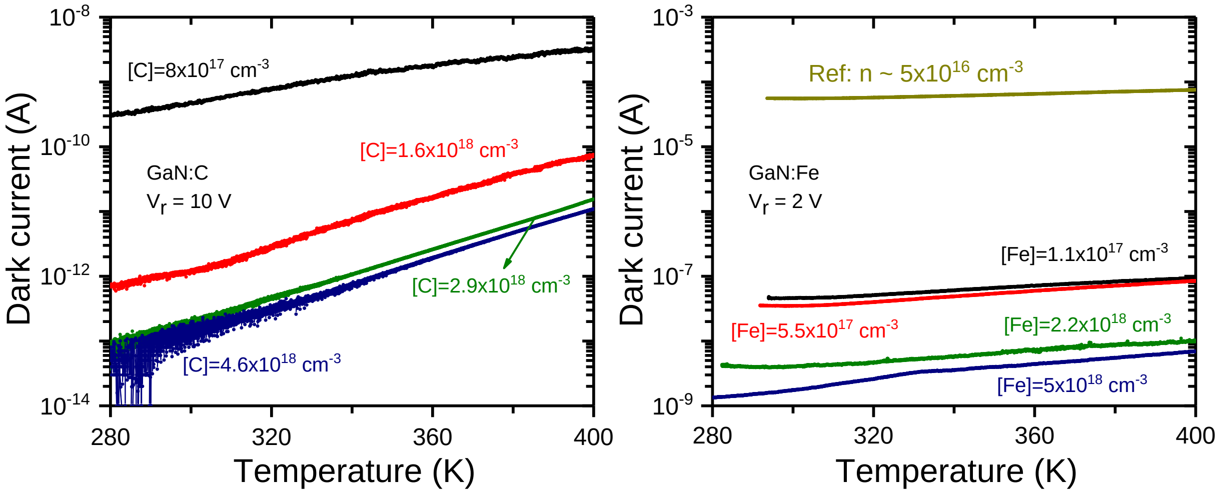

(a) (b)

Figure 4.11: Dark current plotted as a function of temperature for **(a)** C-doped; and **(b)** Fe-doped samples.

From these data activation energies according to an Arrhenius law (ln (I_{dark}) vs. 1000/T) were extracted. Activation energies change from 87 meV to 128 meV with increasing Fe concentration and from 190 meV to 540 meV with increasing C concentration, respectively. By performing temperature dependent dark current measurements using a planar contact configuration with two surface contacts, we find slightly higher activation energies for the GaN:Fe (Fe=5x10^{18} cm^{-3}) and GaN:C (C=4.6x10^{18} cm^{-3}) structures of 0.21 eV and 0.6 eV, respectively. These values are substantially lower than to be expected for a release of electrons from Fe- or C-related trap states. However, dislocations might be responsible for shallower trap states in GaN by providing conducting paths for leakage current.[42, 43] Even though in the employed lateral device geometry, the contribution of threading dislocations to leakage current is expected to be lower than for vertical geometries. Nevertheless due to the large separation of lateral contacts, dark current transport is likely to go vertically through the semi-insulating region and then laterally through the Si-doped GaN layer above the SiN mask. Larger activation energies are therefore unlikely to be found. In recent work[27] activation energy of 0.63 eV are reported in carbon doped GaN-based power HEMTs.

The C-doped samples always show higher values of activation energies than Fe-doped samples which can be explained with the charge contrast present at dislocations as observed in surface potential measurements. SSPM data of GaN:C samples yields an increasing negative charge contrast around dislocations with carbon concentration however in undoped and GaN:Fe samples only weak or no charge contrast is observed at dislocations (see section 4.6). Such negative charge state of dislocations with respect to the carbon-doped GaN matrix can be associated with an energetic barrier for electrons trapped at dislocations providing higher thermal activation energies for leakage currents in GaN:C samples as compared to Fe-doped GaN. For device applications requiring maximum breakdown field strength the C- or Fe-doping concentration in GaN containing dislocations must exceed the background carrier concentration significantly.

4.4.3 Thermal activation energy of GaN with fully Fe-doped layer arrangement

As we see in previous section that Fe-doped GaN samples where only top layer is doped, exhibit activation around 0.21 eV which are lower than the expected value of Fe-acceptor that is around 0.5 eV. In further investigation temperature dependent conductivity spectra were recorded at constant reverse voltage for a GaN buffer structure containing all iron-doped layers arrangement with Fe ~ 3x10^{18} cm^{-3}.

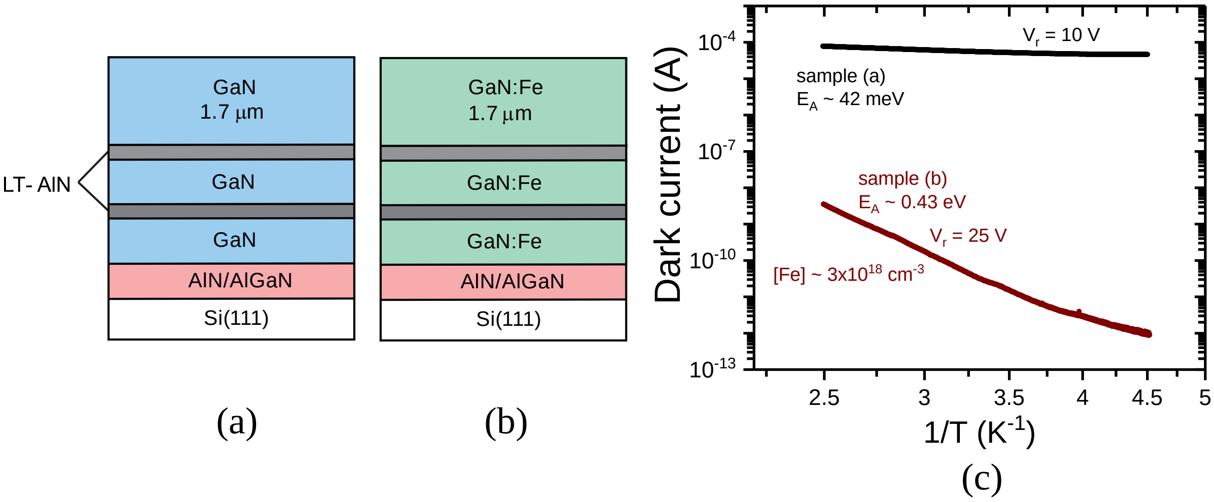

(a) (b) (c)

Figure 4.12: (a, b) Schematic layer arrangement of undoped and Fe-doped sample; **(c)** Arrhenius graphs plotted for dark current measured in planar contact arrangement.

The sample schematics are explained in figs. 4.12 (a, b) while fig. 4.12 (c) exhibits Arrhenius plot for dark current of Fe-doped GaN structure obtained using two surface contacts in comparison with undoped GaN sample. It is observed that the Fe-doped sample (b) which contains all doped layers and no SiN nanomask indicates thermal activation energy E_A around 0.43 eV that is close to the expected value of activation for Fe acceptor state. These results demonstrate that thick Fe-doped layer provides sufficiently high thermal activation while low values as observed in section 4.4.2 can be associated to undoped GaN under top doped layer.

4.4.4 Optical signatures in C- and Fe-doped GaN

The incorporation of carbon and iron in GaN has also been investigated by photoluminescence measurements at 10 K as shown in figs. 4.13 (a) and (b) respectively. The PL spectra of GaN:C samples contain an intense broad yellow luminescence band with a maximum at about 2.22 eV, a weaker blue luminescence band at 2.92 eV along with sharp near-band-edge (NBE) emission at 3.48 eV as presented in fig. 4.13 (a). On the other side, Fe-doped GaN samples show a strong NBE peak similar to C-doped samples, a very weak BL band at 2.84 eV and a highly suppressed YL band at 2.22 eV [Fig. 4.13 (b)].

With increasing acceptor concentration, the absolute PL intensity of the band edge luminescence is drastically reduced in both sample series. The near-band-edge PL spectrum at 10 K of the reference and C-doped samples is originating from two donor bound exciton transitions (DBE_1 at 3.495 eV and DBE_2 at 3.489 eV) along with two free exciton transitions (FX_A at 3.502 eV and FX_B at 3.513 eV)[50, 120] as depicted in fig. 4.13 (c). Monemar et al.

obtained values for the free A- and B-excitonic transitions in PL spectroscopy of relaxed GaN at 3.478 eV and 3.484 eV, respectively.[121] The resulting energy difference for our samples of 24 meV for FX_A indicates compressive strain of 0.87 GPa in agreement with XRD measurements (not shown).

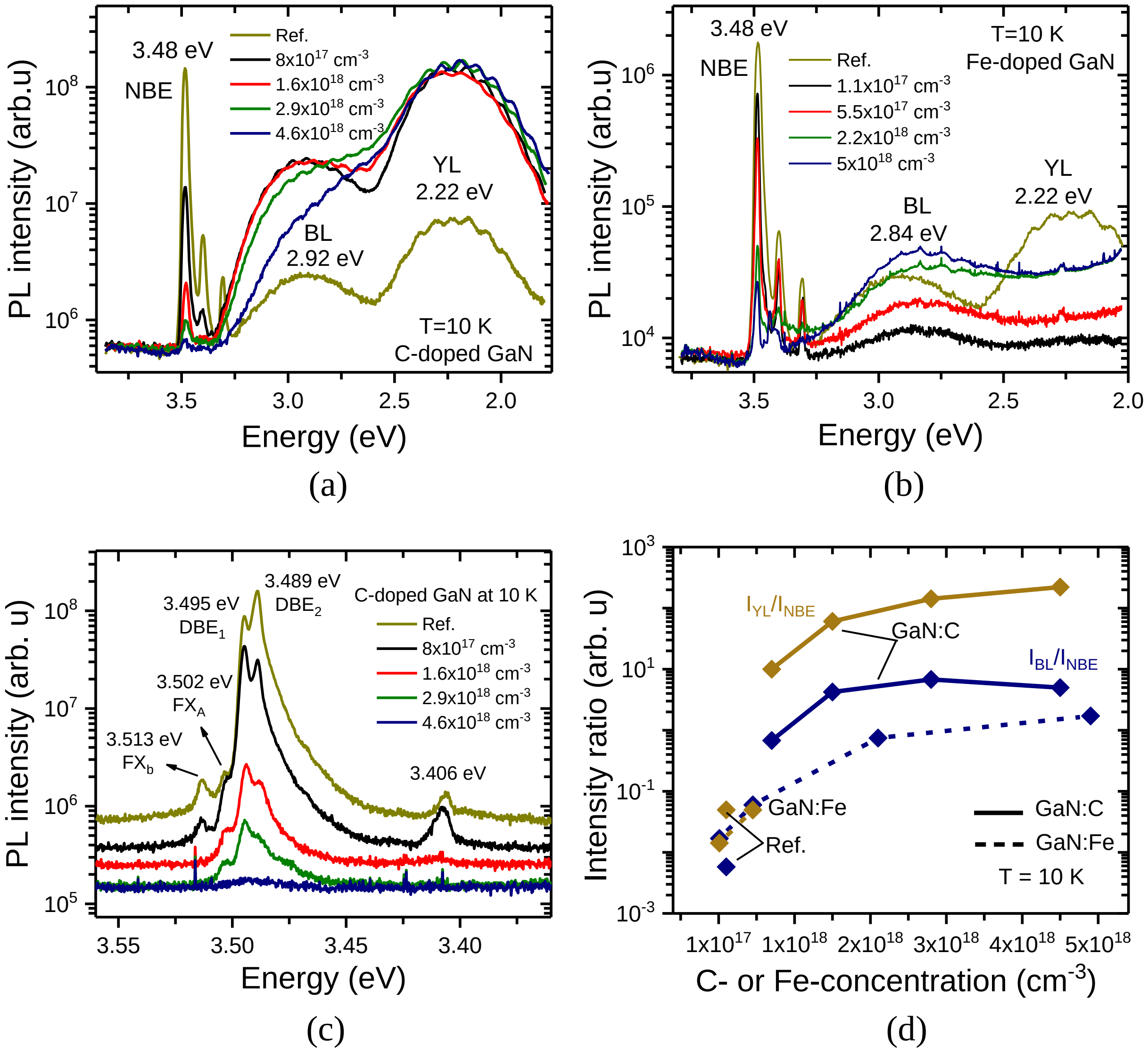

(a) (b)

(c) (d)

Figure 4.13: 10 K PL spectra with absolute intensity of **(a)** C-doped series **(b)** Fe-doped series; **(c)** High resolution 10 K PL spectra of C-doped series; **(d)** Relative intensities of YL and BL bands with respect to NBE.

In C-doped samples the intensity of the YL band increases relative to the NBE emission with increasing carbon concentration. While the absolute intensity of the blue band is highest in moderately C-doped GaN layers with carbon contents around 1.8x10^{18} cm^{-3} the BL intensity tends to decrease with further increasing doping concentration. Similar spectra have been reported[122] for carbon-doped samples grown by molecular beam epitaxy. The relative contribution of the yellow band and blue band emissions is obtained by dividing the respective band intensity by the NBE intensity and is plotted as a function of the carbon concentration in fig. 4.13 (d). A monotonic increase in YL and BL intensities relative to the band-edge emission can be seen.

Carbon incorporated on an N-site (C_N) acts as an initially neutral deep acceptor making a (0/–) charge transition upon capture of an electron with an ionization energy of approximately 0.9 eV.[74] On the other side, the acceptor level of the Fe^{3+}/Fe^{2+} transition lies around E_c – (0.5-0.6) eV within the GaN band gap.[48] According to Armitage et al. and Seager et al. [22, 122], the 2.92 eV BL band is attributed to the transition of C_{Ga} donors to C_N acceptors. However, in figure 4.13 (a), we find a decrease in the absolute BL intensity at high C-doping levels (for C > $1.6x10^{18}$ cm^{-3}) suggesting a decrease of C_{Ga} following Armitage et al.[122] In C and Si co-doping experiments nearly all carbon atoms are incorporated as acceptors (C_N) and no or only low concentrations of carbon related donor states are observed.[50] In addition, the YL band in fig. 4.13 (a), is attributed in literature to a transition between a shallow donor (Si_{Ga} or O_N) and a deep acceptor.[105] It is found that C_N, V_{Ga}, and their complexes C_NO_N or $V_{Ga}O_N$ are major contributor to the yellow luminescence at 2.2 eV in GaN.[73, 106] Thus, the enhancement of the intense yellow and decrease of the weaker BL with carbon doping and the persistence of the YL at all doping levels suggests carbon on nitrogen sites as the dominating deep acceptor state in propane doped GaN.

A broad BL band has been frequently observed in undoped and Si-doped GaN layers which is associated to transitions from conduction band or shallow donor to a relatively deep acceptor.[105] In GaN:Fe samples, the relative intensity of the BL band is observed to increase only marginally with Fe-concentration, while in heavily Fe-doped samples the intensity of the YL band is prominently suppressed by Fe doping. This reduction might be attributed to a reduction in Ga vacancies V_{Ga} and and/or defect complexes composed of V_{Ga} and O, when Fe exceeded the background donor concentration.[123] Such behaviour is reported in iron doped GaN/AlGaN[124] heterostructures and GaN layers.[125] Low temperature PL studies of Fe-doped GaN substrates demonstrated the compensation of Si and O shallow donors, and an incorporation of Ga substitutional Fe^{3+} compensating centers.[126] Usually deep iron acceptors Fe^{3+} (in the neutral state) and Fe^{2+} (in the excited state) act as nonradiative recombination channels. Thus a reduction in the intensity of the excitonic emission and the YL band with increasing iron concentration is correlated to such non-radiative recombination centers in Fe-doped GaN.[75] Due to a high Fe content, radiative donor-acceptor pair transitions are suppressed by prevailing non-radiative recombination channels.

4.5 Fermi-level shift in semi-insulating GaN layers

In this section the Fermi-level shift in carbon and iron doped GaN layers in comparison with undoped and conductive (n- and p-type) GaN layers is investigated by performing electric force microscopy measurement. The technique leads to an indirect measurement of work function or contact potential of the sample which is associated to Fermi-level position within the band gap. The effect of doping contents and dopant type on the contact potential behaviour of GaN surfaces is discussed in detail.

4.5.1 Contact potential difference comparison of semi-insulating GaN layers

Bias dependent electrostatic force microscopy images in phase mode are obtained on C- and Fe-doped as grown samples with the aim to determine the contact potential differences in comparison to n- and p-type GaN layers. A series of 3x3 µm^2 EFM images for un-etched GaN:C ([C] = 4.6x10^{18} cm^{-3}) at DC biases of 0 V, −1 V, −2 V and −4 V, respectively, are presented in figs. 4.14 (a-d).

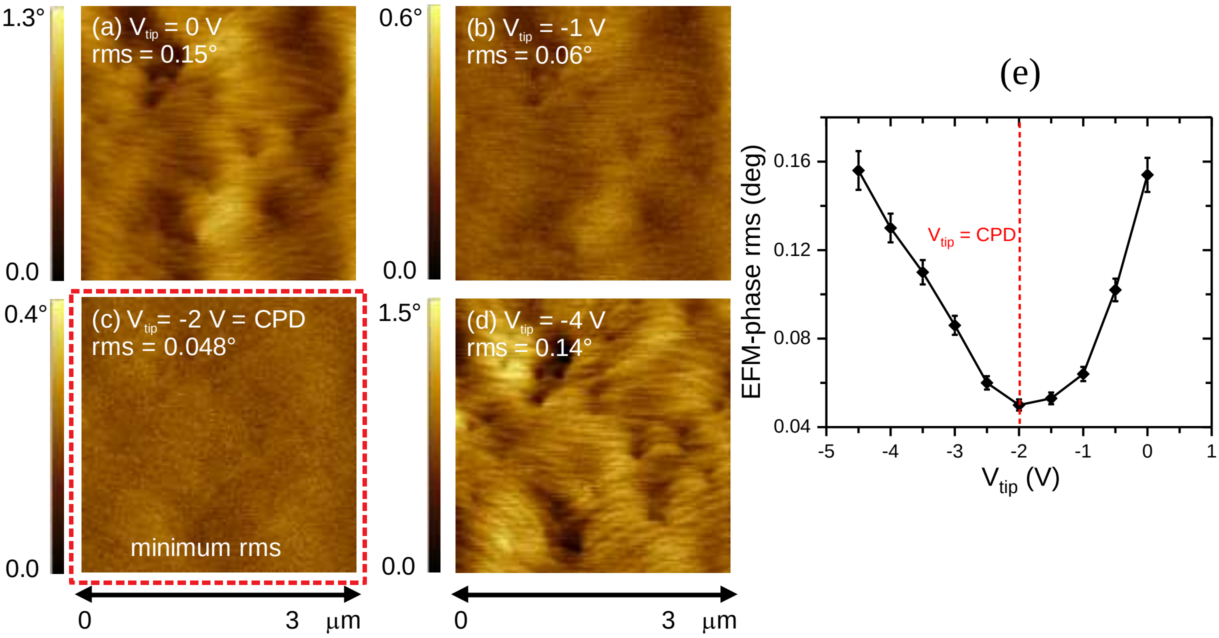

Figure 4.14: (a-d) 3x3 µm^2 EFM phase images of un-etched GaN:C (C= 4.6x10^{18} cm^{-3}) at DC biases of 0 V, −1 V, −2 V and −4 V; **(e)** Variation of phase as a function of tip voltage V_{tip}.

When the DC bias applied to the cantilever tip (V_{tip}) is changed, the roughness contrast in EFM changes due to variation in the induced surface charges. As indicated in fig. 4.14 (c), the lowest roughness contrast is seen in EFM-phase image at a tip bias around –2 V, however the signal is not completely cancelled (rms is not zero) due to first term of Eq. 3.3 which leaves a weak residual image. Fig. 4.14 (e) illustrates that the rms-roughness values obtained from EFM phase-images plotted against the tip bias construct a parabolic curve following the theoretical V^2 dependence of Eq. 3.3. After fitting a parabola the contact potential difference between the metallic tip and the GaN:C layer is determined from the minimum of the curve yielding –1.96±0.04 V at a C-concentration of 4.6x10^{18} cm^{-3}.

A similar bias series of 3x3 μm^2 EFM images obtained for an Fe-doped GaN sample with [Fe] = 5x10^{18} cm^{-3} is depicted in figure 4.15, where figs. (a-f) are EFM phase contrasts obtained at DC biases of –1 V, 0 V, +1 V, +1.5 V, +3V, and +5 V respectively. It is noteworthy that the minimum contrast for Fe-doped GaN is observed at +1.5 V which indicates a positive contact potential difference while for C-doped GaN a minimum contrast at negative bias is suggesting a negative value for the local contact potential difference.

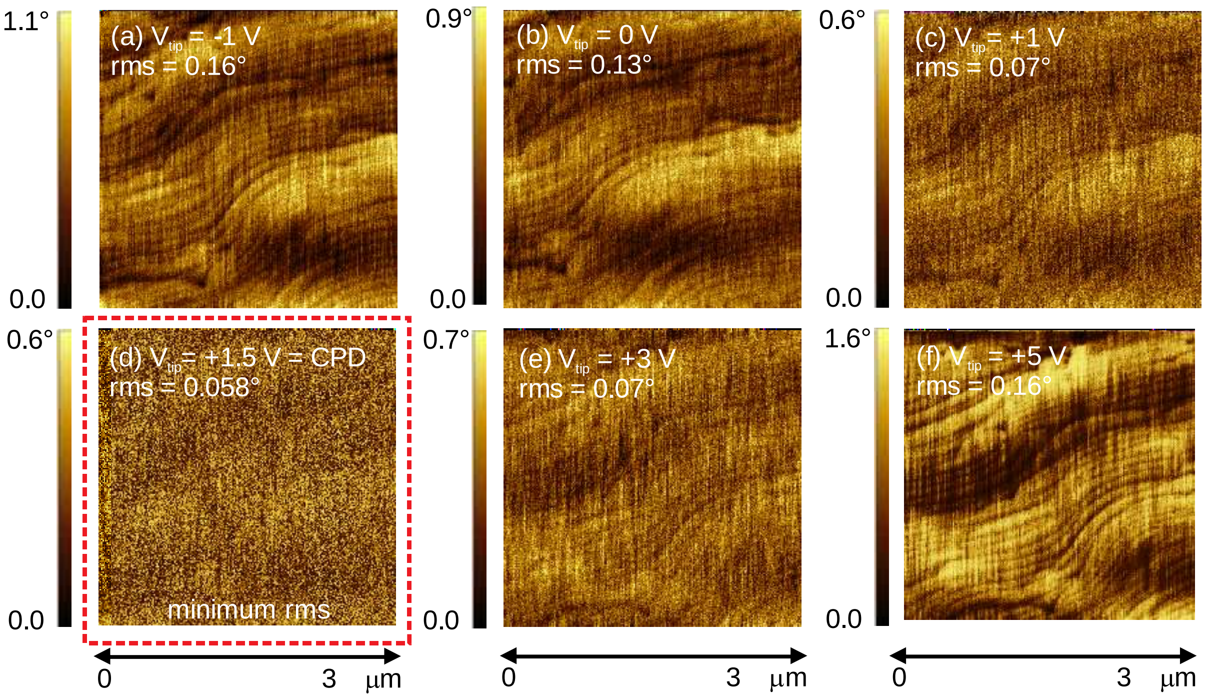

Figure 4.15: (a-f) EFM phase images (3x3 μm^2) of un-etched GaN:Fe ([Fe]= 5x10^{18} cm^{-3}) at DC biases of –1 V, 0 V, +1 V, +1.5 V, +3 V and +5 V respectively.

A series of parabolic curves for C-doped samples is presented in figure 4.16 (a) where the carbon concentration was increased from undoped material ([C] ≤ $2.0\text{x}10^{17}\text{cm}^{-3}$) to [C] = $4.6\text{x}10^{18}$ cm^{-3} for the highest C-doped GaN:C sample. The contact potential difference of the reference sample is around 0.98±0.04 V. As can be seen in figure 4.16 (a), the minima of the parabolas shift from +0.98±0.04 V to −1.96±0.04 V indicating that sign and magnitude of the contact potentials are depending on carbon concentration. In contrast the contact potential of Fe-doped layers is always positive and increases from +0.93 ± 0.04 V to +1.95 ± 0.05 V [Fig. 4.16 (b)]. This suggests that the electrostatic force measured by EFM is not only depending on dopant type but also on doping concentrations. Similar bias dependent EFM measurements were done for a series of n-type (Ge-, Si-doped) and p-type (Mg-doped) GaN layers with different doping levels.

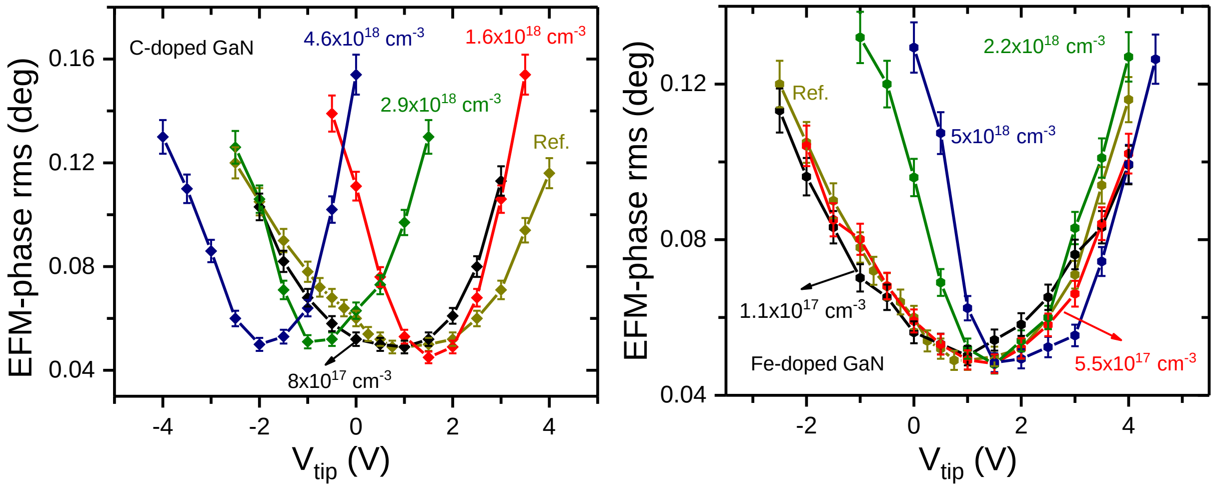

(a) (b)

Figure 4.16: (a, b) Variation of minima or contact potential difference as a function of carbon and iron concentration.

The EFM curves obtained from n-, p-type and semi-insulating GaN layers are compared in figure 4.17. It is well known that the contact potential difference depends on electrical properties of conductive probe and the sample. Furthermore, the measured electrostatic force may also be influenced by substrate and interlayers to some extent. Typically the metal probe and sample surface can be modelled as a resistor and a parallel plate capacitor. Due to the difference in work function between the tip and the sample surface, an attractive or repulsive electrostatic force is exerted on the EFM probe hence changing the resonant frequency. This force has contributions from capacitive forces by the tip-sample capacitor and Coulomb forces due to induced surface charges.

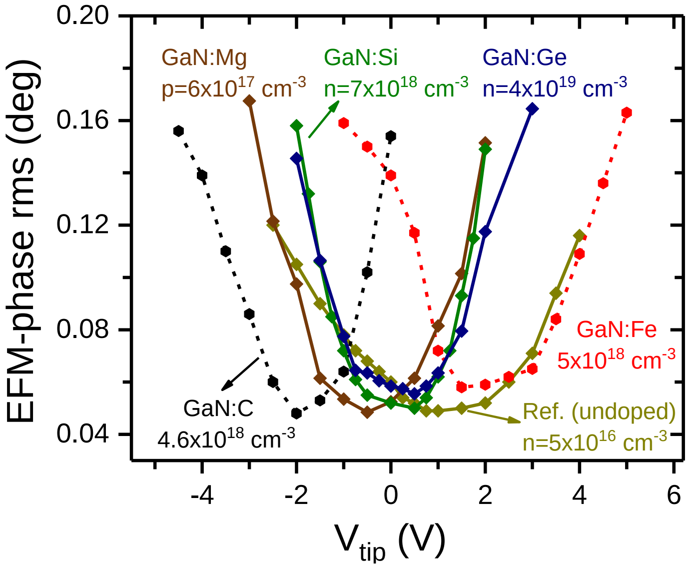

Figure 4.17: Comparison of contact potentials of semi-insulating and conductive GaN layers.

It can be noted from fig. 4.17 that semi-insulating (C- and Fe-doped) GaN samples show higher rms values compared to conductive (n- and p-type) GaN layers layers in low applied bias regime near zero tip voltage. Considering constant Coulomb forces due to surface charges, higher rms values in the case of semi-insulating samples are attributed to stronger changes of the capacitive effects. These introduce a large shift in the cantilever's frequency hence a large roughness contrast will be observed in EFM amplitude and phase-images even when no bias is applied to the tip. However for conductive surfaces the cantilever tip is only marginally influence in amplitude and phase detection since changes of the capacitive effects are small.

The contact potential in dependence of dopant species and doping level is plotted in fig. 4.18 (a). Heavily doped, n-type GaN layers exhibit low values of $V_{contact}$ between 0.5 ± 0.05 V to 0.38 ± 0.05 V for Si-doped ($n \approx 6x10^{18}$ - $2x10^{19}$ cm^{-3}) and 0.6 ± 0.05 V to 0.44 ± 0.03 for Ge-doped ($n \approx 7x10^{18}$ - $1x10^{20}$ cm^{-3}) samples, respectively. For comparable doping concentration of Ge- and Si-, these values are within the range of error. In previous reports, [35, 56, 98, 127] similar values of surface potential have been determined the for undoped, and Si-doped GaN samples. In contrast, Mg-doped samples with hole concentrations of 4 - 6 x 10^{17} cm^{-3} exhibit $V_{contact}$ between –0.37 V and –0.48 V. These values agree reasonably well with values for p-type GaN studied by surface photovoltage variation (SPV)[36] and by Kelvin probe force microscopy (KPFM).[35] Table 4.3 compares our results for n- and p-type GaN to the values reported in literature.

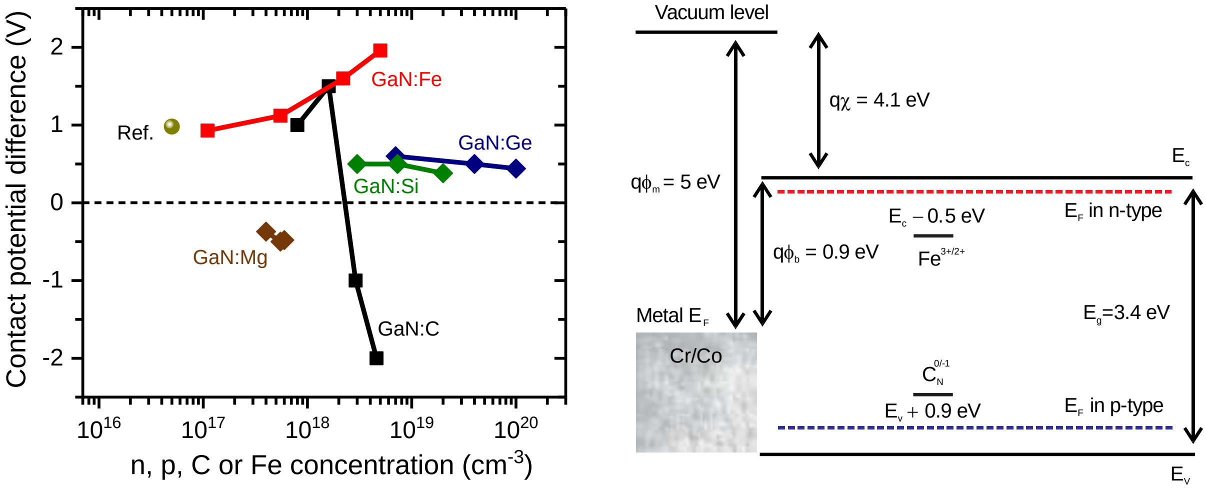

(a) (b)

Figure 4.18: (a) Contact potential vs. electron, hole, Fe, and C concentration for n-type doping (Si, Ge), p-type doping (Mg), Fe-doped and C-doped samples respectively; **(b)** Energy band diagram of GaN and cobalt with Fermi level positions according to n-and p-type conductivity and energetic positions of Fe- and C- related trap states.

The contact potential dependence on the conductivity type can be well described by considering the band diagrams of GaN and cobalt with reference to the vacuum energy level as shown in fig. 4.18 (b). In order to understand the different behaviour of the contact potentials with increasing doping level one first has to look at the Fermi level. In fig. 4.18 (b), the band diagrams of GaN and cobalt are schematically shown relative to each other with the vacuum energy level taken as 0 eV. In addition, the positions of the Fermi-levels in n- and p-type materials as well as the energies of Fe- and C-related trap states ($C_N^{0/-1}$ and $Fe^{+3/+2}$) are indicated. [73, 48] The definite polarity of heavily doped GaN:Ge, GaN:Si, and GaN:Mg layers allows us to assign positive contact potentials to Fermi-levels above the midgap position and negative contact potentials to Fermi-levels below the midgap position.

According to EFM results of semi-insulating series, the degree of compensation by carbon or iron acceptors depends on the acceptor concentration. For low or nominal acceptor concentration ~ 10^{17} cm^{-3}, only shallow donors near the conduction band are compensated while with an increase in acceptor concentration deeper donors get also compensated shifting the Fermi level position towards midgap.[52] Therefore the compensation exhibits a step like behaviour for different acceptor concentrations, and the shift in Fermi level position after compensation is determined by the total acceptor concentration and the energy states of donors.

Table 4.3: Contact potential difference ($V_{contact}$) for n- and p-type GaN layers

Reference	**GaN type**	**Method**	**Carrier conc. (cm^{-3})**	**$V_{contact}$ (eV)**
Simpkins et al.[98]	n-type	SKPM	$5x10^{19}$	0.1 - 0.2
Köhler et al.[56]	GaN:Si	depletion approximation	$6x10^{17}$	1.5
Köhler et al.[56]	GaN:Si	depletion approximation	$2.3x10^{19}$	0.2
Chevtchenko et al.[127]	Undoped	SKPM	$\sim 10^{16}$	0.7 ± 0.1
Barbet et al.[35]	GaN:Si	KPFM	$2x10^{18}$	0.28 ± 0.04
Barbet et al.[35]	GaN:Si	KPFM	$1x10^{19}$	0.13 ± 0.12
Barbet et al.[35]	GaN:Mg	KPFM	$7x10^{16}$	– 0.52 ± 0.32
Barbet et al.[35]	GaN:Mg	KPFM	$8x10^{16}$	– 0.05 ± 0.16
Simpkins et al. [36]	GaN:Mg	SPV	$5x10^{17}$	– 0.36
This work	Undoped	EFM	$5x10^{16}$	0.98
This work	GaN:Si	EFM	$(0.3-2)x10^{19}$	0.5 - 0.4
This work	GaN:Ge	EFM	$7x10^{18}$ - $1x10^{20}$	0.6 - 0.44
This work	GaN:Mg	EFM	$(4 - 6)x10^{17}$	– 0.37 - – 0.48

In our semi-insulating series (C- and Fe-doped), the Fermi level must shift from a position near the conduction band minimum for the undoped, n-type GaN material towards the midgap position with an increasing compensation of free electrons. In case of Fe doping, the Fermi level remains above midgap position as the respective acceptor states are energetically above midgap position at $E_c - 0.5$ eV.[48] Carbon-related acceptor states are, however, positioned below midgap at around 0.9 eV ($E_c - 2.5$ eV) above the valence band maximum in GaN.[73, 74] As a consequence, the Fermi-level will cross the midgap position to the energetic position of $C_N^{0/-1}$ if the material becomes semi-insulating.

The position of Fermi level at the corresponding semiconductor surface with respect to Co/Cr tip is provided by the difference between metal work function and χ_{GaN} , however the band bending introduced by surface states or impurities cannot be neglected. In order to approximate the net surface band bending, the first two terms on the right hand side of Eq. 3.4 are assumed to be constant for all samples. For the metal work function ϕ_m, we used 5.0 eV for cobalt being the outer coating material of the probe tip.[128] The electron affinity of GaN χ_{GaN} was reported to 3.5 eV for a cleaned surface and 4.1 eV for an oxidized GaN surface.[129] In these calculations the latter value results in a Schottky barrier height $\phi_b = |\phi_m - \chi_{GaN}| = 0.9$ eV. The net band bending is obtained by $\Delta\phi = \phi_b - e \cdot V_{contact} - \Delta E_{fn}$.[60] For Si- and Ge-doped samples an average contact potential value of $V_{contact} = +0.5$ V is used. A calculation of the Fermi level position yields $E_F\text{-}E_c \approx (-20/+130)$ meV for doping levels between 5x10^{18} cm^{-3} to 2x10^{19} cm^{-3}. For n-doped GaN with $n > 10^{19}$ cm^{-3} an average upward surface band bending of $\Delta\phi = 0.4\pm0.05$ eV is obtained. For p-type GaN we assumed $\Delta E_{fn} \approx 3.24$ eV and $V_{contact} = -0.35$ V resulting in $\Delta\phi = -1.99$ eV. These values are in the range of band bending as determined by Cook et al.[130] i.e. + 0.3 eV for GaN:Si and −1.3 eV for GaN:Mg. Deviations in the absolute values are within the uncertainty of the electron affinity in GaN.[127]

The surface band bending for highly resistive samples can be approximated to +0.36 eV for the highest doped GaN:C layer and −1.56 eV for GaN:Fe. In the first case, the calculated surface band bending is in the range for GaN:Ge and GaN:Si samples while in the latter case, the surface band bending is slightly lower than in GaN:Mg samples. Generally we expect upward band bending in Fe-doped samples and downward band bending in C-doped samples. In semi-insulating samples we can, however, not exclude an additional voltage drop across the semi-insulating GaN region leading to a bias offset in the measurement. Determination of such a bias offset is difficult as it would require knowledge about specific geometries such as the probe tip shape and diameter. Therefore, the values for surface band bending of semi-insulating layers are not discussed. The change of the contact potential polarity with increasing C concentration still holds, however.

4.5.2 Contact potential of GaN:C cap layers on AlInN FETs

In order to investigate the compensation effect of carbon on the surface properties of device structures, bias dependent electric force microscopy measurements were also conducted on two GaN:C/GaN/AlN/AlInN heterostructures. Here thin GaN:C cap layers with [C] ~ 3 x10^{18} cm^{-3} were grown on AlInN barrier layers while the nominal thicknesses of top layer were ~10 nm and ~25 nm, respectively. For comparison imaging was also performed on a reference sample with undoped GaN cap layer. The details of these heterostructures are provided in section 5.2 of chapter 5. Figs. 4.19 (a-d) show 3x3 μm^2 EFM images obtained for a 25 nm thick C-doped GaN cap layer sample at DC biases of +2 V, 0 V, –1 V and –4 V respectively. Fig. 4.19 (e) plots the rms values obtained from corresponding EFM images against applied tip bias. By fitting the data points, the values of contact potentials are estimated around –0.92 and –1.08 V for samples with top layer C doped, and +0.5 V for reference sample with undoped GaN cap layer. Even for thin GaN:C layers, the position of the Fermi level shifts below mid-gap confirming the compensation effect introduced by carbon atoms.

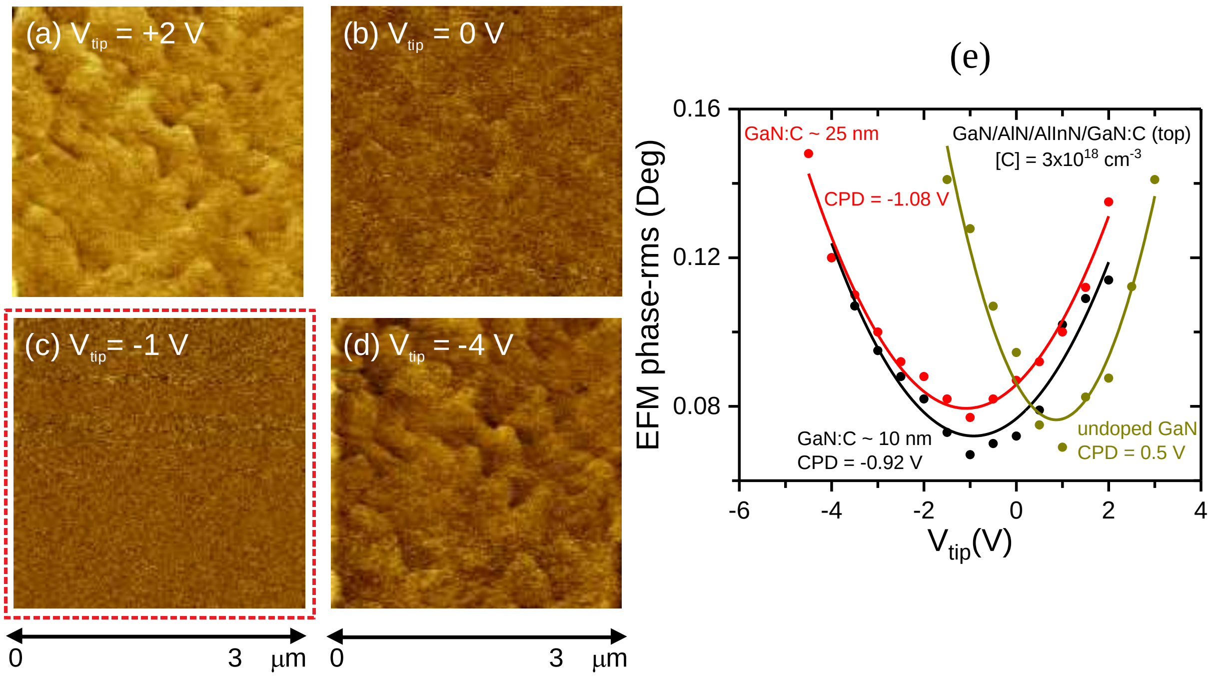

Figure 4.19: (a-d) 3x3 μm^2 EFM-phase images of a GaN/AlN/AlInN heterostructure with 25 nm GaN:C cap layer at tip biases of +2 V, 0 V, –1 V and –4 V respectively; **(e)** EFM parabolic curves of GaN/AlN/AlInN FETs with undoped GaN and GaN:C cap layers.

4.6 Local electronic properties of GaN layers

In this section, electronic properties around dislocations at the surface of undoped, C-doped and Fe-doped GaN layers are investigated by performing scanning surface potential microscopy. Moreover the potential contrast around dislocations in semi-insulating GaN is compared with conductive GaN samples. The effect of doping contents and dopant type is studied by comparing the charge state of dislocations with respect to the surrounding region.

4.6.1 Potential contrast around dislocations in C-doped GaN layers

AFM topography and corresponding surface potential mapping profiles of GaN layers are simultaneously recorded on etched sample surfaces in tapping mode with a SSPM setup. In order to exclude any change of the charge state of the sample upon etching samples are investigated before and after etching. The surface morphologies change upon etching as intended, however, without etching the SSPM data could not be obtained as clear as for etched samples.

Figure 4.20 (a) and (b) respectively, present the topography and potential profiles of an undoped GaN sample acquired on the surface before etching treatment. Line scans in figure 4.20 (c) indicated by the red and green curves are obtained from height and potential data of respective images [4.20 (a, b)]. According to Eq. 3.5, a negative charge state of these regions relative to the background potential on the flat surface regions is concluded from the positive value of the SSPM signal around pits. The SSPM contrast for the un-etched GaN sample exhibits broadened potential peaks which can be only roughly correlated with dislocations.

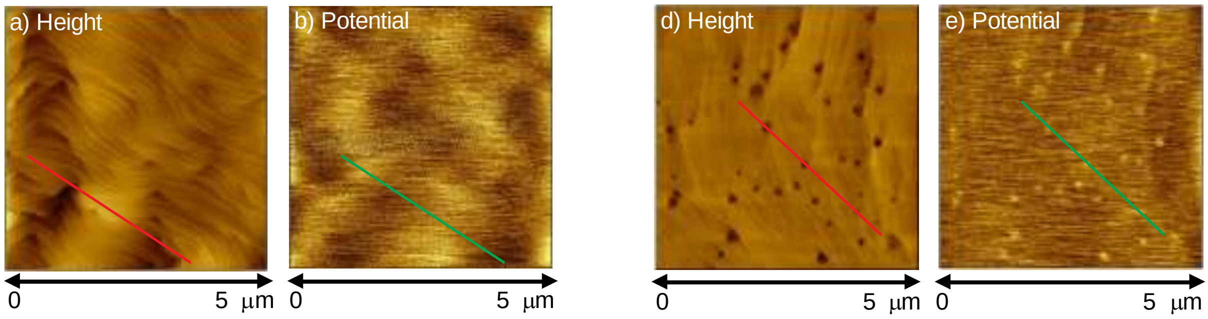

(c) Line scan

(f) Line scan

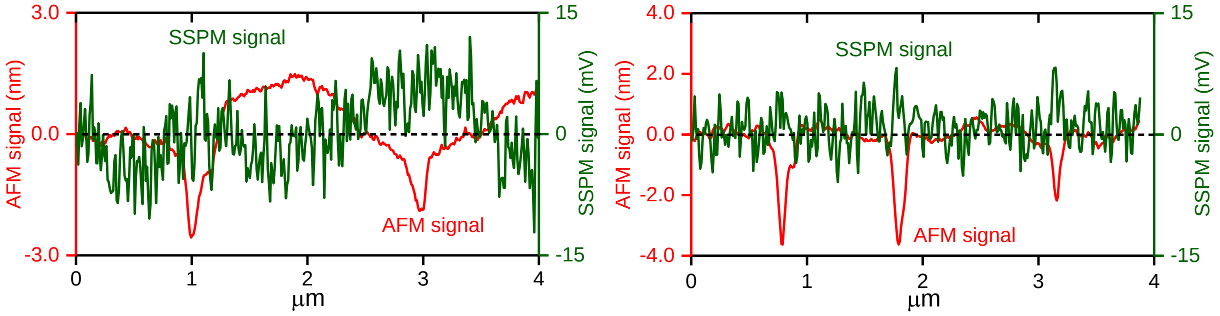

Figure 4.20: Surface images (5x5 µm^2) of undoped GaN surfaces: **(a, b)** height profile and corresponding SSPM image of an un-etched surface; **(c)** extracted line scan from (a) and (b); **(d, e)** height profile and corresponding SSPM image of an etched surface; **(f)** extracted line scans from (d) and (e) across dislocations.

The SSPM profiles obtained for unetched surface of C-doped GaN layers reveal negatively charged dislocations (not shown) but with poor resolution. The surface morphologies changed upon etching resulting in high resolution AFM images for topographic measurements as discussed in section 4.3.[116] Moreover the charge contrast of dislocations from the potential profiles of etched surfaces are agreeably correlated with etched pits observed in height images. Therefore, only etched GaN samples were further used for detailed SSPM investigations of these dislocation pits.

The surface potential mapping of an etched sample surface of undoped GaN with a perfect match of bright and dark spots in height along with the corresponding potential image is presented in figs. 4.20 (d, e). Line scans in fig. 4.20 (f), indicated by red and green lines in the respective images 4.20 (d, e), are extracted such that dislocations are traversed. Dislocation related pits are clearly visible in the surface morphology image and correspond to bright regions in the surface potential image. All pits show no significant change in the SSPM signal with respect to the background signal. Sign and amplitude of the potential signal is similar to that of unetched samples. The amplitude of the SSPM signal in the vicinity of dislocations is found to be very low (< 10 mV) close to the background noise level. Moreover, Si and C co-doped GaN samples with n-type conductivity, as determined by Hall-effect measurements,[50] also exhibit neutral or weakly charged dislocations (not shown). In previous work Krtschil et al. also reported neutral dislocations in un-doped GaN[116] and n-GaN[34] films.

Figs. 4.21 (a-c) present all types of dislocations in one image and show height and potential images as well as extracted line scans of a heavily C-doped GaN sample ($[C] = 4.6\text{x}10^{18}\ \text{cm}^{-3}$). From the positive value of the SSPM signal at dislocations, a negative charge state relative to the background potential on the flat surface regions is concluded. It is noteworthy that this difference of the potential signal is depending on the carbon concentration. Even for lightly carbon doped samples surface potential maxima at the core of dislocations are distinguishable from background noise with a potential signal of 15 meV while heavily carbon doped samples exhibit saturated surface potential signals of around 27 meV. All types of pits are negatively charged, however, the surface potential contrast varies for different dislocation types. A summary of the approximate surface potential contrast and other investigations for C-doped samples is presented in table 4.4.

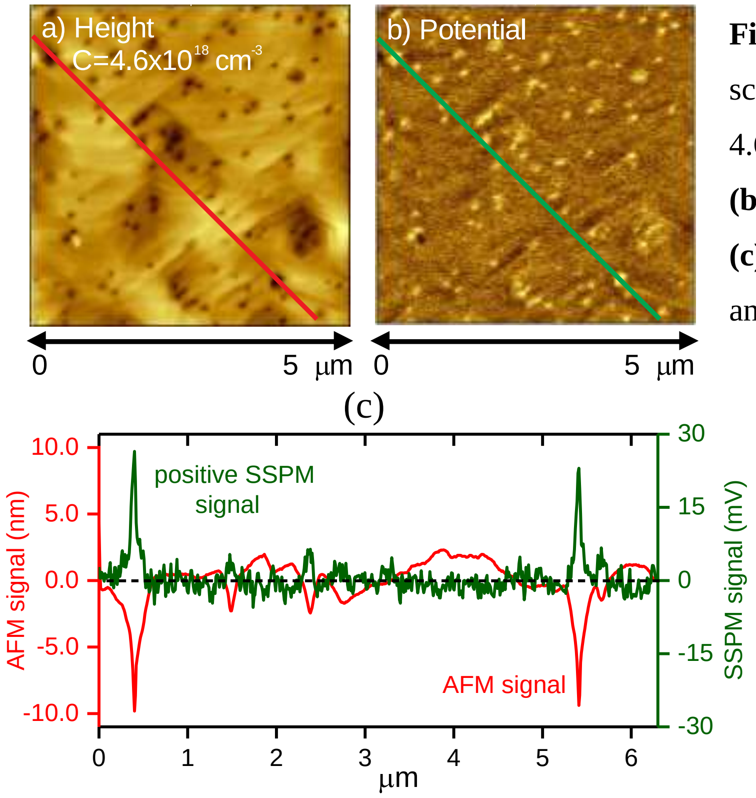

Figure 4.21: 5x5 µm^2 surface scans of C-doped GaN with [C]= 4.6x10^{18} cm^{-3}, **(a)** height image; **(b)** respective SSPM image; and **(c)** extracted line scans from (a) and (b) across dislocations.

Table 4.4: Samples with different intentional carbon concentrations by propane doping as determined by SIMS, FWHM and dislocation density as determined from XRD, EPD as determined from AFM as well as buffer leakage current at 50 V for a contact distance of 20 µm, surface potential as determined by SSPM measurements.

[C] (cm^{-3})	≤2.0x10^{17} (uid)	8.0x10^{17}	1.6x10^{18}	2.9x10^{18}	4.6x10^{18}	6.7x10^{18}
FWHM [0002] (deg)	0.086	0.095	0.089	0.092	0.098	0.088
FWHM $[10\bar{1}0]$ (deg)	0.128	0.136	0.130	0.126	0.14	0.10
XRD ρ_s (10^8 cm^{-2})	1.9	2.4	2.1	2.2	2.5	2
XRD ρ_e (10^9 cm^{-2})	1.1	1.3	1.2	1.1	1.4	0.7
AFM EPD (10^8 cm^{-2})	2±0.12	2.1±0.23	2.0±0.13	2.2±0.20	2.5±0.30	2.2±0.13
SSPM peak height (mV)	<10	15±1.5	20±1.5	24±2.6	26±1.4	27±4
I @ 50 V (mA)	> 100	4.5x10^{-2}	5.3x10^{-3}	1.4x10^{-3}	3.3x10^{-7}	9.7x10^{-7}

The SSPM peak height is estimated using an average value of 5 peaks from a 5x5 μm^2 image. Bright regions in the potential image are designated to a higher work function indicating the Fermi level being closer to the valence band.[98] The SSPM signal is taken relative to the background surface potential defined as zero. From SSPM measurements it is concluded that carbon-doping in GaN enhances the charge state contrast of dislocations from the neutral/weakly charged character in un-doped and n-type GaN to a predominantly negatively charged character for carbon doped GaN layers. With increasing carbon concentration the signal increases until saturation around 27 meV as presented in figure 4.22.

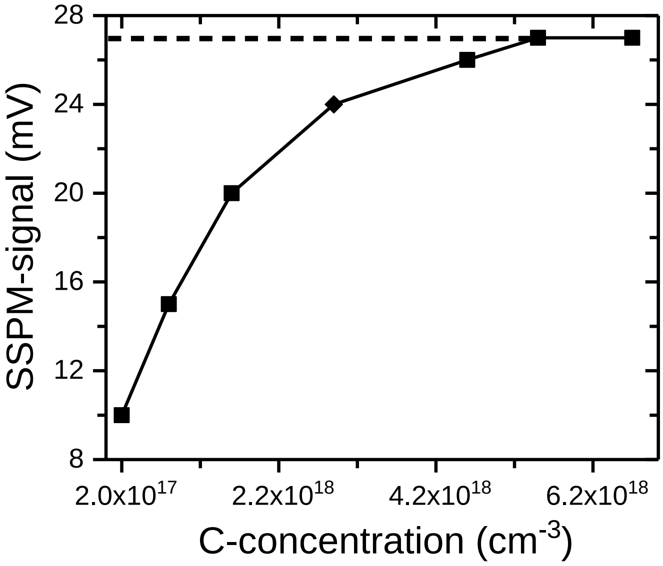

Figure 4.22: The SSPM signal strength of the samples plotted as a function of C-concentration with saturation around 27 meV.

To discuss the observed charge contrast of dislocations in GaN:C we have to consider two possible effects. Firstly, the dislocation core itself or their vicinity may be electrically charged depending on the Fermi-level position[131] or carbon-related acceptors may be accumulated around dislocations changing its electrical character.[34] Secondly, the background surface potential is reduced by a Fermi level shift towards the valence band due to carbon compensation effects.[131, 132] In undoped and lightly carbon doped layers, the Fermi-level position is supposed to be pinned near the conduction band minimum. With increase in carbon concentration the position of Fermi-level shifts across the band gap and moves towards valence band where it is pinned to the position at 0.9 eV above the valence band maximum (VBM).[18, 73] Accordingly, the charge contrasts are depending on the position of the Fermi level. From the EFM measurements on C-doped samples we expect a local increase in the work function at the vicinity of dislocations which is consistent with the large potential variations around dislocations. Uren et al. also reported a negative acceptor charge due to a potential gradient in C-doped GaN/AlGaN structures.[133] This negative potential contrast around dislocations in GaN:C samples might be associated with an energetic barrier for electrons trapped at dislocations.

4.6.2 Potential contrast around dislocations in Fe-doped GaN layers

The AFM height and surface potential maps (5x5 μm^2) of etched Fe-doped GaN surface with Fe = 2.2x10^{18} cm^{-3} along with a corresponding line section through dislocations are respectively shown in figs. 4.23 (a-c), whereas figs. (d, e) exhibit height and potential images of a Fe-doped sample having Fe = 5x10^{18} cm^{-3}. An iron doped GaN sample with intermediate Fe-concentration shows only weakly charged pits with SSPM signal <10 mV while in a GaN:Fe sample with Fe = 5x10^{18} cm^{-3} no charge contrast is associated with dislocations.

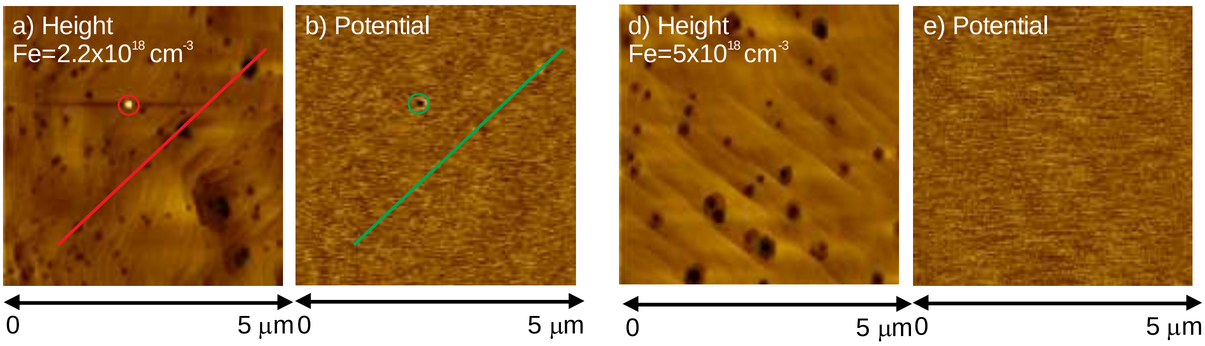

(c) Line scan

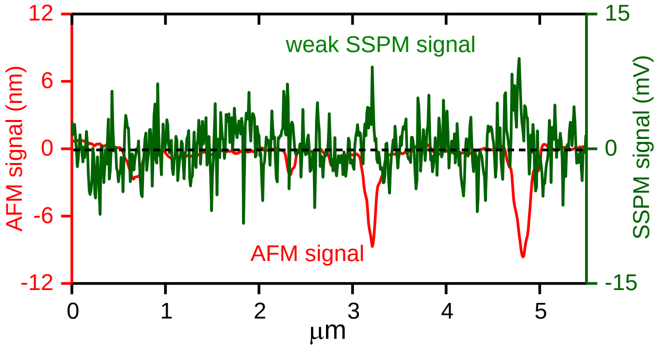

Figure 4.23: Surface images of Fe-doped GaN Fe= 2.2x10^{18} cm^{-3} GaN after wet-etching: **(a)** 5x5 μm^2 height profile; **(b)** corresponding SSPM image; **(c)** extracted line scan from (a) and (b) across dislocations. Surface scans (5x5 μm^2) of Fe-doped GaN Fe= 5x10^{18} cm^{-3}: **(d)** height image; **(e)** corresponding SSPM image.

As discussed in the section 4.5.1 of this thesis, iron doping in GaN is believed to cause Fermi-level pinning near $E_c - 0.5$ eV.[48] With increasing Fe-concentration the Fermi-level moves from near the CBM to the Fe^{3+}/Fe^{2+} charge transfer level, when compensating residual donors. Therefore consistent potential contrast of dislocations independent of doping level observed in GaN:Fe layers is related to Fermi-level position. On the other side in Fe-doped GaN layers, during wet etching process a decoration of Fe defects around the dislocations has been found.[134] Thus there is also a probability that iron acceptors (Fe^{3+} or Fe^{2+}) decorated around dislocations might compensate the weak negative charge of the threading dislocation core as seen in undoped GaN.[135]

4.6.3 Potential contrast around dislocations in conductive GaN layers

The surface topography, potential and their respective line scans through dislocations for a Si-doped ($n = 8x10^{18}$ cm^{-3}) GaN sample are shown in figs. 4.24 (a-c), respectively, whereas figs. 4.24 (d-f) demonstrate the height and potential images along with corresponding line scans traversed through dislocations for Mg-doped ($p = 6x10^{17}$ cm^{-3}) GaN sample.

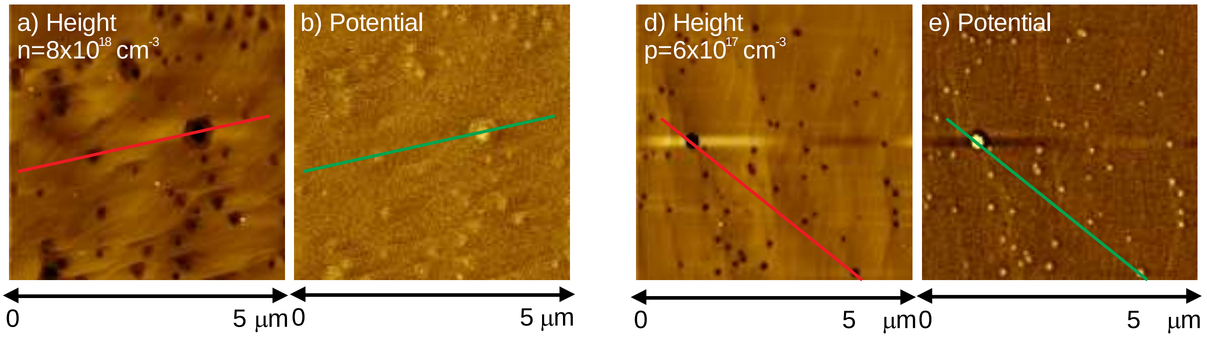

(c) Line scan

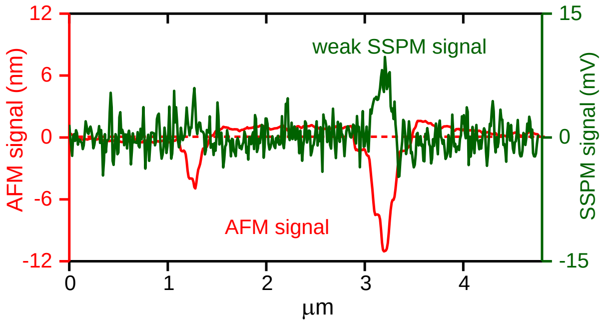

(f) Line scan

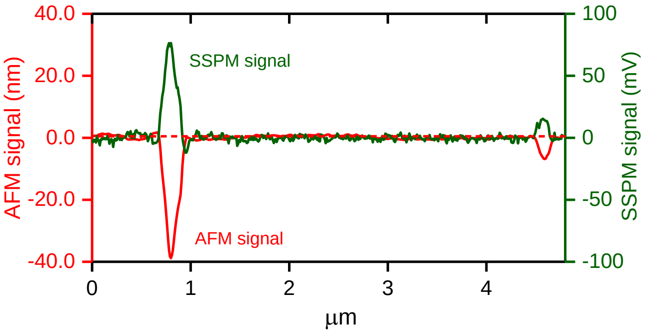

Figure 4.24: Surface images (5x5 μm^2) of an etched Si-doped ($n = 8x10^{18}$ cm^{-3}) GaN surface: **(a)** height profile; **(b)** corresponding SSPM image; **(c)** extracted line scan from (a) and (b) across dislocations; Surface scans (5x5 μm^2) of a Mg-doped GaN ($p = 6x10^{17}$ cm^{-3}): **(d)** height image; **(e)** respective SSPM image; **(f)** extracted line scans through dislocations.

It is notable that Si-doped GaN layers reveal only weakly charged pits with a SSPM signal amplitude ≤10 meV which is in the range on the background noise signal. Undoped and Ge-doped samples also exhibit a similar potential contrast in SSPM mapping profiles as that of Si-doped samples. Moreover, for n-type GaN samples the charge contrast of dislocations is found to be independent of the electron concentration. On the other side, Mg-doped GaN samples exhibit prominently negative charged pits, while increase in hole concentration of GaN:Mg layers enhances the local potential contrast of dislocations with respect to surrounding as depicted in figure 4.25. Similar findings are reported by others for dislocation regions in undoped GaN,[33, 136] n-GaN,[32] and Mg-doped GaN films.[34, 116] In Mg-doped GaN layers negatively charge of surface pits has been associated to an accumulation of Mg^- acceptors around the dislocation.[34, 116] A weak negative charge contrast observed in undoped and n-type GaN can be attributed to coulomb charges trapped at the dislocation core, or trapped by native acceptor defect states manifesting nominally negative charge states.[131, 135]

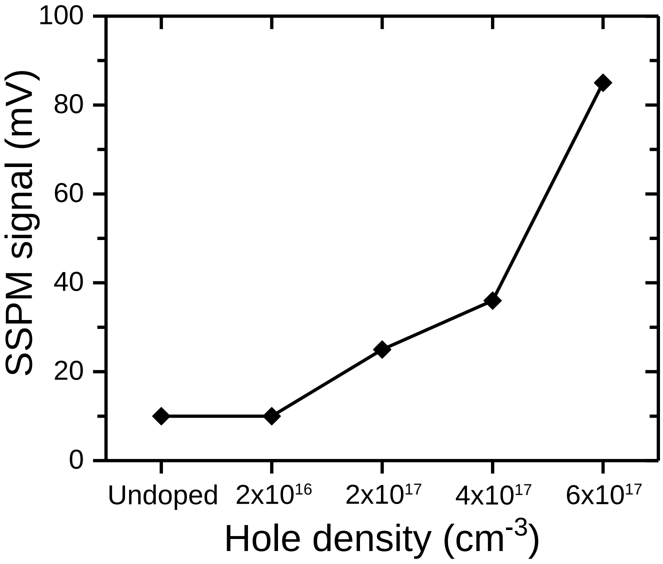

Figure 4.25: SSPM signal strength of GaN:Mg series plotted against the hole density

The comparison of surface potential values of C- and Fe-doped samples with n- and p-type GaN samples reveals that, C- and Mg-doped layers show similar potential due to a Fermi-level position below midgap or near the valence band. In both C- and Mg-doped sample series the charge contrast is observed to increase with increasing doping concentration due to change in Fermi-level position. Whereas the potential distribution around dislocations in Fe-doped GaN layers is more consistent with n-type GaN layers, and unlike GaN:C layers local charge contrast of dislocations is nearly independent of carrier concentration.

4.7 Comparison of intrinsic and precursor based C-doped GaN

As already discussed above highly resistive GaN buffer layers are mainly used in FETs to avoid breakdown within the device (source-drain). There are two different ways to obtain semi-insulating C-doped GaN layers, one is by adjusting growth parameters (intrinsic carbon doping) to include higher concentrations of carbon from the hydrocarbon groups of the Ga precursor, and the other is a precursor based C-doping of GaN layers using propane or other hydrocarbons.[137] For comparison, a carbon-doped GaN sample series was grown containing an undoped reference sample along with one precursor based GaN:C and three intrinsically C-doped GaN samples.

Table 4.5 summarizes the details of growth parameters for samples grown in the series. For sample C1 carbon doping is achieved using propane as a precursor, while high resistivity in C2, C3, and C4 is established by changing the growth temperature and reducing the V/III ratio by a factor of four. Through examination of the change in carbon concentration with growth temperature, an increase in doping concentration from $1x10^{19}$ cm^{-3} to $9x10^{19}$ cm^{-3} between 950 °C and 850 °C is noticed. This is because background C concentration increases with the decrease of growth pressure, temperature as well as NH_3 flow rate.[20]

Table 4.5: Growth parameters for the C-doped samples with carbon concentration, ammonia flux, reactor temperature and FWHMs for (0002) and ($10\bar{1}0$) x-ray ω-scans.

Samples	**Dopant**	**[C] (cm^{-3})**	**NH_3 (sccm)**	**T (°C)**	**FWHM (0002)**	**FWHM ($10\bar{1}0$)**
Reference	undoped		2000	1110	0.067°	0.098°
C1	propane	$5x10^{18}$	2000	1110	0.075°	0.102°
C2	intrinsic	$1x10^{19}$	500	950	0.077°	0.106°
C3	intrinsic	$9x10^{19}$	500	850	0.097°	0.212°
C4	intrinsic	$2x10^{18}$	500	750	0.085°	0.150°

4.7.1 Structural properties of carbon included GaN

In order to investigate the influence of the earlier mentioned growth parameters on structural properties XRD and AFM measurements were applied. The FWHM of x-ray ω-scans obtained for out of plane and in-plane measurements are shown in table 4.5. For precursor based (C1) and intrinsic C-doped (C2) samples, the x-ray ω-scans are slightly broadened as compared to the reference sample. However, screw- and edge-type dislocation densities of C1 and C2 are identical, exhibiting ρ_s around $1.5\text{x}10^8$ cm^{-2} and $\rho_e \sim 7\text{x}10^8$ cm^{-2} respectively. Estimated values of screw- and edge-type dislocations obtained from out of plane and in-plane XRD analysis are found to be highest for intrinsically doped samples C3 and C4. Dislocation densities with edge component as high as $2\text{x}10^9$ cm^{-2} and with screw components in the range of $2\text{x}10^8$ cm^{-2} are extracted for these samples (C3 and C4).

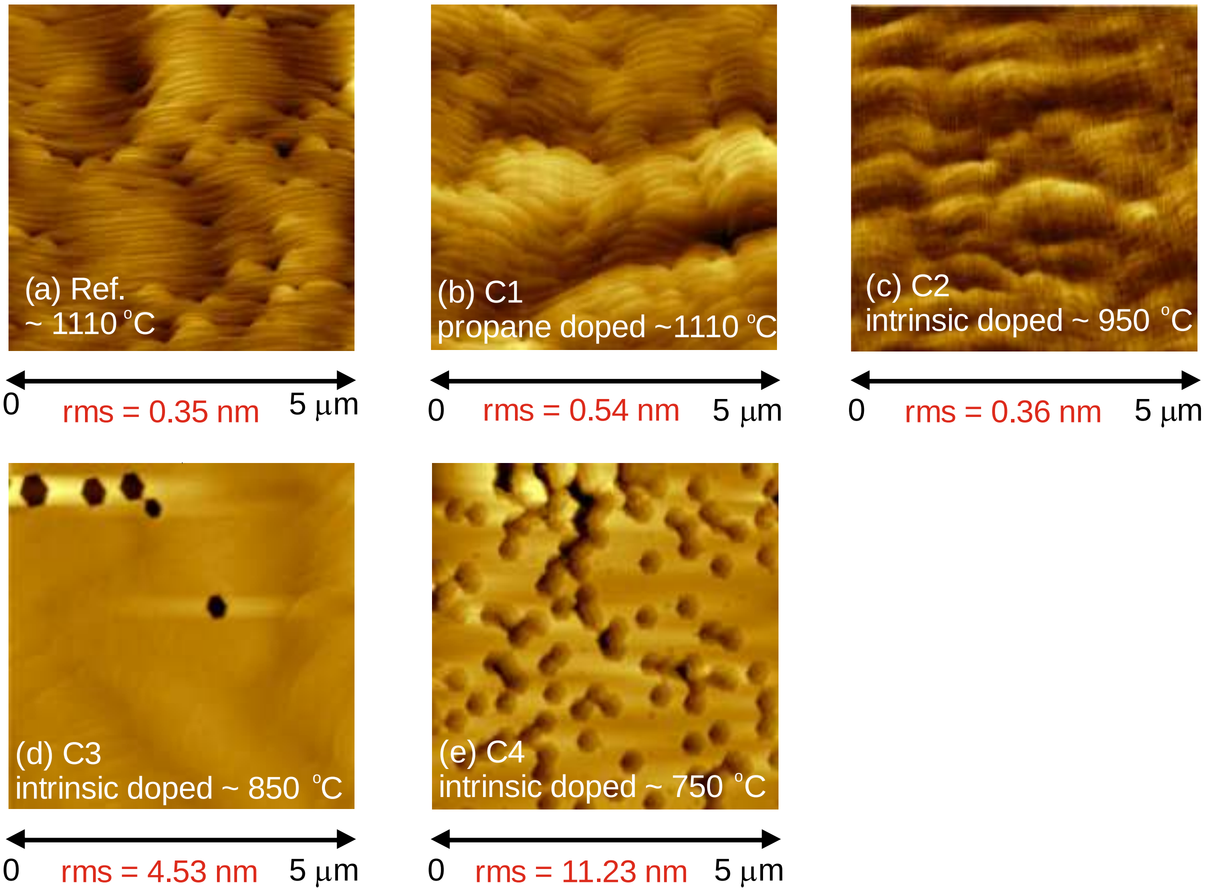

Figure 4.26: 5x5 μm^2 AFM images for reference sample **(a)**, precursor-based C-doped sample **(b),** and intrinsic C-doped samples **(c-e)**.

The dependence of growth conditions on structural properties of highly resistive GaN layers is revealed by the series of images 4.26 (a-f). The AFM profiles of the reference sample, C1 and C2 samples exhibit typical two dimensional atomic growth steps, for sample C1 surface features are more pronounced. The surface morphology of the reference sample is usual for GaN on sapphire [see Fig. 4.26 (a)], with rms ~ 0.35 nm. A modification in surface morphology is observed for sample C1 [Fig. 4.26 (b)] and the rms is found to increase up to 0.54 nm. However, the surface morphology for sample C2 with rms ~ 0.36 nm is similar to the reference sample suggesting that intrinsic carbon doping at this growth temperature has not a strong influence on GaN surface morphology. On the other side the morphology gradually deteriorates for samples C3 and C4 as shown in figs. 4.26 (d, e). Intrinsically carbon doped samples grown at quite low temperatures exhibit hexagonal shaped pits on the surface and very high rms values.

Fig. 4.27 (a) presents a high-resolution AFM image of a 2x2 μm^2 area from the smooth surface region of sample C3 excluding pits as shown in main fig. 4.27 (b). The image contains spiral step growth, which form by the termination of atomic steps due to the intersection of a screw-dislocation component with the film surface.[138] Above this hillock region shown by the dashed square region in fig. 4.27 (b), a hexagonal shaped pit is located. Fig. 4.27 (c) shows a high-resolution image and depth profile of the V-pit found in sample C3 by extracting a line through the pit. These so-called V-shape defects observed in samples C3 and C4 are typically associated to threading dislocations terminated by forming pits with 6 equivalent facets in shape of an inverted hexagonal pyramid. The depth of pit is found to be around 20 nm; however the depth resolution of such V-pits is limited in AFM.

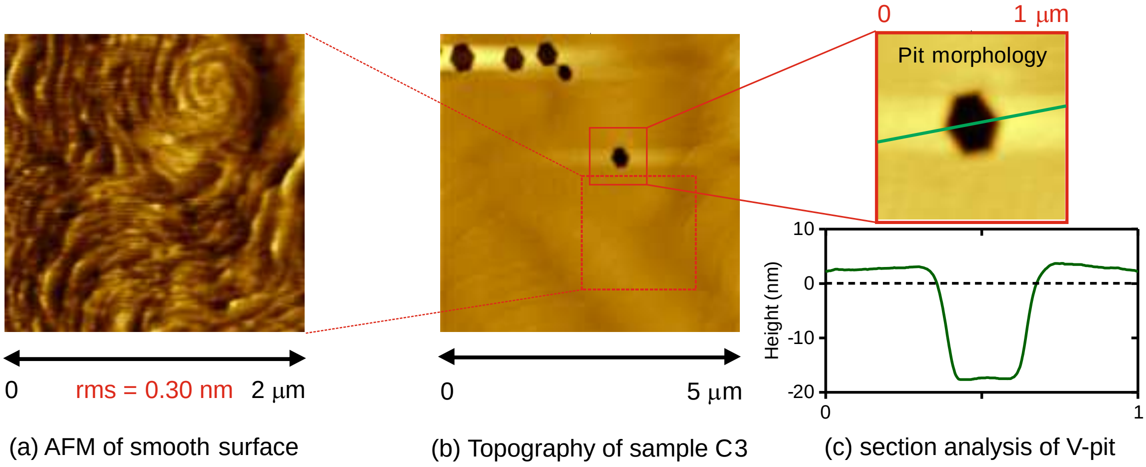

(a) AFM of smooth surface

(b) Topography of sample C3

(c) section analysis of V-pit

Figure 4.27: (a) 2x2 μm^2 AFM image mapped from smooth surface of sample C3; **(b)** 5x5 μm^2 topographic profile of sample C3; **(c)** is the depth profile of a V-pit from high resolution image of sample C3.

4.7.2 Compensation effect of carbon impurities

A comparison of the breakdown field strengths at 295 K as a function of electric current is demonstrated in figure 4.28. It is seen that both intrinsic and precursor-based doping methods can significantly enhance the breakdown field strength above 1.5x10^6 V/cm. The results determine an overall suppression in current leakage and an enhancement of the breakdown field strength above 200 V for a carbon doping level around mid-10^{18} cm^{-3}. This has been achieved by the intrinsic doping method as well as using propane as precursor source. However, sample C1, which was doped using propane, exhibits a breakdown shifted to even higher electric field strengths than the best intrinsically doped samples.

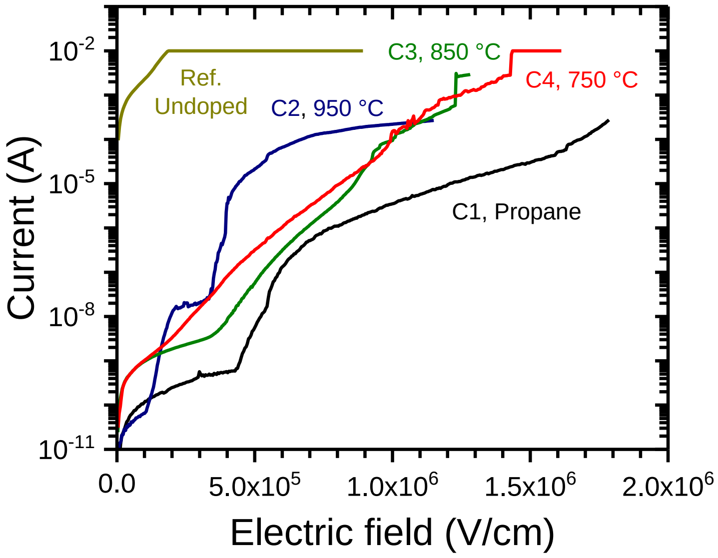

Figure 4.28: Breakdown field measurements at 295 K

A series of 2x2 μm^2 EFM-phase images for the intrinsically C-doped sample C4 is presented in figs. 4.29 (a-d), while fig. 4.29 (e) compares the parabolic curves as determined by EFM measurement of samples C1, C2 and C3 with the reference. We see that all carbon doped samples exhibit a contact potential difference towards the negative DC bias regime, which is associated to a Fermi-level position in the lower half of the band gap. Thus intrinsic carbon doping also tends to shift the Fermi level towards the valence band near carbon acceptor level C_N, nevertheless it degrades the surface quality by introducing pits. Due to large number of pits, it was not possible to perform EFM measurements on sample C4. The comparative study of extrinsically doped (propane based) and intrinsically doped (lowering growth temperature and V/III ratio) GaN:C layers show identical features in EFM and electrical characterizations.

However, the surface morphology is found to be degraded for intrinsic doping at quite low temperature and device breakdown occurs at lower electric field strength.

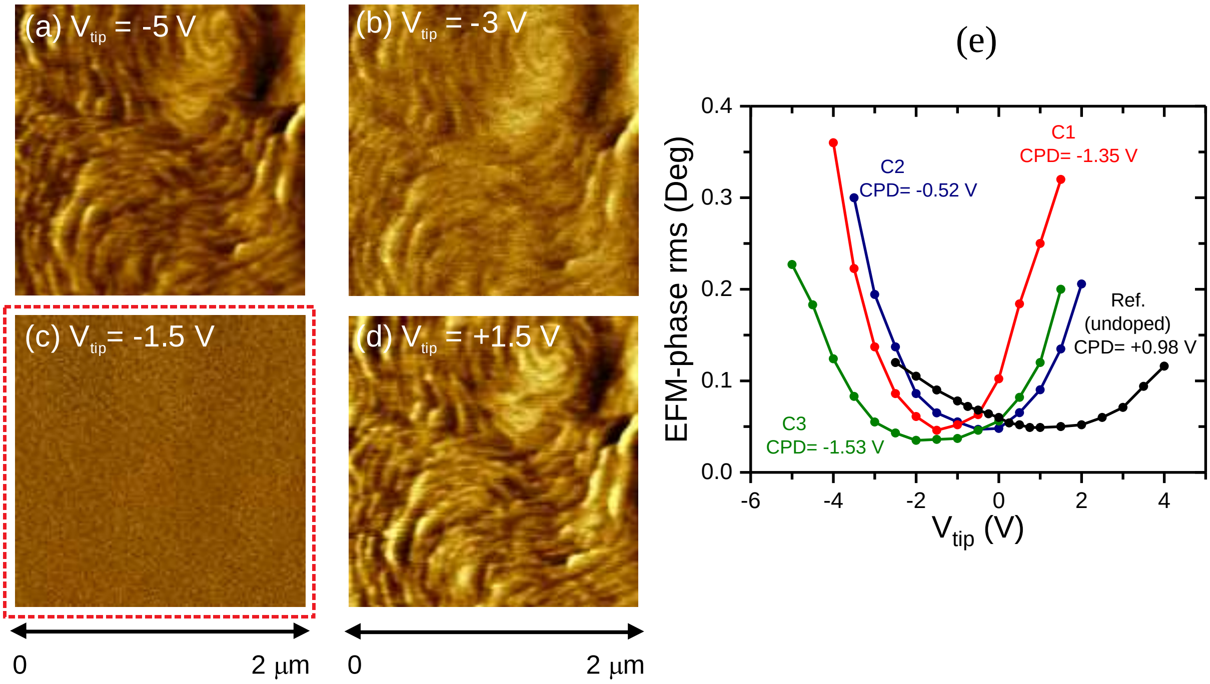

Figure 4.29: (a-d) EFM phase images (2x2 µm^2) of un-etched intrinsically C-doped sample C3 at DC bias of –5 V, –3 V, –1.5 V and +1.5 V; **(e)** EFM parabolic curves of GaN samples.

4.8 Conclusion

Dislocation densities with screw and edge-components as obtained by XRD analysis are in the range of low 10^8 cm^{-2} and low 10^9 cm^{-2}, respectively, and found to be independent of doping type and concentration. A shift of the Fermi-level position with respect to conduction band minimum is a function of dopant type and concentration. Iron and carbon both enhance breakdown voltages by compensating background donors however, the Fermi-level position shifts above midgap for Fe-doping and below midgap for carbon doping at $C \geq 1.6x10^{18}$ cm^{-3}. The negative charge contrast around dislocations found in potential profiles of GaN:C layers can be related to an energetic barrier for electrons trapped at dislocations. Fe-doped GaN layers exhibit no charge contrast.

Thermal activation energies extracted from current transport measurements also confirm the influence of impurity type and concentration on leakage behaviour. In vertical transport measurements, C-doped GaN layers exhibit an up to 5 orders of magnitude lower dark current at room temperature and significantly higher thermal activation energy than Fe-doped samples at comparable dopant concentrations. The activation energy in C-doped samples (0.6 eV) is found to be higher than Fe-doped (0.21 eV) for a similar doping concentration. The vertical current leakage paths through dislocations are considered to be responsible for thermal activation energies being lower than the known deep level energy positions. Altogether, carbon doped GaN layers are better suited for electron capture than iron doped because they better block leakage paths via dislocations. In addition thermal activation energy of carbon related acceptor traps is higher than for iron-related acceptors.

Extrinsically doped and intrinsically doped GaN:C layers have identical features in electrical characterization. However, the surface morphology is degraded for intrinsic doping and device breakdown occurs at lower electric field strength.

Chapter 5

Influence of SI-GaN buffer on GaN-based FETs on Si

5.1 Introduction

GaN on Si based high power electronics and RF applications are subject to high electric fields within device structures. Therefore, the growth of semi-insulating GaN buffer layers between device region and the Si substrate is inevitable. In this chapter, related electrical properties of GaN/AlGaN and GaN/AlN/AlInN field effect transistor structures are described. To reduce buffer leakage, GaN buffer layers beneath GaN/AlN/AlInN and GaN/AlGaN heterostructures, respectively, are either doped with iron or carbon. Breakdown voltages in lateral (buffer) and vertical configuration are measured. Moreover, Hall-effect and capacitance-voltage measurements are applied to understand the electronic transport properties and characterize surface and interface related defects.

5.2 Sample details and properties

Figs. 5.1 (a, b) schematically show the layer sequence of AlInN and AlGaN FETs. After an AlN/AlGaN nucleation layer, a 750 nm GaN buffer layer intentionally doped with carbon or iron, followed by a low temperature AlN layer was grown. Subsequently, a 700 nm C- or Fe-doped GaN buffer and a 200 nm undoped GaN channel layer were deposited. A thin AlN spacer layer around 1 nm in thickness was inserted prior to the 10 nm thick AlInN barrier layer to reduce alloy and interface roughness scattering mechanisms,[139] and AlInN FET structures were finalized with a 2 nm thick GaN cap layer on the top. The AlGaN barrier layer is around 20 nm thick, and uncapped GaN/AlGaN heterostructures do not contain an AlN spacer layer. A reference sample with an undoped GaN buffer was also grown for comparative investigations. The In and Al content in AlInN and AlGaN barrier layers is around 14% and 25%, respectively, as assessed by high resolution X-ray diffraction (HR-XRD). Sample details and the concentrations of C and Fe in the semi-insulating GaN buffer layers are summarized in table 5.1. The electrical measurements were performed on Ti/Al/Ni/Au ohmic contacts (source, drain) and Ni/Au Schottky (gate) contacts as illustrated in figure 3.7 (a).

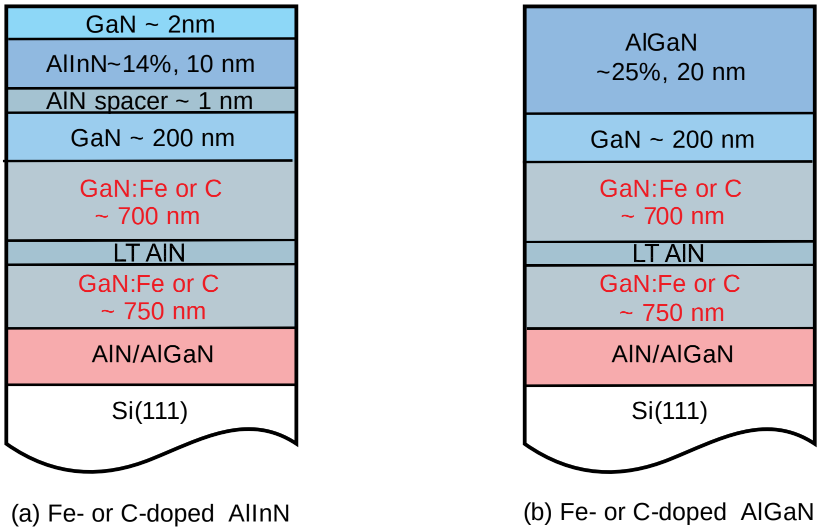

(a) Fe- or C-doped AlInN (b) Fe- or C-doped AlGaN

Figure 5.1: Layer arrangement of AlInN and AlGaN FETs investigated.

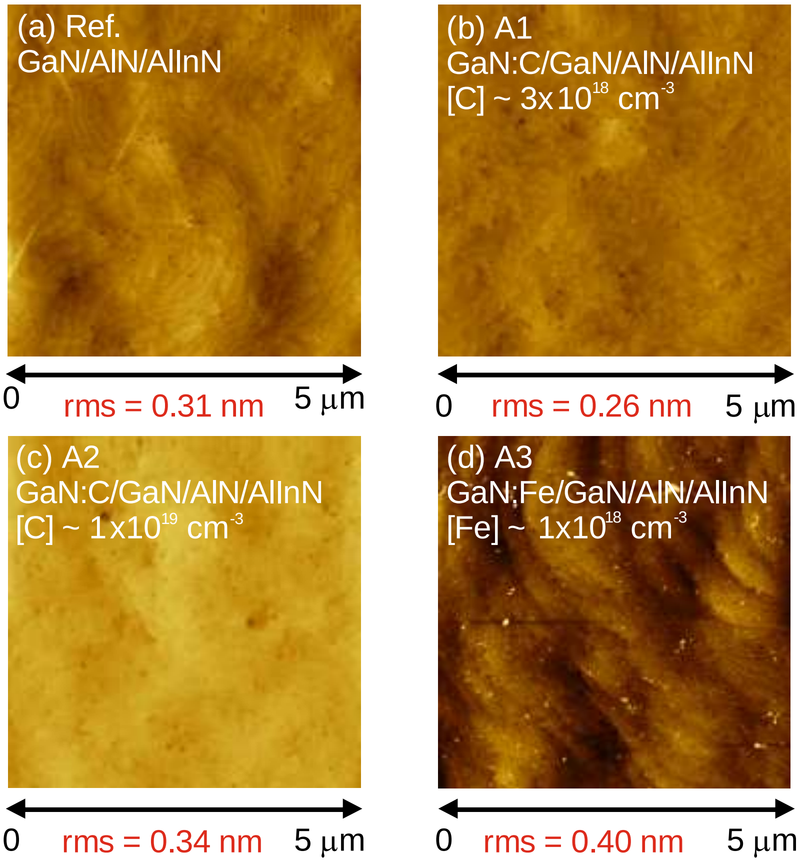

Figure 5.2: Surface morphology and roughness analyses of GaN:C,Fe/GaN/AlN/AlInN structures described in table 5.1.

The role of the surface on the local electronic properties has already been discussed in detail in chapter 4. Surface morphology and roughness analysis were performed by atomic force microscopy measurements in tapping mode. The AFM images in figs. 5.2 (a-d) compare the surface topography of undoped buffer (reference), C-doped and Fe-doped buffer GaN:C,Fe/GaN/AlN/AlInN field effect transistors. All topographic profiles exhibit very smooth surfaces for the top GaN cap layer. The root mean square roughness parameters were obtained from 5x5 μm^2 AFM images. Similar rms values were determined for all samples as illustrated in figure 5.2 however the surface roughness of Fe-doped FET was slightly higher than that of the other samples.

5.3 Transport properties

Here, we examine the two dimensional electron gas properties of GaN/AlN/AlInN and GaN/AlGaN FETs with different buffer layers by Hall-effect and by the transfer length method. The sample details and electric properties provided by Hall-effect and TLM measurements are listed in table 5.1.

Table 5.1: Sample details and electrical properties of the AlInN and AlGaN FETs obtained by Hall-effect, TLM and I-V measurements.

Sample	structure and buffer doping (bottom to top)	μ_H ($cm^2V^{-1}s^{-1}$)	n_{sh} 10^{13} cm^{-2}	R_{sh} (Ω/sq)	TLM R_{sh} (Ω/sq)	TLM R_c (Ω-mm)
Ref.	GaN/AlN/AlInN	463	2.61	516	881	2.5
A1	GaN:C/GaN/AlN/AlInN [C] ~ 3x10^{18} cm^{-3}	1099	2.03	280	191	3.6
A2	GaN:C/GaN/AlN/AlInN [C] ~ 1 x10^{19} cm^{-3}	786	1.94	408	378	2.8
A3	GaN:Fe/GaN/AlN/AlInN [Fe] ~ 1 x10^{18} cm^{-3}	1173	1.64	324	244	3.9
A4	GaN:C/GaN/AlGaN [C] ~ 3 x10^{18} cm^{-3}	1435	0.88	493	495	3
A5	GaN:Fe/GaN/AlGaN [Fe] ~ 4 x10^{18} cm^{-3}	938	0.60	1100	1182	6

It is noteworthy that the reference sample shows very low electron mobility, however, the higher carrier concentration of 2.61x10^{13} cm^{-2} might be due to surface and interface donor states. The values of sheet resistance and Hall mobility of the C-doped GaN/AlGaN sample are in agreement with literature,[140, 141] whereas for GaN/AlGaN heterostructures comprising an iron doped buffer layer with Fe ~ 8x10^{17} cm^{-3}, values of μ_H and sheet carrier concentration around 585 $cm^2V^{-1}s^{-1}$ and $2.24x10^{13}$ cm^{-2} are reported.[142] 2DEG properties for FETs with GaN buffer layer are not deteriorated upon intentional carbon or iron doping.

Transfer length method is conducted using a conventional transfer length pattern consisting of rectangular Ti/Al/Ni/Au ohmic contacts separated by 5 μm to 35 μm spacers with 5 μm increments. Figure 5.3 shows the TLM characteristics of investigated samples while sheet and contact resistances extracted from these plots are described in table 5.1. The linear behaviour indicates a good contact quality for all samples and the values of sheet resistances obtained from TLM method are comparable to Hall-effect measurements. It is noted that total resistivity is the sum of resistivity of all layers connecting metal to two dimensional electron gas and GaN/2DEG interface resistivity.

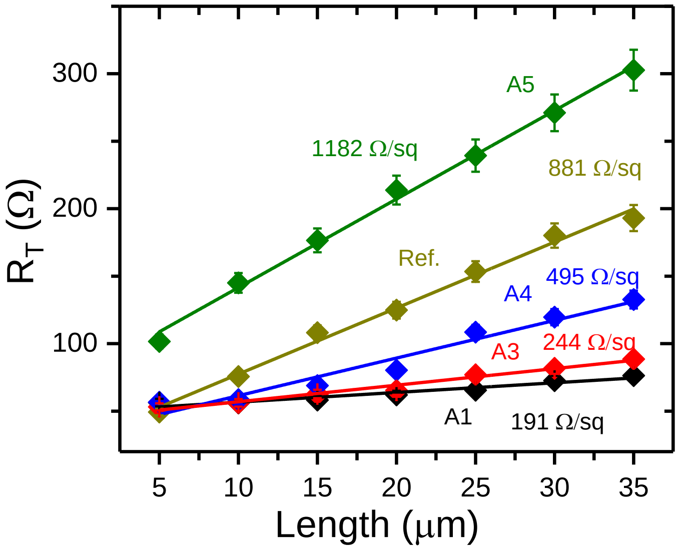

Figure 5.3: Sheet resistance determination from transfer length measurements

5.4 Breakdown voltages of Fe- and C-doped buffer FETs

In this section GaN/AlN/AlInN and GaN/AlGaN heterostructures with different buffer layers are discussed, in perspective of buffer and vertical leakages through device structures. To measure the buffer conductivity, the current-voltage characteristics at room temperature were investigated in lateral or planar configuration using the contact layouts shown in fig. 5.4 (b). For this purpose two isolated ohmic (Ti/Al/Ni/Au) contacts of size 100x100 μm^2 separated by a distance of 100 μm were fabricated by evaporation, while mesa isolation with etch depth ~ 500 nm was achieved by inductively coupled plasma reactive ion etching using chlorine/argon. Vertical breakdown voltages of GaN buffer structure were measured through the complete FET layer structure using top and bottom electrodes as illustrated in fig. 5.4 (c). The breakdown voltage measurements determined in lateral and vertical contact schemes are plotted in figs. 5.5 (a) and (b) respectively.

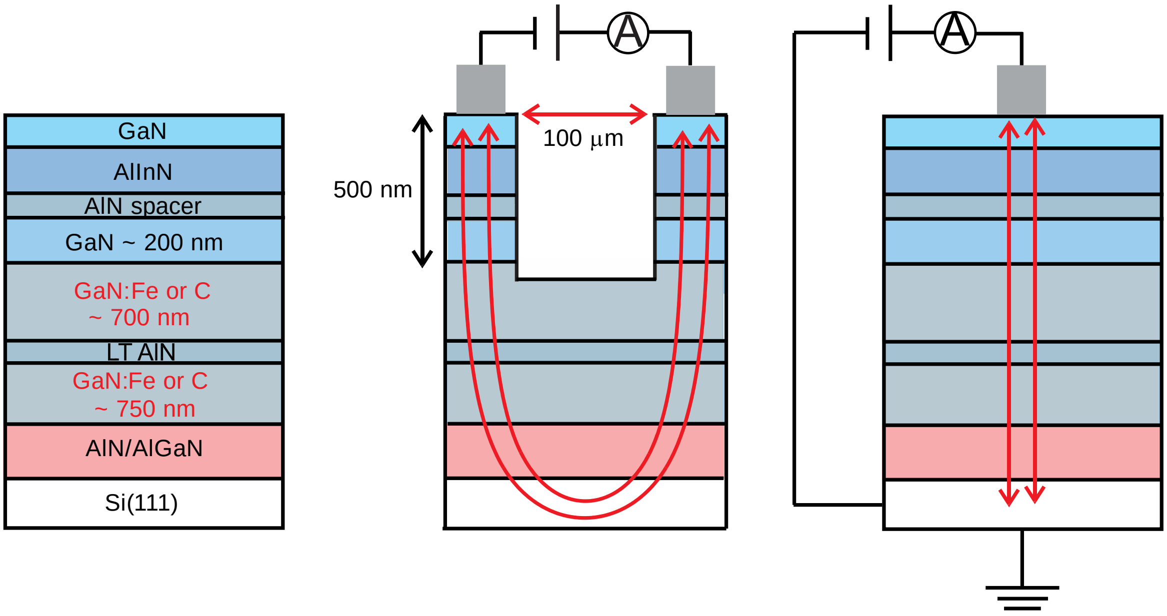

(a) Structure diagram (b) Lateral contacts geometry (c) Vertical I-V schematic

Figure 5.4: (a) structure diagram and schematic arrangement of contacts for breakdown voltage measurements in lateral **(b)** and vertical **(c)** configurations respectively.

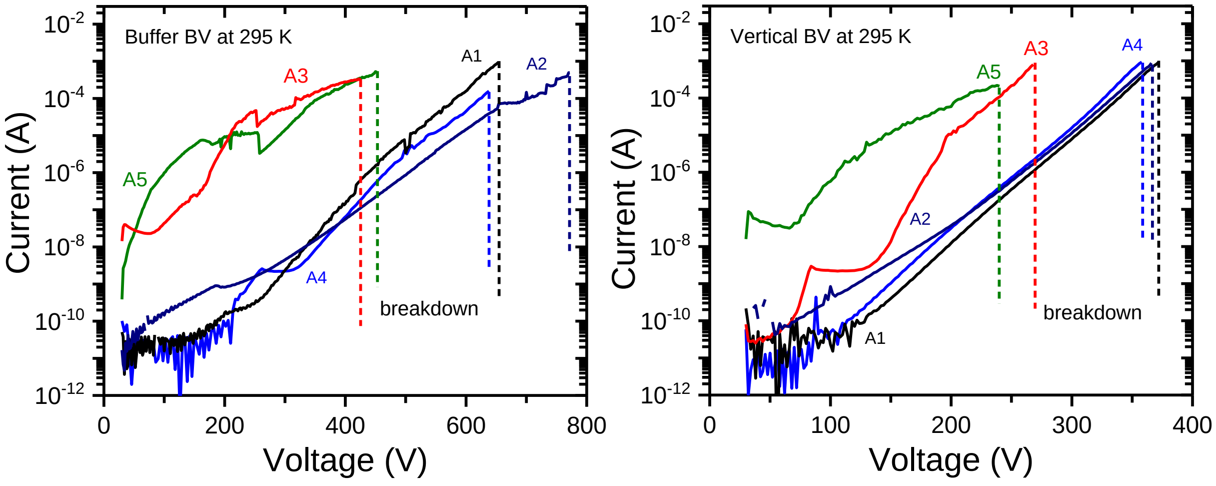

(a) (b)

Figure 5.5: (a) Buffer breakdown voltage measurements obtained in lateral contact layout; and **(b)** Vertical breakdown voltage measurements through the FET structures.

AlInN and AlGaN FETs with Fe-doped buffer structures enhance the breakdown voltages and the electric field strength up to 400 V and 1.5x10^6 V/cm respectively in lateral configuration, while in vertical contact arrangement breakdown voltages of 280 V with field strength of 1.9x10^6 V/cm are achieved. In contrast C-doped buffer FETs offer higher breakdown voltages of 750 V with field strength 2.6x10^6 V/cm for lateral buffer leakage, and breakdown voltages above 350 V with 2.4x10^6 V/cm for vertical contact arrangements. The values of specific resistivities for carbon and iron-doped buffer FETs are obtained around 1.5x10^6 Ω-cm and 2x10^5 Ω-cm for lateral, and 2.8x10^5 Ω-cm and 1.4x10^5 Ω-cm for vertical measurements of the devices. These results demonstrate enhanced breakdown properties of devices with C-doped buffer in comparison with Fe-doped buffers, suggesting carbon doping more suitable for power electronics applications.

5.5 DC characterization

Fig. 5.6 (a) plots the transfer characteristics of C- and Fe- buffer doped GaN/AlN/AlInN FETs to determine the threshold voltage (V_{th}) for the devices. The drain was biased at 10 V with reference to source. At V_{GS} of +2 V the peak value of drain current is around 28 mA and threshold voltages are below –5 V for all samples. V_{th} shifts to higher reverse bias with an increase in doping concentration. FETs with C-doped buffer (A1 and A2) exhibit slightly more negative threshold values due to higher carbon content as compared to iron doped FET structure (A2). Both C- and Fe-doped semi-insulating buffer layers minimize the off-state leakage currents in comparison with reference sample. Lowest off-state drain leakage currents are related to highest carbon-doping concentration in the GaN buffer which is consistent with the results on breakdown voltage.[25]

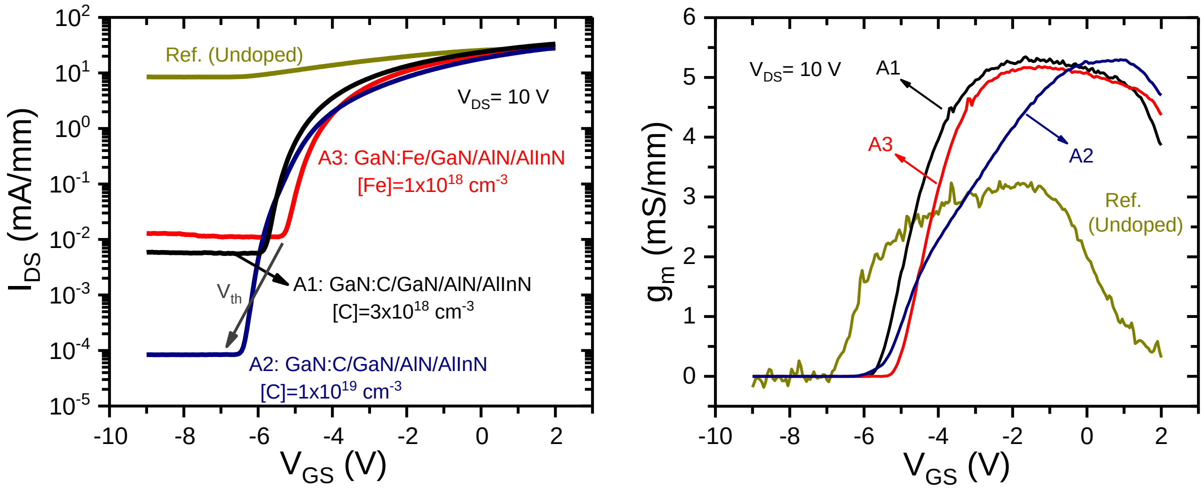

(a) (b)

Figure 5.6: (a) Transfer characteristics and **(b)** transconductance of FETs at V_{DS} = 10 V.

Table 5.2: Transfer characteristics of processed FETs with C- or Fe-doped buffer structures

Sample	**V_{th} (V)**	**g_m(max) (mS/mm)**	**I_{DS}(off) mA/mm**
Ref.	– 6	3.19	8.5
A1	– 5.84	5.3	6×10^{-3}
A2	– 6.48	5.3	1×10^{-4}
A3	– 5.32	5.17	1.1×10^{-2}

Transfer characteristics of FETs with Fe- or C-doped GaN buffer structures reveal higher transconductance (g_m) maxima in comparison with the reference sample, which exhibits a broadened transconductance profile [Fig. 5.6 (b)]. The maximum value of g_m is nearly the same in both Fe- and C-doped FETs. Maximum transconductance is reached at a gate voltage of –1.6 V. After approaching the 2DEG equilibrium (maximum g_m) the current density becomes constant with further increase in V_{GS} while at positive bias a fall of g_m is seen. Table 5.2 summarizes the transfer characteristics of GaN/AlN/AlInN FETs with C- and Fe-doped GaN buffer structures.

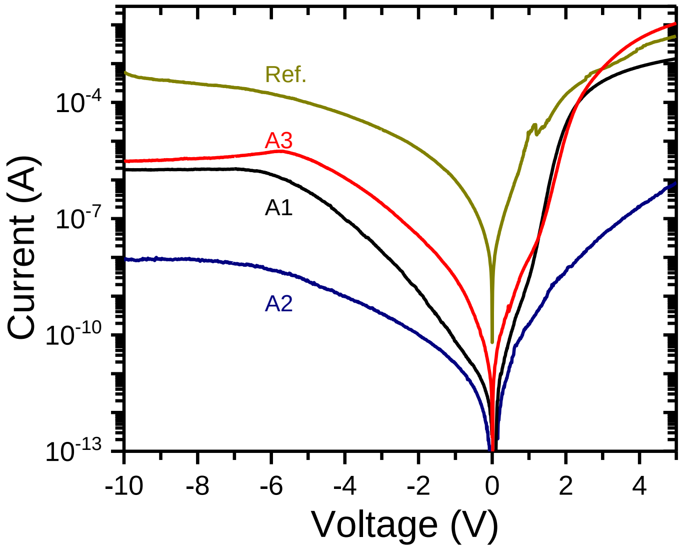

Figure 5.7: RT I-V characteristics measured between gate and drain contacts of undoped, carbon, and iron doped buffer GaN/AlN/AlInN FETs.

The current-voltage curves recorded between the gate (Schottky) and drain (ohmic) contacts for an applied bias ranging from –10 V to +5 V are displayed in figure 5.7. Here doping with C significantly reduces reverse current leakages while the forward currents are not strongly affected. Forward-bias I-V characteristics are analyzed to determine the series resistance and barrier height using the Eqs. 2.18 and 2.20.[80] The reference sample has the highest value around 308 Ω while the C- and Fe-doped device structures exhibit series resistances of 253 Ω and 296 Ω, respectively. These values are more or less the same for similar Fe- and C-concentration. However, heavily C-doped FET (A2) has comparatively large series resistance around 357 Ω due to low electron mobility. At room temperature the obtained values of barrier heights are around 0.87 eV, nearly equal for all buffer doped samples however for the reference sample a comparatively low barrier height of about 0.75 eV is measured, which can be attributed to inferior material quality. These results are in agreement with previous reports[79, 143] of GaN/AlN/AlInN and C-doped GaN/AlGaN heterostructures.

5.6 Depletion characteristics

To extract the 2DEG carrier concentration as a function of depletion depth, capacitance voltage measurements were performed between gate (Schottky) and drain (ohmic) contacts at room temperature. The C-V curves measured for GaN/AlN/AlInN FETs containing undoped, C- and Fe-doped buffer layers are plotted in figure 5.8. From –10 V (reverse bias) to 10 V (forward bias) the depletion characteristics exhibit two-step behaviour. At forward bias of 5 V, a step like decrease in capacitance occurs (step 1), indicating the depletion of surface and AlInN/GaN (top) layer regions. In the bias range from 0 to –5 V, we see a nearly constant capacitance equivalent to the total capacitance of the AlInN barrier layer. In this bias regime, a 2DEG exists at the GaN/AlN/AlInN layer sections. At around –5 V a steep decrease in capacitance is observed (step 2), reflecting complete depletion of the 2DEG under the gate contact. For stronger reversed bias (–6 to –10 V) depletion in the GaN buffer layer occurs.

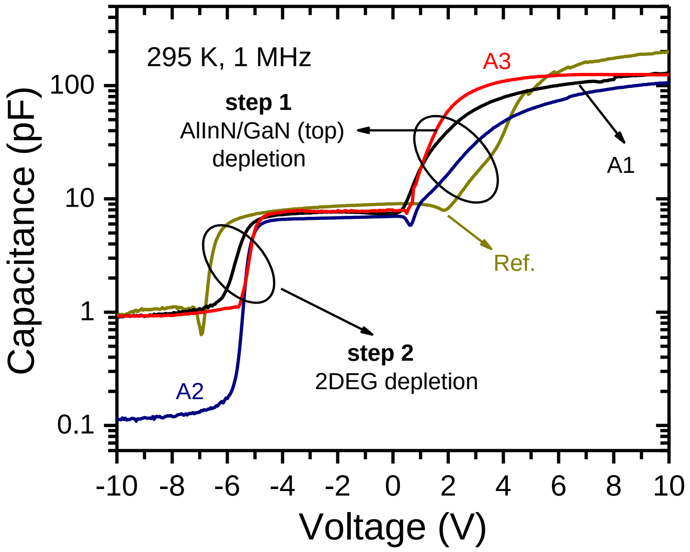

Figure 5.8: C-V characteristics measured between gate and drain contacts of undoped, C- and Fe-doped buffer GaN/AlN/AlInN FETs.

Figure 5.9 portrays an enlarge view of C-V curves in the bias range from 0 to –8 V where 2DEG depletion occurs. For the reference sample, V_{th} is around –6.8 V while FETs with C- and Fe-doped buffer structures have a V_{th} of –6 V and –5.7 V, respectively. All samples show nearly identical slopes for the 2DEG depletion (step 2), however, the sample A2 with [C] = $1x10^{19}$ cm^{-3} has very low capacitance in the deep depletion regime due to the strong compensation effect of C in the GaN buffer. This is in agreement with low leakage currents as observed in the transfer characteristics [Fig. 5.6 (a)].

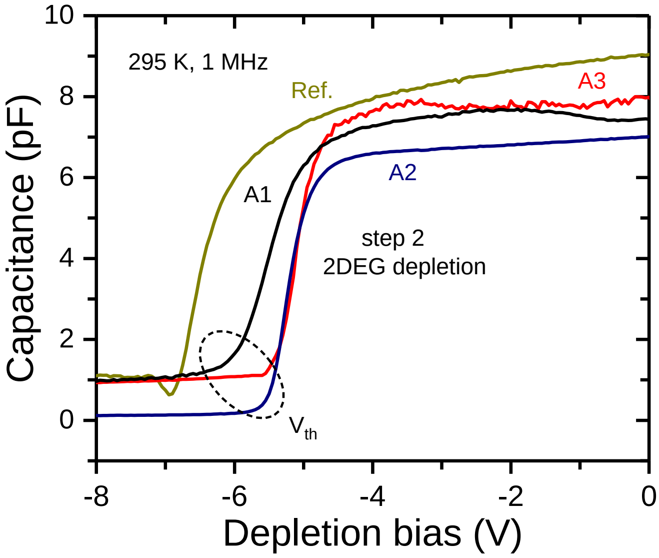

Figure 5.9: Enlarge view of C-V characteristics in 2DEG depletion range.

C-V profiles were further used to calculate the carrier concentration of the 2DEG following Eqs. 2.30 and 2.31, as illustrated in fig. 5.10. The carrier distribution profiles reveal sharp peaks corresponding to the presence of 2DEG at the GaN/AlInN region. Net carrier concentration determined from the area under the curve for C-doped GaN/AlN/AlInN (A1) FET is around $1.9x10^{13}$ cm^{-2} which is comparable to the value obtained from Hall-effect measurement. Reference and Fe-doped GaN/AlN/AlInN (A3) FETs exhibit sheet carrier concentrations about $6.8x10^{12}$ cm^{-2} and $1.3x10^{13}$ cm^{-2} respectively, which are lower than those obtained by Hall-effect measurements. The carrier concentration for the heavily C-doped FET (A2) estimated by C-V measurement is also much lower than the obtained value from Hall measurement. This is due to low capacitance in deep depletion regime for high carbon doping level. Both Hall-effect and C-V measurements indicate that 2DEG properties of GaN/AlN/AlInN FETs are not ruined upon doping with carbon and iron for doping contents in the range of 10^{18} cm^{-3}.

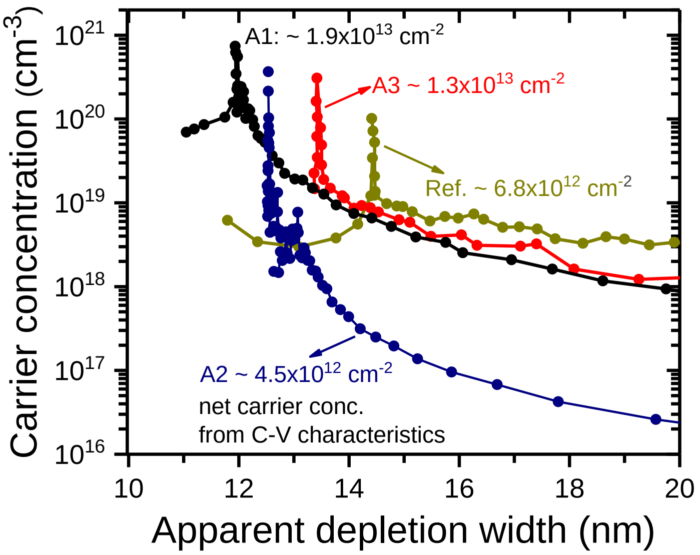

Figure 5.10: Carrier distribution profile as a function of depletion depth.

In order to investigate the influence of semi-insulating doping on defect state distributions, trap densities were evaluated. For this purpose the low-high frequency method was adopted, using 10 kHz as low frequency and 1 MHz as high frequency according to Eq. 2.33. The estimated values of D_{trap} are found to be around $2x10^{12}$ eV^{-1} cm^{-2} in all samples independent of buffer doping which is close to the reported values for GaN/AlGaN and GaN/AlN/AlInN heterostructures.[144, 145] The results from C-V measurements suggest that in our device structures, C and Fe doping does not affect the defect densities distributions.

5.7 Conclusion

The GaN/AlN/AlInN and GaN/AlGaN FETs grown with both C- or Fe-doped GaN buffer layers significantly improve the breakdown field strength and off-state current in comparison to reference test devices with undoped GaN buffer structures. The Fe-doped buffer FETs enhance the electric filed strength up to $1.5x10^6$ V/cm and $1.9x10^6$ V/cm in lateral and vertical contact arrangements respectively. C-doped buffer FETs withstand higher electric field strength up to $2.6x10^6$ V/cm for lateral buffer leakage, and above $2.4x10^6$ V/cm for vertical contact configuration. For a comparable doping concentration, the specific resistivity of a heterostructure with a Fe-doped buffer structure is around $2x10^5$ Ω-cm which is one order of magnitude lower than a device structure with C-doped buffer ($1.5x10^6$ Ω-cm). The Hall-effect and capacitance-voltage characteristics of C and Fe doped buffer FETs show that 2DEG properties are not declined upon doping with carbon or iron and buffer doping is also not found to change defect density distributions.

Chapter 6

Effect of SiN passivation on GaN/AlN/AlInN heterostructures

6.1 Introduction

The performance of GaN-based FETs is thought to be limited due to surface states which are responsible for the current slump and decrease in drain current at radio-frequency operation. One of the key methods to reduce current collapse and gate leakage is the insertion of a SiN passivation layer on the AlInN or AlGaN barrier layer. In this chapter, the influence of a SiN surface passivation layer on GaN/AlN/AlInN heterostructures is explored in the context of defect characteristics and current leakage mechanisms. The leakage transport mechanisms are discussed by employing current-voltage measurements while capacitance-voltage, admittance and thermally stimulated current measurements are used as defect characterization tools.

6.2 Sample details and basic properties

Figure 6.1 (a) shows the layer structure of the GaN/AlN/AlInN heterostructures with SiN cap. Indium concentration in the 5 nm thick AlInN layers is around 15 %. Two-dimensional electron gas mobility of AlInN and AlGaN FETs is usually restrained due to alloy and interface roughness scattering mechanism occurring at the heterointerface between AlInN and GaN layers.[139] In order to enhance the conduction band offset and the 2DEG confinement, and hence to increase 2DEG concentration and mobility, an AlN spacer layer (d_{AlN}) of around 2 nm in thickness was grown prior to the AlInN layer.

The reference sample is uncapped while three passivated samples contain in-situ deposited SiN passivation layers with thicknesses (d_{SiN}) of around 2 nm, 5 nm, and 9 nm respectively. Table 6.1 presents the details of the investigated SiN passivated GaN/AlN/AlInN sample series. In order to perform electrical measurements, two-terminal device structures consisting of ohmic Ti/Al/Ni/Au (20/50/15/100 nm) and Schottky Ni/Au (15/100 nm) contacts were fabricated as shown in fig. 6.1 (b). The test device for I-V and C-V investigations forms therefore a metal-insulator-semiconductor diode. Due to the insulating SiN capping layer above the AlInN barrier Hall-effect measurements on passivated samples were not possible as the required dry etching led to poor contact quality. The sheet carrier concentration within the 2DEG regime was calculated from C-V characteristics.

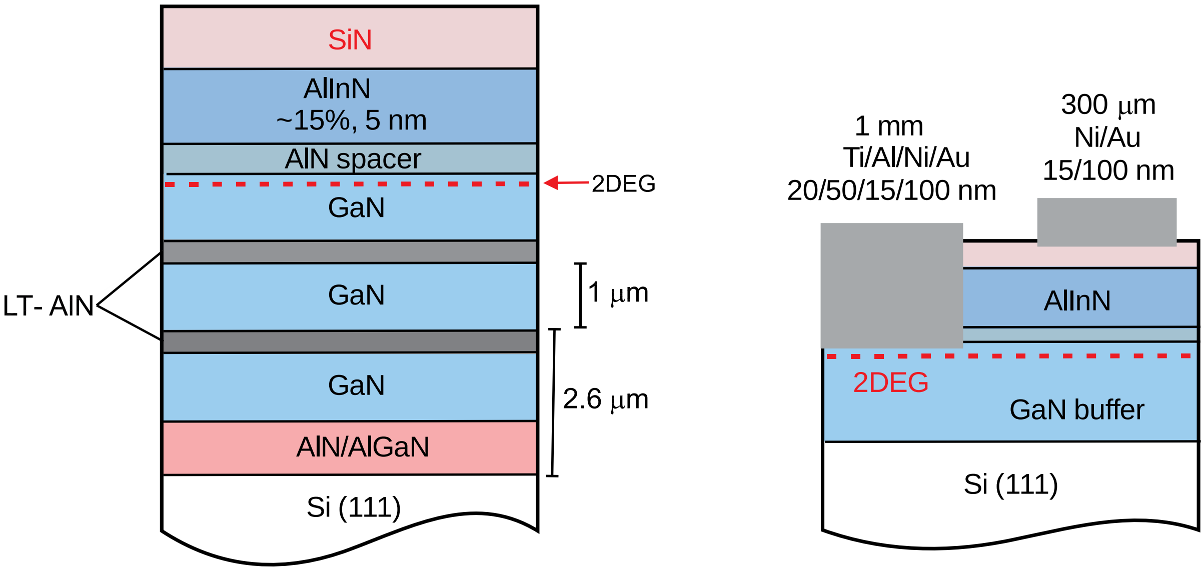

Figure 6.1: (a) Scheme of the layer arrangement of a GaN/AlN/AlInN/SiN heterostructure (d_{SiN} varied from 0 to 9 nm); **(b)** Contact layout of a test device for electrical measurements.

Table 6.1: Details of the GaN/AlN/AlInN/SiN sample series

Sample No.	**1**	**2**	**3**	**4**
[In] (%)	15	15	15	15
d_{AlInN} (nm)	5	5	5	5
d_{SiN} (nm)	0	2	5	9
carrier conc. from C-V (10^{13} cm^{-2})	2	1.8	1.6	1.3

6.3 Effect of SiN passivation on surface leakage

The room temperature I-V characteristics of all samples are plotted in figure 6.2 (a). Reverse (leakage) currents for sample #1 (without SiN capping layer) and #2 with d_{SiN} = 2 nm are relatively high, however, for samples #3 and #4 with thicker SiN passivation layers, reverse currents are lower by up to two orders of magnitude. Leakage currents at a bias of –4 V are compared in figure 6.2 (b). There is a significant suppression of reverse bias leakage currents for samples upon passivation with $d_{SiN} \geq 5$ nm, which demonstrate good insulating properties of the SiN layer. In forward bias direction above 1 V, the passivation treatment also results in a substantial decrease in current as compared to the reference sample. In previous work,[146, 147] the reduction in leakage currents in GaN/AlGaN FETs due to alleviation of electric field after SiN deposition is reported.

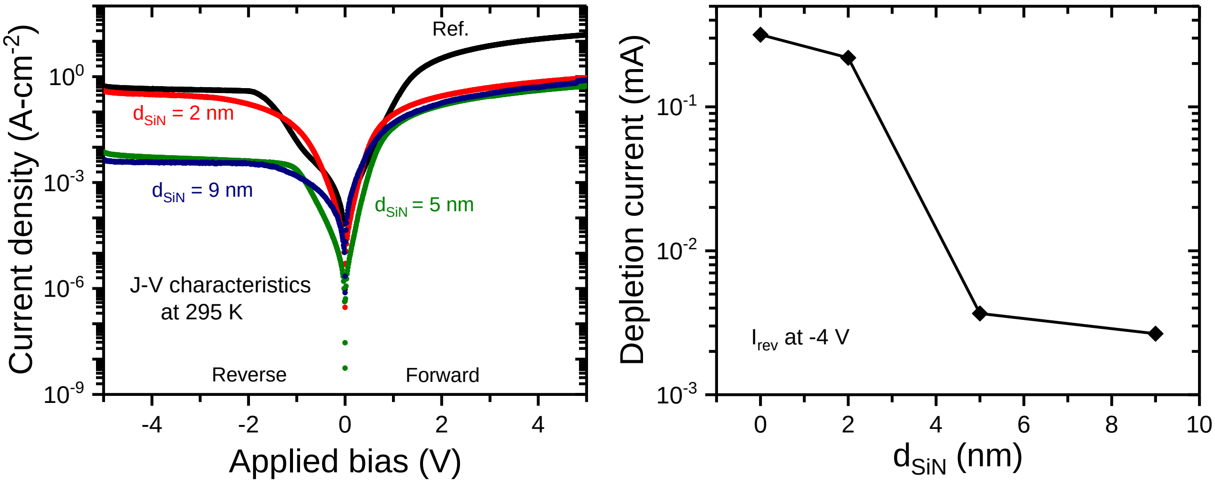

(a) (b)

Figure 6.2: (a) Reverse and forward current-voltage characteristics of an MIS diode with differently thick SiN passivation layer at 295 K; **(b)** Reverse current at −4 V plotted as a function of SiN passivation layer thickness.

Diode parameters and contact properties on top of the AlInN/SiN layer were determined by combining the thermionic and diffusion model for Schottky contacts with the Cheung and Cheung method using Eqs. 2.18 and 2.20.[80, 81] Figure 6.3 (a) shows a linear dependence in Cheung's function (H(I)) versus I plots for all samples.[81] Barrier heights and series resistances of the GaN/AlN/AlInN heterostructures obtained from intercepts and slopes of linear curves are drawn in figure 6.3 (b). Here the resistance obtained from I-V characteristics is not only the resistance of the top AlInN barrier layer but it also includes the AlN spacer and GaN buffer layer regions.

There is an increase in the values of barrier height ϕ_b and series resistance R_s after the insertion of the thick SiN passivation layer ($d_{SiN} \geq 5$ nm) on AlInN, while a reduction in reverse saturation current is observed. Barrier height is found to be enhanced from 0.58 eV (for the reference sample) to 0.81 eV for the sample with thick SiN layer. According to Schottky-Mott theory,[61] the barrier height of MS contact solely depends on the metal work function and semiconductor electron affinity in the absence of surface states. However the surface properties, interfacial layer thickness, and surface states strongly influence the barrier height of metal-semiconductor systems.[148] It is notable that the values of the ideality factor for all samples are around 2 and nearly equal. Table 6.2 summarizes the obtained values of Schottky parameters. These values are comparable to previous reports of Schottky diodes on GaN/AlN/AlInN heterostructures.[79, 81, 147, 149] The deposition of the SiN capping layer of thickness ≥ 5 nm on AlInN barrier mitigates the reverse leakage current by blocking charge transfer between the metal and AlInN barrier layer.

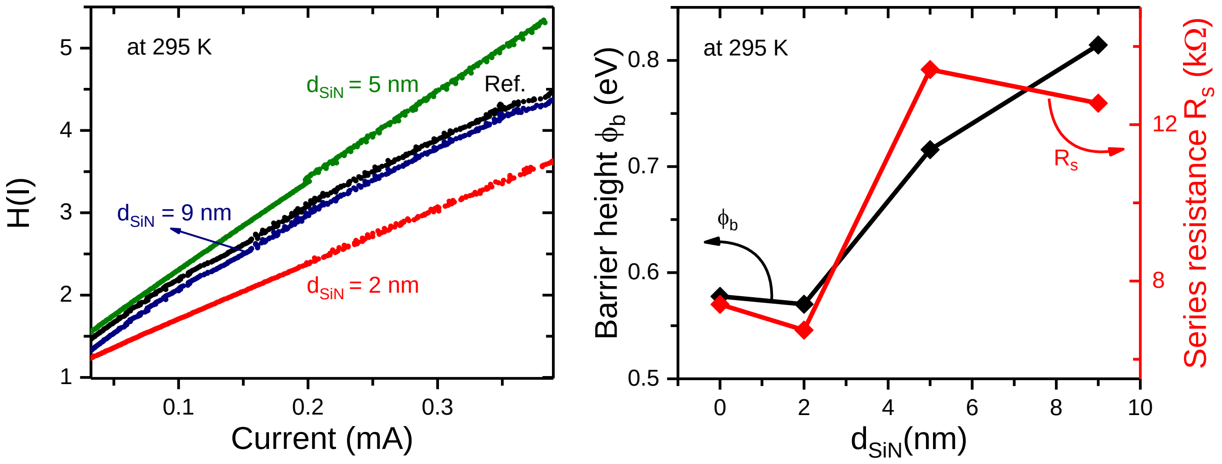

(a) (b)

Figure 6.3: (a) Cheung's function H(I) versus I plots as obtained from forward bias I-V data; **(b)** ϕ_b and R_s as derived using the Cheung and Cheung formula[5] [Eqs. 2.18 and 2.20].

Table 6.2: SiN passivation layer thickness dependent values of Schottky parameters: ideality factor n, barrier height ϕ_b, series resistance R_s and reverse saturation current I_o as determined from forward I-V characteristics at room temperature.

Sample No.	d_{SiN} (nm)	n	ϕ_b (eV)	R_s (kΩ)	I_o (A)
1	0	2.04	0.58	7.4	1.5×10^{-8}
2	2	1.96	0.58	6.7	5.1×10^{-9}
3	5	1.89	0.72	13	2.1×10^{-9}
4	9	1.96	0.81	12.5	5.6×10^{-9}

6.4 Leakage current mechanisms

It is well known that the charge transport behaviour in MIS structures is often controlled by the contact limited Fowler-Nordheim tunneling, trap-assisted tunneling, and Frenkel-Poole emission mechanisms.[150] The current-voltage characteristics measured at various temperatures for sample with 9 nm thick SiN cap layer are depicted in figure 6.4. All samples exhibit similar dependence of current densities over temperature. These measurements are used to examine the current transport mechanisms in GaN/AlN/AlInN/SiN heterostructures according to their bias and temperature dependent behaviour.

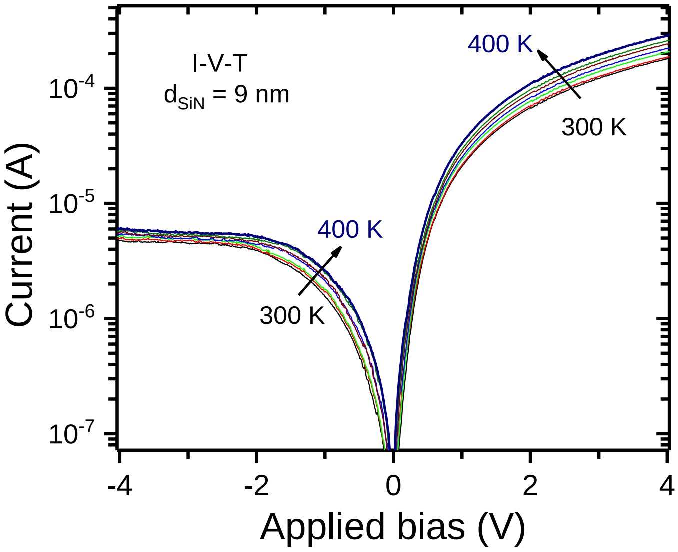

Figure 6.4: Forward and reverse bias I-V characteristics of GaN/AlN/AlInN structure with 9 nm thick SiN layer at different temperatures.

6.4.1 Forward bias analysis

Figure 6.5 (a) illustrates the trap-assisted tunneling current density (J_{TAT}) versus E^{-1} plots measured at different temperatures for high forward bias regime (above +2 V), where the linear behaviour follows Eq. 2.22[82] and therefore supports a two-step trap-assisted tunneling mechanism. Here, only the characteristic curves for sample #4 with d_{SiN} ~ 9 nm are drawn. The reference sample without any SiN passivation layer reveals also a linear behaviour with a trap activation energy ϕ_t of 0.44 eV. The trap energies of passivated samples with thick SiN layers are 0.46 eV and 0.52 eV which are only slightly higher than for the reference sample [Figure 6.5 (b)]. In a previous report, Dutta et al.[82] extracted a trap level around 0.26 eV in GaN/AlN/AlInN which is substantially lower than the extracted values in this work.

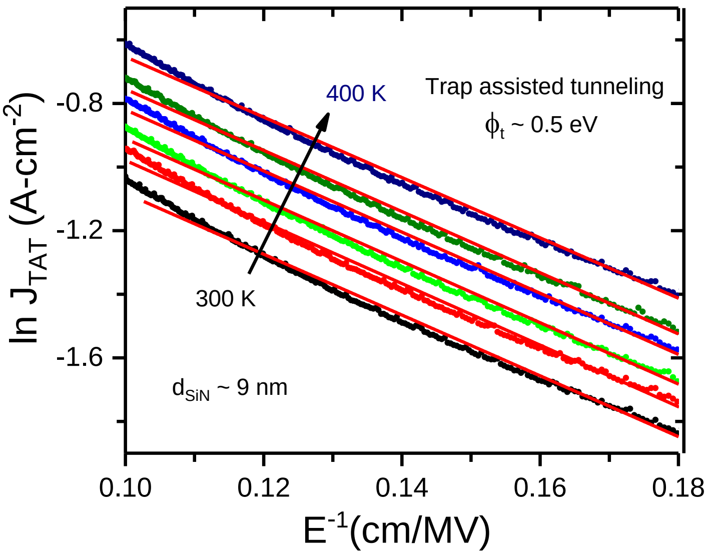

(a)

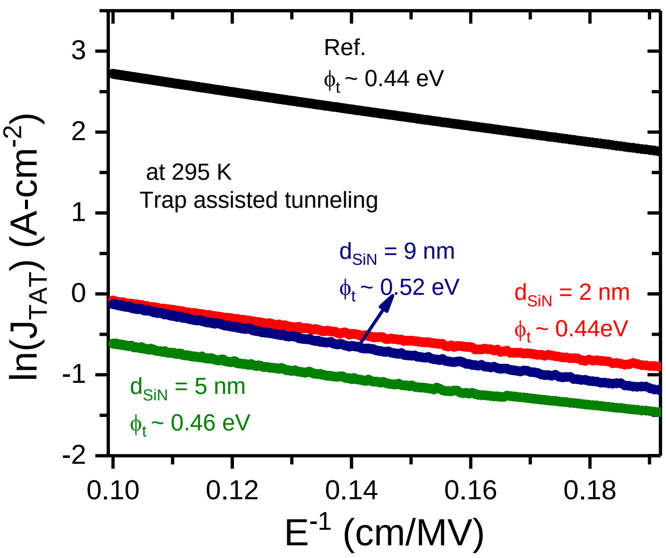

(b)

Figure 6.5: (a) Trap assisted tunneling plots in high forward bias regime of a sample with d_{SiN} = 9 nm in the temperature range from 300 K- 400 K; **(b)** Trap assisted tunneling plots of all samples obtained at 295 K.

In low forward bias regime (≤ 1.8 V) ln(J) versus E^{-1} plots are deviating from straight lines which suggest that the energy of electrons is not sufficient to cross the potential barrier by TAT process. However there is a finite probability for electrons of tunneling through the potential barrier.[83, 84] It is indicated in figure 6.6 that only the reference sample exhibits an $\ln(J_{FNT}/E^2)$ over E^{-1} dependence as follows from equation 2.23 for a Fowler-Nordheim tunneling process. The effective barrier height for the reference sample is around 0.50 eV which is agreement with the barrier height obtained from thermionic emission theory. On the other hand, all SiN passivated samples deviate from a linear behaviour. Obviously, SiN increases the tunneling distance and/or barrier which decrease tunneling probability.

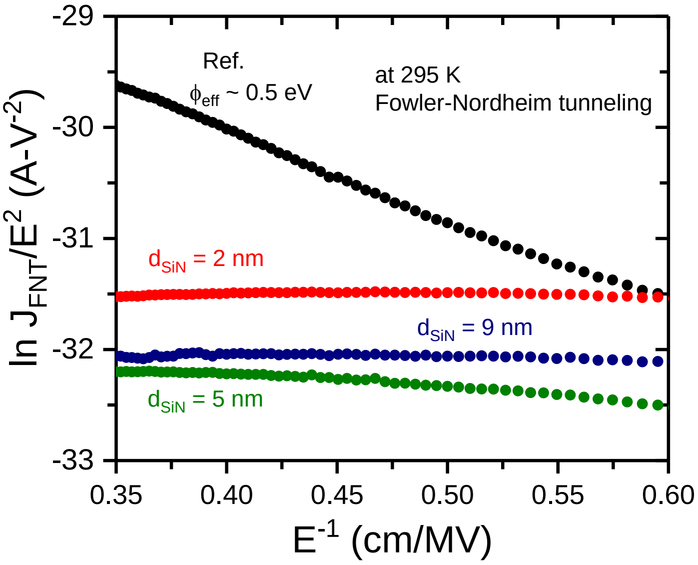

Figure 6.6: The ln(J/E^2) versus E^{-1} plots of GaN/AlN/AlInN/SiN structures for Fowler-Nordheim tunneling process.

6.4.2 Reverse bias analysis

In reverse direction, the Frenkel-Poole emission is considered as the dominant transport mechanism in MIS heterostructures which describes an electric-field enhanced thermal emission of carriers from trapped states into the barrier.[86] An analysis of the Frenkel-Poole emission for the sample with d_{SiN} ~ 5 nm, obtained from I-V characteristics in reverse regime is interpreted in figure 6.7 (a), where circles are data points and solid red lines are linear fits. The ln(J_{FP}/E) versus $\sqrt{\mathbf{E}}$ curves are nearly straight lines as predicted from Eq. 2.25 confirming the dominance of Frenkel-Poole emission in this regime.[82, 83] Some deviation from linearity might be due to the presence of other parallel transport mechanisms along with Frenkel-Poole emission. The parameter b(T) is the intercept extracted at each temperature from a linear fit of the J/E vs $\sqrt{\mathbf{E}}$ plots. Figure 6.7 (b) plots the parameter b(T) as function of inverse temperature (1000/T) in accordance with Eq. 2.27 to obtain the emission barrier height for a trap responsible for Frenkel-Poole emission.

All samples reveal Frenkel-Poole emission but samples with thick SiN layers exhibit comparatively strong temperature dependence. The emission barrier height is increased from 0.15 eV (for reference sample) to 0.31 eV for sample with d_{SiN} = 5 nm. Our results of passivated samples are only slightly lower than previous work where the emission barrier height is determined around 0.38 eV for SiN passivated GaN/AlN/AlInN[82] and GaN/AlGaN[147] heterostructures. Arslan et al.[86] reported trap energy of 0.12 eV for Schottky contacts on GaN/AlN/AlInN heterostructures which is close to the value 0.15 eV obtained for reference sample in our investigations. Dislocation related trapped states are commonly considered to be responsible for these emissions. In our GaN/AlN/AlInN structures, we find two different mechanisms; trap assisted tunneling and Frenkel-Poole emission, to be dominant for current transport in forward and reverse directions, respectively.

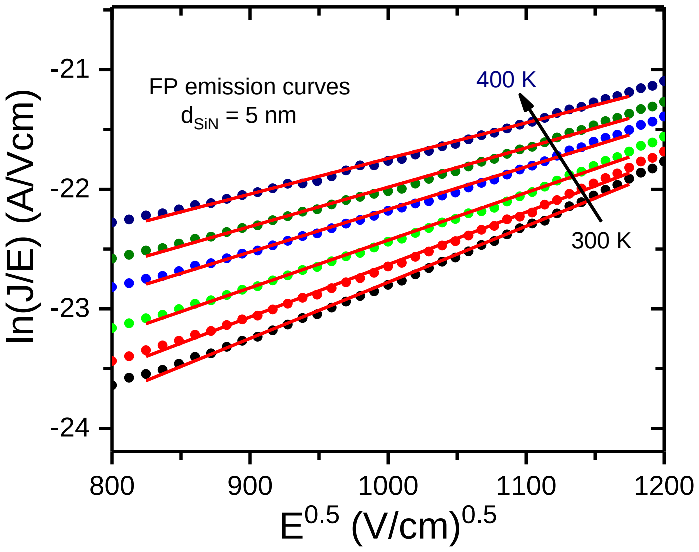

(a)

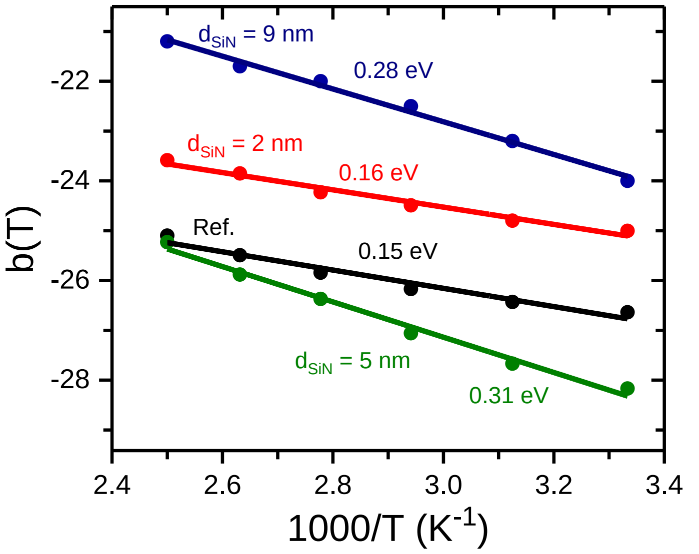

(b)

Figure 6.7: (a) Frenkel-Poole emission plots for reverse bias regime of I-V characteristics for sample with d_{SiN} =5 nm; **(b)** Arrhenius plot of all samples exhibiting emission barrier heights.

6.5 Depletion layer characterization

To investigate the passivation effect of the SiN layer on defect distribution, capacitance-voltage and admittance spectroscopy measurements of the GaN/AlN/AlInN/SiN-metal contacts are conducted. Typical C-V profiles of all samples obtained at room temperature and 10 kHz, when reverse bias from 0 to –5 V with a 50 mV modulation amplitude is applied, are demonstrated in figure 6.8 (a).

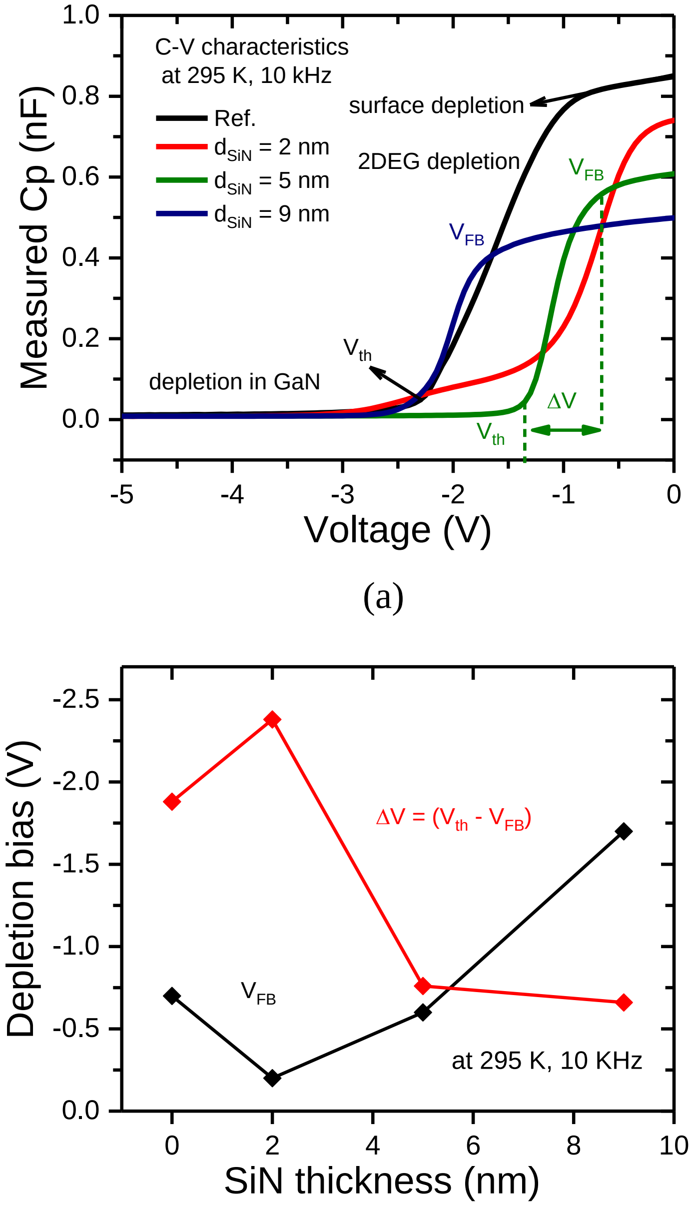

(a)

(b)

Figure 6.8: (a) Parallel capacitance-voltage characteristics at 295 K and 10 kHz of SiN capped FET structures and the reference sample; **(b)** Corresponding flat band voltage and ΔV in dependence of the SiN layer thickness.

By considering a parallel arrangement of RC dispersions, the measured parallel capacitance (C_p)- voltage characteristics of GaN/AlN/AlInN heterostructures fall into three different voltage ranges.[104] First, the regime between zero bias and the flat band voltage V_{FB} (defined as the inflection point when the capacitance curve drops significantly) reflects the depletion of the barrier involving both the AlInN and the AlN layer.[151] Around zero bias, the 2DEG accumulates at the barrier layer leading to a high capacitance value. The second regime, spanning from the drastic capacitance drop from V_{FB} to the much softer decrease in capacitance, can be attributed to the depletion of the 2DEG. Beyond threshold bias (V_{th}) for full 2DEG depletion, the third regime is characterized by a nearly constant capacitance representing the GaN/AlN/AlInN heterostructure at high reverse bias.

The insertion of SiN dielectric layer determines a decrease of the accumulation capacitance in the GaN/AlN/AlInN heterostructures. For a parallel equivalent circuit configuration, the measured capacitance of a device is affected by the series resistance,[104] which tends to rise with SiN thickness leading to an additional voltage drop. Therefore a systematic change in zero-bias capacitance and the value of flat band voltage V_{FB} with increasing passivation layer thickness is observed. Figure 6.8 (b) reveals that the thickness of SiN passivation layer affects the flat band voltage and ΔV ($V_{th} - V_{FB}$) of test devices. The C-V curves of the samples with 5 nm and 9 nm passivation layer thicknesses show a sharp step, while reference and thin passivation layer samples exhibit comparatively broad C-V curves. In case of thick dielectric layers, reverse leakage currents through the contact are alleviated hence 2DEG channel is more effectively depleted reflecting a steep C-V curve. Exceeding threshold bias, the depletion regime is extending to high resistance GaN layer therefore capacitance is very small due to low electron concentration.

The measured C-V characteristics are further used to calculate the net sheet carrier concentration of 2DEG for GaN/AlN/AlInN heterostructures (see table 6.1). In figure 6.9 the carrier distribution profiles are plotted as a function of depletion depth using Eqs. 2.30 and 2.31, while the net carrier concentration of 2DEG (as mentioned in the graph) is estimated from the area under corresponding curves. With increasing SiN cap thickness the sheet carrier concentration decreases slightly (see Table 6.1), hence the initial drop in the capacitance value in accumulation regime upon SiN passivation can be attributed to the lower carrier concentration of 2DEG. The peak positions agree well with the total thickness of the SiN and AlInN barrier layers for each sample. The value of dielectric constant of SiN estimated from the zero-bias capacitance (using Eq. 2.30) is 7.2, close to the reported value. [152, 153]

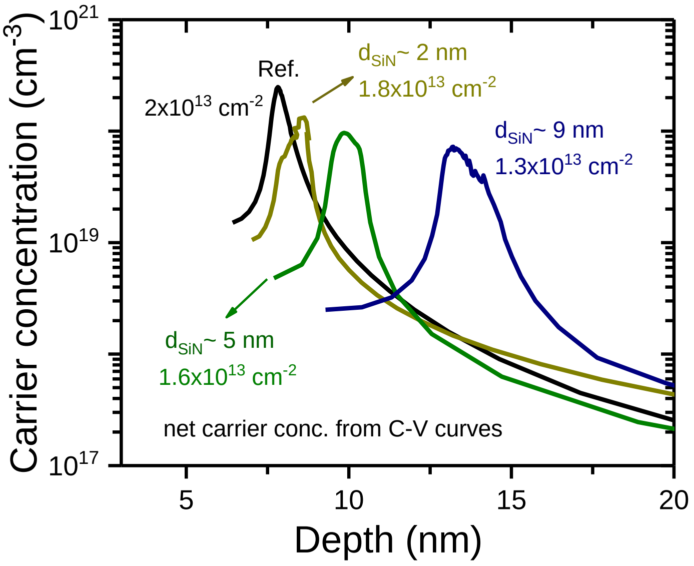

Figure 6.9: Carrier distribution profile as a function of depletion depth indicating net carrier concentration in the 2DEG as estimated from area under the curves.

To investigate the electrical behaviour of trap states in GaN/AlN/AlInN heterostructures, an equivalent circuit of MIS capacitor shown in fig. 2.12 is adopted where the trap states are assumed to be comprised of a continuum of levels.[89] These trap states can be located at the AlInN surface, at the AlInN/SiN or GaN/AlN/AlInN layer regions, also within the AlInN barrier or GaN buffer layer.[144, 154] The model employs the capacitance of an AlInN layer and a GaN depletion regime along with trap capacitance (C_{trap}) and associated loss mechanism (R_{trap}) during the capture/emission of carriers from the traps. The simplified equivalent circuit determines the parallel capacitance and conductance of the MIS structure.

Angular frequency (ω) dependent parallel conductance (G_p/ω) spectra explored for the sample #2 (2 nm SiN), at 295 K and at different reverse applied voltages are displayed in figure 6.10. The dynamic capacitance dispersion probes the AlInN/SiN and GaN/AlN/AlInN layer regions by changing the applied bias from accumulation (V_{bias} near zero) to depletion ($V_{bias} > V_{th}$). With change in depletion bias the dispersions in figure 6.10 signify two different behaviours. From zero to −1.4 V the bias dependent amplitudes of frequency dispersions represent the extension of the depletion width from AlInN/SiN region to full depletion of the 2DEG. At the resonance frequency, observed dispersion peaks are related to parallel resistance and parallel capacitance as $\omega_R=1/RC$, hence shift in the peak position at higher (lower) frequencies is associated to overall decrease (increase) in the RC product.

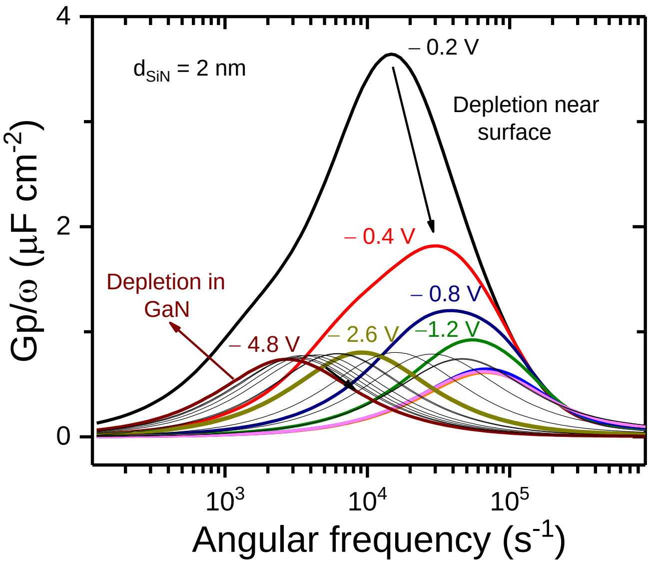

Figure 6.10: G_p/ω versus log(ω) plot for a sample with d_{SiN} = 2 nm measured at various reverse applied voltages.

In the accumulation regime, around zero bias, the barrier layer has a response time τ = RC due to maximum capacitance. With increasing depletion bias the total capacitance reduces and the dispersion shifts to the high frequency regime as presented in fig. 6.10. The amplitude of the dispersion peak also decreases up to –1.4 V (due to the extension of the depletion width C is reduced and R increased). Besides the main dispersion peak a second shoulder appears at lower frequency which represents another parallel capacitance. This can be associated to the undoped GaN/AlN section which is assumed to be depleted at higher reverse bias. With a further increase in reverse bias from –1.6 V to –5 V the depletion width of the metal contact reaches the undoped GaN layer. As a consequence high resistance of the GaN correspond to a shift towards the low frequency regime.

The parallel conductance curves of all samples recorded at reverse bias near 2DEG depletion, as a function of angular frequency are compared in figure 6.11. Values of applied voltages for corresponding curves are marked in the graph. It is seen, that the reference sample without passivation layer shows a strong G_p/ω dispersion peak indicating response time when the device is near 2DEG depletion. There is significant decrease in the amplitude of dispersion for the sample with 2 nm thick SiN passivation layer. Whereas sample #3 and #4 with thicker SiN layer (d_{SiN} ~ 5 nm and 9 nm) exhibit very weak and suppressed dispersions shifted at lower frequency. Following the parallel equivalent model circuit, these dispersions involve the resistances of barrier layer, AlN and GaN regions. As layer resistance grows with SiN thickness, the amplitude of peak in response curve decreases and the peak shifts to lower frequency. The broad and sharp G_p/ω peak found for the un-passivated reference sample is associated with a high conductance of the contact.

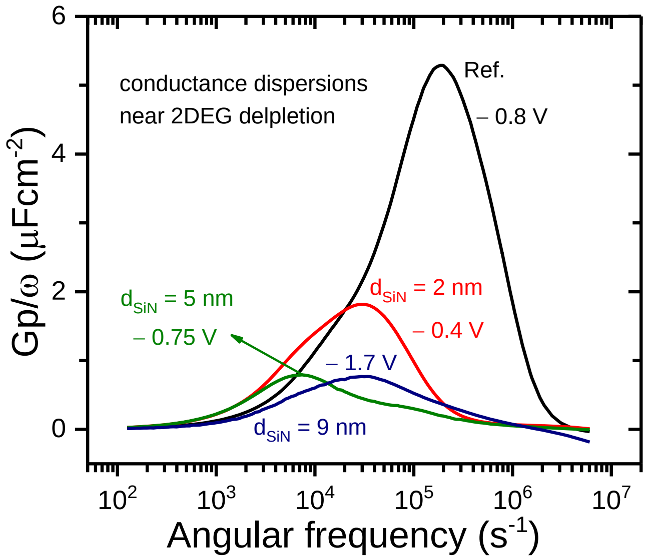

Figure 6.11: Parallel conductance of GaN/AlN/AlInN/SiN heterostructures as a function of angular frequency (ω) measured at 295 K and near 2DEG depletion regime.

6.6 Temperature dependence of C-V analysis

It is evident from figure 6.12 that parallel capacitance-voltage curves manifest dependence on the temperature. Here the C_p-V characteristics of sample with 5 nm passivation layer measured at 1 kHz frequency, with varying temperature from 50-400 K are portrayed.

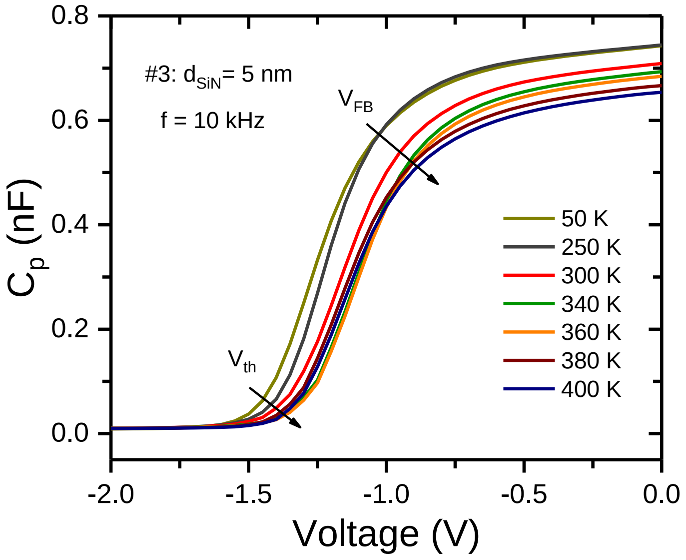

Figure 6.12: Reverse bias C-V curves in the temperature range of 50-400 K, at 10 kHz frequency, for sample with d_{SiN} = 5 nm.

In the range from 50-250 K, parallel capacitances of the device are more or less independent of temperature, however the measured capacitance in accumulation and 2DEG depletion regime exhibits a decreasing behaviour with rise in temperature from RT to 400 K. Flat band and threshold voltages are slightly shifted to the low negative bias with rising temperatures. These measurements are next used to estimate 2DEG carrier concentration at various temperatures. As can be seen from figure 6.13, the deduced carrier concentrations of all samples are not influenced at temperatures below 250 K whereas a reduction of the sheet carrier concentration is observed from 300 K to 400 K. Similar temperature dependent behaviour of carrier concentration in the range of 223 K - 398 K has been reported for AlGaN/GaN HEMTs.[155] This can be explained by thermally activated carrier trapping processes. However, carrier density of the sample with 9 nm thick passivation layer is more or less independent of temperature.

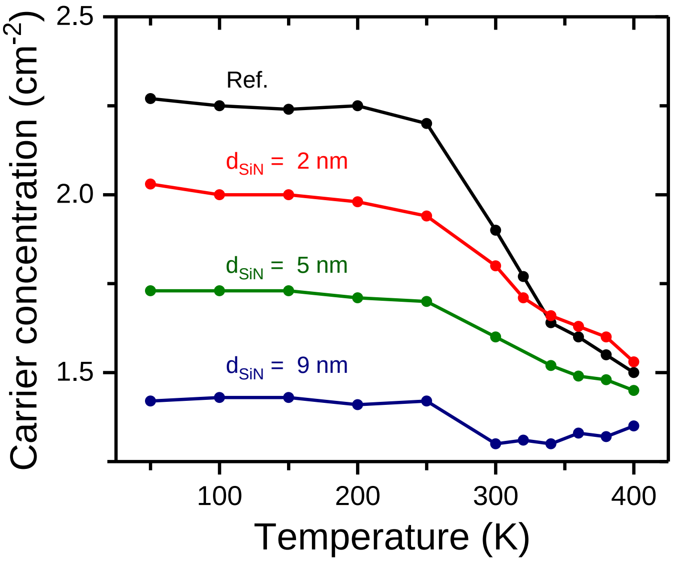

Figure 6.13: Temperature dependence of carrier concentration obtained from C-V analysis.

6.7 Investigation of trapping effects

In order to extract D_{trap} and τ_{trap} quantities the trap parameters are estimated by fitting experimental $G_p(\omega)$ or $C_p(\omega)$ data. The C-V curves measured for a sample with d_{SiN}~ 5 nm at multiple frequencies are shown in figure 6.14. A strong frequency dispersion of the C-V curves is observed from accumulation to depletion regime. In accumulation regime, the measured parallel capacitance is dominated by the contribution from 2DEG, whereas the capacitance dispersions in depletion regime are attributed to trap states within the band gap.

At 1 kHz and 10 kHz, ωτ < 1 hence most of the trap states are able to contribute to the observed capacitance while at higher frequency ωτ increases, and the probing depth becomes nearly zero (when ωτ≈1). Thus traps do not respond to the measured capacitance.

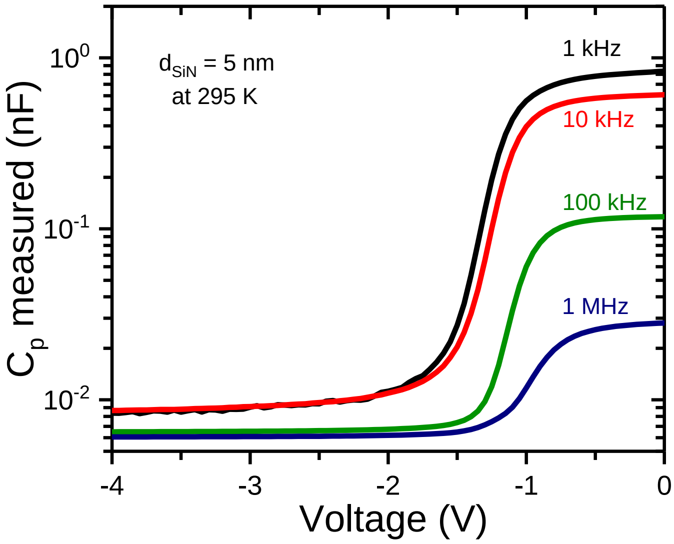

Figure 6.14: C-V characteristics of GaN/AlN/AlInN/SiN MIS diodes at multiple frequencies.

Typical G_p/ω versus ω curves measured at different reverse bias as shown in fig. 6.10 were fitted in accordance with Eq. 2.35 (fitting of the curves is not displayed) to determine trap parameters. Figure 6.15 plots the extracted values of deduced trap densities D_{trap} for all samples as a function of depletion bias. The trap density of the reference (un-passivated) sample in the 2DEG depletion regime is found to be above 10^{13} cm^{-2} eV^{-1} whereas for GaN/AlN/AlInN heterostructures with a passivation layer an apparent decrease in the values of D_{trap} can be seen. In GaN depletion regime D_{trap} is around (4-5)×10^{12} cm^{-2}eV^{-1} for sample with d_{SiN} = 9 nm. In previous reports D_{trap} was reported at slightly lower values for GaN/AlN/AlInN[144] heterostructure with a SiN passivation layer of thickness of 11.1 nm, and for a GaN/AlGaN/SiN[156] heterostructure with a 14 nm in-situ deposited SiN layer. The value for the un-passivated sample in depletion regime are comparable with literature,[89, 90, 144] where the state densities for GaN/AlN/AlInN and GaN/AlGaN heterostructures are reported in the range of (0.4-1.3)×10^{13} cm^{-2} eV^{-1}.

The second defect state parameter obtained from G_p/ω data for GaN/AlN/AlInN/SiN heterostructures is the emission time constant which depend on the space charge region width. Emission time constants τ_{trap} of reference and thin SiN layer occurs over a wide range from 1 μs - 0.3 ms whereas for GaN/AlN/AlInN heterostructures with thick SiN layers (5 nm and 9 nm) τ_{trap} are in the range of 0.1 ms - 3 ms.

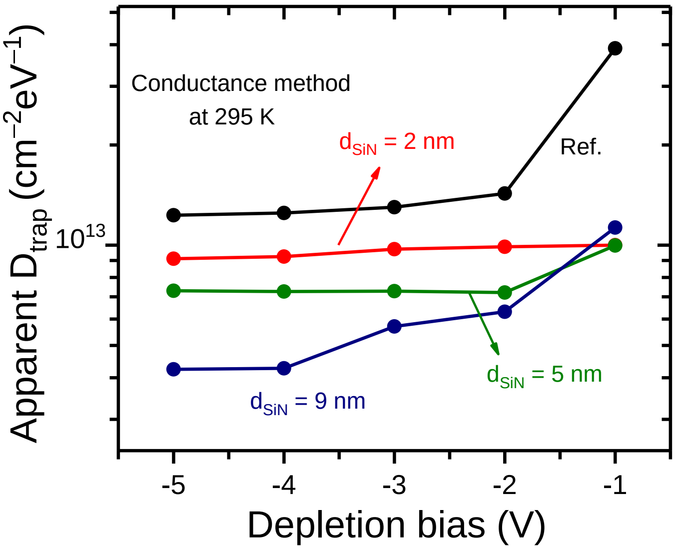

Figure 6.15: Apparent trap densities (D_{trap}) obtained by the conductance method

Conductance method was mainly derived to extract trap densities at high-permittivity **k** dielectric/semiconductor interfaces and their distribution in narrow semiconductor band gap materials like silicon. Typical wide gap material contains deep level traps that influence the response of frequency-based conductance and low-high frequency methods. Therefore, exact value of trap densities and location of the traps for GaN cannot be determined with these measurements.

Usually it is assumed that trap states within the AlInN and GaN layers typically exist deep below the conduction band edge and have slow transients with emission times as large as milliseconds.[144, 154] Stoklass et al.[89] have revealed an emission time of 8 ms for the defect states in the GaN bulk, while they have attributed time constants in the range of 0.1 - 1 μs to near-surface states in GaN/AlGaN HFETs and MOSHFETs structures. In another report[144] emission time constants of 3 - 7 μs are associated with near-surface states in GaN/AlN/AlInN heterostructures.

6.8 Defect characterization of GaN and GaN/AlN/AlInN structures

To investigate deep and shallow defect states in GaN/AlN/AlInN heterostructures in comparison to GaN buffer structures thermally stimulated current measurements were conducted. The measurement starts at low temperature by filling electron and hole traps through illuminating the sample for several minutes with above band gap light. Then filled traps were emptied in dark ambience at constant reverse bias by slowly increasing the temperature while recording sample current.[103]

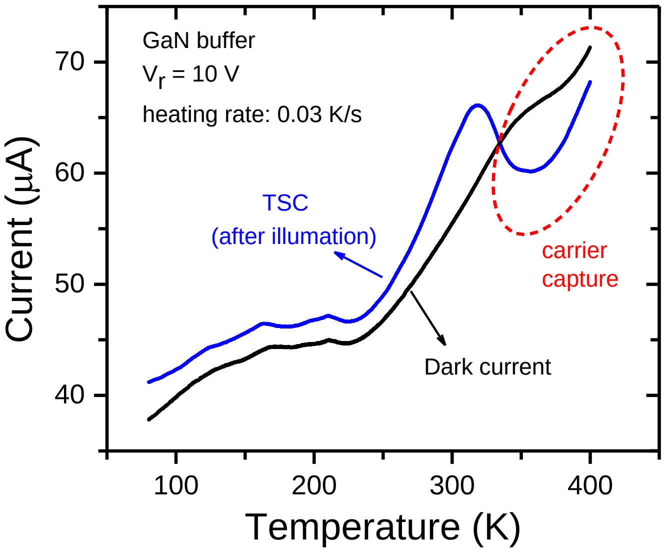

Figure 6.16: TSC spectrum of an undoped GaN buffer

Thermally stimulated current spectrum of GaN buffer layer sample is shown in figure 6.16, where black curve is intrinsic dark current while the blue curve represents the current obtained after illumination. The red dotted line in fig. 6.16 indicates a region of carrier loss. Net TSC currents are obtained by subtraction of the intrinsic dark current from the optically excited current.

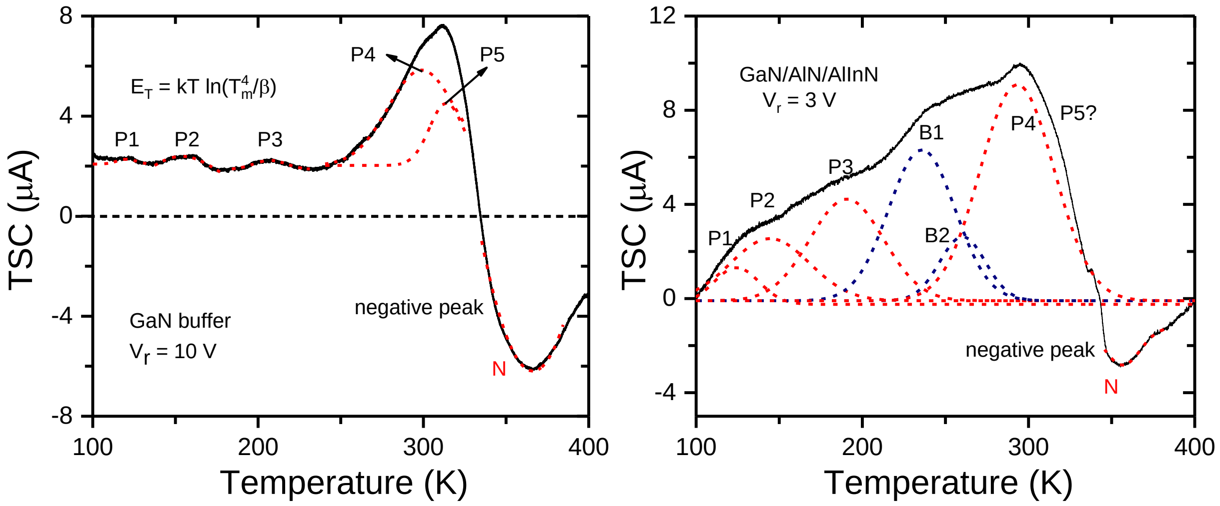

(a) (b)

Figure 6.17: Peak fittings on TSC spectra: (a) GaN buffer; and (b) GaN/AlN/AlInN sample

Typically, the excited spectrum shows higher currents than the intrinsic dark current since thermal emissions from traps take place. But, in the range from 300 - 400 K the excited current is lower than the intrinsic dark current which implies a carrier capture process caused by traps. Hence as illustrated in fig. 6.17 (a), a negative peak appears in the TSC spectra of the GaN buffer layer above 300 K after subtraction. A dashed reference line is drawn at zero difference signal. The negative peak is also observable in GaN/AlN/AlInN heterostructure as shown in fig. 6.17 (b).

In the GaN buffer structure, positive but weak TSC traps appear at P1 ~ 124 K, P2 ~ 144 K, P3 ~ 207 K, along with dominant peaks P4 ~ 299 K, P5 ~ 314 K, and a negative peak N ~ 366 K. GaN/AlN/AlInN heterostructure shows peaks P1-P3, P4, N, and may be P5 with nearly similar peak positions as in GaN buffer. Two additional peaks B1 ~ 236 K and B2 ~ 260 K can be identified. The activation energies (E_T) are estimated with $E_T = kT_m \ln(T_m^4/\beta)$, where T_m is the peak temperature, β is the heating rate, and k is the Boltzmann constant.[103, 102]

Table 6.3: Overview of activation energies of defects in GaN/AlN/AlInN and GaN samples

This work			Fang et al. [102]	Fang et al. [157]	Yang et al. [158]
Peak position	GaN (eV)	GaN/AlN/AlGaN (eV)			
P1	0.24±0.02	0.23±0.02		D: 0.25 eV	
P2	0.30±0.02	0.31±0.02			
P3	0.44±0.02	0.40±0.02			
B1		0.51±0.04			0.54 eV
B2		0.57±0.03	B: 0.58 eV	B: 0.61 eV	
P4	0.67±0.04	0.66±0.04	A: 0.67 eV		0.65 eV
P5	0.71±0.05	0.75±0.05		A_x: 0.72 eV	0.75 eV
N	0.85±0.04	0.83±0.04			

Individual peak fits and activation energies for the GaN buffer and GaN/AlN/AlInN samples are also displayed in figs. 6.17 (a) and (b), respectively. Fang et al.[102, 157] reported similar activation energies in n-type and C-doped semi-insulating GaN layers by deep level transient spectroscopy and TSC. Three GaN buffer related deep-level traps with activation energies of 0.54 eV, 0.65 eV and 0.75 eV are reported in GaN/AlGaN structure by TSC measurement.[158] Table 6.3 presents an overview of trap activation energies in our work in comparison with previous work. The negative peaks found in both spectra suggest carrier capture processes above 300 K which might be responsible for increase in resistance at high temperatures. From our TSC measurements on GaN/AlN/AlInN and GaN buffer structures, we have determined similar values of trap activation energies.

6.9 Conclusion

In this chapter, the influence of a SiN passivation on electrical properties of GaN/AlN/AlInN heterostructures was studied. After the insertion of ≥ 5 nm thick SiN on AlInN barrier layer surface leakage currents are substantially alleviated due to increase in barrier height and series resistance. Also a reduction of the capacitance in accumulation regime and a shift of the flat band voltages is observed as a function of SiN thickness.

The current transport through the Schottky contacts on GaN/AlN/AlInN/SiN heterostructures in forward direction can be explained by trap assisted tunneling processes while the reverse-bias leakage currents are dominated by Frenkel-Poole emission. By employing a thick SiN capping layer, the charge transfer probability is significantly reduced due to an enhanced emission barrier height for the trap states that characterizes the conduction mechanism.

There is a reduction in sheet carrier concentration with increasing temperature above 250 K, which can be attributed carrier trapping processes at elevated temperatures. Thermally stimulated current measurements on GaN/AlN/AlInN and GaN buffer structures also indicate carrier capture or loss mechanisms above room temperature.

Chapter 7

Summary and outlook

The aim of this study was to present a direct comparison of the material properties of two common deep acceptor dopants carbon and iron for semi-insulating GaN layers and FET structures. The thesis consists of two main experimental parts. Firstly, an investigation of the surface and local electronic behaviour of MOVPE grown semi-insulating GaN buffer layers, by adopting various electrical, optical and scanning probe microscopy techniques. Secondly, GaN/AlN/AlInN and GaN/AlGaN heterostructures were characterized with a focus to study the influence of the semi-insulating GaN buffer layer and SiN surface passivation layers on the electrical properties of device structures.

Precursor based C-doped and Fe-doped GaN layers were compared with regard to their breakdown field strength, leakage currents and surface potential distributions on the micro and nanoscale. By investigating the contact potential using EFM technique, the influence of carbon or iron doping on Fermi-level position was determined. With the references of n-type and p-type GaN samples, the acceptor states introduced by carbon were demonstrated to cause Fermi-level pinning below the midgap position at C doping levels above $1.6\text{x}10^{18}$ cm^{-3} whereas the acceptor-states by Fe impurities were always energetically located above the midgap position.

By locally probing dislocations using SSPM a negative charge contrast with respect to the surrounding areas was revealed in C-doped samples which enhanced with increasing doping concentration, whereas Fe-doped samples do not exhibit such a contrast. This negative charge contrast around dislocations observed in carbon doped GaN samples can be associated with an energetic barrier for electrons trapped at dislocations suggesting higher activation energy for the measured leakage currents in GaN:C samples as compared to Fe-doped GaN. Vertical transport measurements establish the high potential of extrinsically C-doped GaN layers in favor to Fe-doped layers. For an acceptor concentration of $4.6\text{x}10^{18}$ cm^{-3} GaN:C sample exhibit an up to 5 orders of magnitude lower dark current at room temperature and significantly higher thermal activation energy than Fe-doped sample with a comparable dopant concentration. In the C- and Fe-doped GaN layers activation energies of 0.6 eV and 0.21 eV were found, respectively, which are substantially lower than to be expected for a release of electrons from $C_N^{0/-}$ and $Fe^{+3/+2}$ defect levels. However, vertical transport via threading dislocations can be considered to be responsible for low activation energies allowing current flow through the undoped GaN layer and the Si-doped buffer region.

Surface and electrical properties of extrinsically GaN:C layers doped using propane as precursor source were compared with intrinsically carbon doped layers where carbon doping was achieved by lowering growth temperature and V/III ratio. It was observed that the surface morphology for intrinsic doping degrades with lowering growth temperature and breakdown occurs at lower electric field. These investigations indicate that GaN:C sample doped using a precursor shows better properties than intrinsic doping.

GaN/AlN/AlInN and GaN/AlGaN FETs with carbon and iron doped buffer structures were analyzed using buffer (lateral) leakage and vertical current leakage measurements on test devices. C-doped AlInN and AlGaN FETs offer electric field strength as high as 2.6×10^6 V/cm for lateral buffer leakage and above 2.4×10^6 V/cm for vertical contact arrangement. In contrast, the Fe-doped FETs enhance the breakdown field strength up to 1.5×10^6 V/cm in lateral configuration and 1.9×10^6 V/cm for vertical leakage measurements through the device. The comparison of carbon and iron doped buffer FETs demonstrate that carbon doping is more effective in achieving low buffer and vertical leakage currents, high breakdown voltages, and improve the electric field strengths. Transfer characteristics of GaN/AlN/AlInN FET device structures suggest that both Fe- and C-doped GaN buffer structures substantially reduce gate leakage and off-state leakage currents. While a shift in V_{th} to a higher reverse bias were found for an overall increase in buffer doping level, both C and Fe doped buffer FETs established that 2DEG properties are not deteriorated upon semi-insulating doping and buffer doping was also not found to change the defect density distributions.

The effectiveness of an in-situ deposited SiN passivation layer on electrical properties of GaN/AlN/AlInN heterostructures was also demonstrated. A marginal decrease in the 2DEG density found for thicker SiN capping layers is attributed to a relocation of the net surface charge away from the 2DEG. A systematic shift in flat band voltages with a decrease in zero bias capacitance as a function of passivation layer thickness was seen which can be associated to an increase in the series resistance of device. Reverse leakage currents in GaN/AlN/AlInN heterostructures were mitigated substantially with SiN layer, also the Schottky barrier height is enhanced from 0.58 eV to 0.81 eV. Generally, in forward direction trap assisted tunneling mechanism was found to be responsible for current transport, while the reverse-bias leakage current was dominated by Frenkel-Poole emission. Polarization induced fixed charges enhance the probability of electron tunneling through the Schottky gate barrier for uncapped sample whereas by inserting a SiN cap layer the tunneling probability can be reduced due to an increases barrier height, thereby increasing the device performance.

Although different electrical properties of the GaN-based AlInN and AlGaN FETs have been investigated in this work, details of the drain-current transient effects and the degradation mechanisms should be studied in the future. By conducting pulsed measurements with a broad range of the pulse width, bias level and temperature could deliver significant information regarding drain current transient effects. These measurements will probe channel trapping and deep buffer traps under ON-state device operating conditions. The existence of current collapse and related dispersion effects can be analyzed by employing gate-lag and drain-lag turn-on pulsing techniques. Next to DC properties of the FETs, RF characterization should be done to study about the device performance in the high frequency range. High frequency analysis of the FET devices could be obtained by the measurement and evaluation of scattering parameters (S-parameters).

Bibliography

[1]O. Ambacher, J. Phys. D: Appl. Phys. **31**, 2653 (1998).

[2]M. A. Khan, X. Hu, G. Sumin, A. Lunev, J. Yang, R. Gaska, and M. S. Shur, IEEE Electron Device Lett. **21**, 63 (2000).

[3]A. Krost and A. Dadgar, Materials Science and Engineering: B **93**, 77 (2002).

[4]O. Ambacher, B. Foutz, J. Smart, J. R. Shealy, N. G. Weimann, K. Chu, M. Murphy, A. J. Sierakowski, W. J. Schaff, L. F. Eastman, R. Dimitrov, A. Mitchell, and M. Stutzmann, Journal of Applied Physics **87**, 334 (2000).

[5]Y. Dora, A. Chakraborty, L. Mccarthy, S. Keller, S. P. DenBaars, and U. K. Mishra, IEEE Electron Device Lett. **27**, 713 (2006).

[6]U. K. Mishra, P. Parikh, and Y. -F. Wu, Proc. IEEE **90**, 1022 (2002).

[7]U. K. Mishra, S. Likun, T. E. Kazior, and Y. -F. Wu, Proc. IEEE **96**, 287 (2008).

[8]F. A. Marino, D. A. Cullen, D. J. Smith, M. R. McCartney, and M. Saraniti, Journal of Applied Physics **107**, 54516 (2010).

[9]C. D. Lee, V. Ramachandran, A. Sagar, R. M. Feenstra, D. W. Greve, W. L. Sarney, L. S. Riba, D. C. Look, S. Bai, W. J. Choyke, and R. P. Devaty, Journal of Electronic Materials **30**, 162 (2001).

[10]S. Q. Zhou, A. Vantomme, B. S. Zhang, H. Yang, and M. F. Wu, Appl. Phys. Lett. **86**, 81912 (2005).

[11]D. Kapolnek, X. H. Wu, B. Heying, S. Keller, B. P. Keller, U. K. Mishra, S. P. DenBaars, and J. S. Speck, Appl. Phys. Lett. **67**, 1541 (1995).

[12]S. Keller, B. P. Keller, Y. -F. Wu, B. Heying, D. Kapolnek, J. S. Speck, U. K. Mishra, and S. P. DenBaars, Appl. Phys. Lett. **68**, 1525 (1996).

[13]T. Hino, S. Tomiya, T. Miyajima, K. Yanashima, S. Hashimoto, and M. Ikeda, Appl. Phys. Lett. **76**, 3421 (2000).

[14]V. Narayanan, K. Lorenz, W. Kim, and S. Mahajan, Appl. Phys. Lett. **78**, 1544 (2001).

[15]Q. Dai, M. F. Schubert, M. H. Kim, J. K. Kim, E. F. Schubert, D. D. Koleske, M. H. Crawford, S. R. Lee, A. J. Fischer, G. Thaler, and M. A. Banas, Appl. Phys. Lett. **94**, 111109 (2009).

[16]G. Steude, B. K. Meyer, A. Göldner, A. Hoffmann, A. Kaschner, F. Bechstedt, H. Amano, and I. Akasaki, Jpn. J. Appl. Phys. **38**, L498-L500 (1999).

[17]J. Neugebauer and C. G. van de Walle, Phys. Rev. B **50**, 8067 (1994).

[18]M. J. Uren, J. Moreke, and M. Kuball, IEEE Trans. Electron Devices **59**, 3327 (2012).

[19]S. Heikman, S. Keller, S. P. DenBaars, and U. K. Mishra, Appl. Phys. Lett. **81**, 439 (2002).

[20]D. D. Koleske, A. E. Wickenden, R. L. Henry, and M. E. Twigg, Journal of Crystal Growth **242**, 55 (2002).

[21]W. V. Lundin, E. E. Zavarin, P. N. Brunkov, M. A. Yagovkina, A. V. Sakharov, M. A. Sinitsyn, B. Y. Ber, D. Y. Kazantsev, and A. F. Tsatsulnikov, Tech. Phys. Lett. **42**, 539 (2016).

[22]C. H. Seager, A. F. Wright, J. Yu, and W. Götz, Journal of Applied Physics **92**, 6553 (2002).

[23]C. Poblenz, P. Waltereit, S. Rajan, S. Heikman, U. K. Mishra, and J. S. Speck, J. Vac. Sci. Technol. B **22**, 1145 (2004).

[24]M. J. Uren, S. Karboyan, I. Chatterjee, A. Pooth, P. Moens, A. Banerjee, and M. Kuball, IEEE Trans. Electron Devices **64**, 2826 (2017).

[25]A. -J. Tzou, D. -H. Hsieh, S. -H. Chen, Y. -K. Liao, Z. -Y. Li, C. -Y. Chang, and H. -C. Kuo, Electronics **5**, 28 (2016).

[26]Y. Pu, L. Pang, X. -J. Chen, T. -T. Yuan, W. -J. Luo, and X. -Y. Liu, Chinese Phys. B **20**, 97305 (2011).

[27]M. Meneghini, A. Tajalli, P. Moens, A. Banerjee, E. Zanoni, and G. Meneghesso, Materials Science in Semiconductor Processing **78**, 118 (2018).

[28]B. M. Green, K. K. Chu, E. M. Chumbes, J. A. Smart, J. R. Shealy, and L. F. Eastman, IEEE Electron Device Lett. **21**, 268 (2000).

[29]R. Vetury, N. Q. Zhang, S. Keller, and U. K. Mishra, IEEE Trans. Electron Devices **48**, 560 (2001).

[30]N. Ramanan, B. Lee, C. Kirkpatrick, R. Suri, and V. Misra, Semicond. Sci. Technol. **28**, 74004 (2013).

[31]A. D. Koehler, N. Nepal, T. J. Anderson, M. J. Tadjer, K. D. Hobart, C. R. Eddy, and F. J. Kub, IEEE Electron Device Lett. **34**, 1115 (2013).

[32]G. Koley and M. G. Spencer, Appl. Phys. Lett. **78**, 2873 (2001).

[33]P. J. Hansen, Y. E. Strausser, A. N. Erickson, E. J. Tarsa, P. Kozodoy, E. G. Brazel, J. P. Ibbetson, U. Mishra, V. Narayanamurti, S. P. DenBaars, and J. S. Speck, Appl. Phys. Lett. **72**, 2247 (1998).

[34]A. Krtschil, A. Dadgar, and A. Krost, Journal of Crystal Growth **248**, 542 (2003).

[35]S. Barbet, R. Aubry, M. -A. Di Forte-Poisson, J. -C. Jacquet, D. Deresmes, T. Mélin, and D. Théron, Appl. Phys. Lett. **93**, 212107 (2008).

[36]B. S. Simpkins, E. T. Yu, U. Chowdhury, M. M. Wong, T. G. Zhu, D. W. Yoo, and R. D. Dupuis, Journal of Applied Physics **95**, 6225 (2004).

[37]Y. Zhang, D. Piedra, M. Sun, J. Hennig, A. Dadgar, L. Yu, and T. Palacios, IEEE Electron Device Lett. **38**, 248 (2017).

[38]H. Morkoç, Handbook of nitride semiconductors and devices, Wiley-VCH; Chichester: John Wiley, Weinheim, (2008-2009).

[39]I. A. Luk'yanchuk and D. Mezzane, Smart materials for energy, communications and security, Springer, Dordrecht, (2008).

[40]T. Hanada, in Oxide and Nitride Semiconductors, edited by M. Hasegawa, A. Inoue, N. Kobayashi, T. Sakurai, L. Wille, T. Yao, and S. -K. Hong, Springer Berlin Heidelberg, Berlin, Heidelberg, pp. 1-19, (2009).

[41]H. Morkoç, Materials Science and Engineering: R: Reports **33**, 135 (2001).

[42]E. J. Miller, D. M. Schaadt, E. T. Yu, C. Poblenz, C. Elsass, and J. S. Speck, J. Appl. Phys. **91**, 9821 (2002).

[43]Y. Y. Wong, E. Y. Chang, T. -H. Yang, J. -R. Chang, J. -T. Ku, M. K. Hudait, W. -C. Chou, M. Chen, and K. -L. Lin, J. Electrochem. Soc. **157**, H746 (2010).

[44]M. A. Meyers and K. K. Chawla, Mechanical behavior of materials Cambridge University Press, Cambridge, (2009).

[45]H. M. Ng, D. Doppalapudi, T. D. Moustakas, N. G. Weimann, and L. F. Eastman, Appl. Phys. Lett. **73**, 821 (1998).

[46]W. Götz, N. M. Johnson, C. Chen, H. Liu, C. Kuo, and W. Imler, Appl. Phys. Lett. **68**, 3144 (1996).

[47]K. K. Chin, J. Semicond. **32**, 112001 (2011).

[48]A. Y. Polyakov and I. -H. Lee, Materials Science and Engineering: R: Reports **94**, 1 (2015).

[49]G. Miceli and A. Pasquarello, Phys. Rev. B **93** (2016).

[50]A. Lesnik, M. P. Hoffmann, A. Fariza, J. Bläsing, H. Witte, P. Veit, F. Hörich, C. Berger, J. Hennig, A. Dadgar, and A. Strittmatter, phys. stat. sol. (b) **254**, 1600708 (2017).

[51]K. Ikenaga, A. Mishima, Y. Yano, T. Tabuchi, and K. Matsumoto, Jpn. J. Appl. Phys. **55**, 05FE04 (2016).

[52]W. Siegel, G. Kühnel, H. A. Schneider, H. Witte, and T. Flade, Journal of Applied Physics **69**, 2245 (1991).

[53]T. Tanaka, N. Kaneda, T. Mishima, Y. Kihara, T. Aoki, and K. Shiojima, Jpn. J. Appl. Phys. **54**, 41002 (2015).

[54]T. Y. Lin, W. S. Su, and Y. F. Chen, Solid State Communications **130**, 49 (2004).

[55]M. Kocan, A. Rizzi, H. Lth, S. Keller, and U. K. Mishra, phys. stat. sol. (b) **234**, 773 (2002).

[56]K. Köhler, J. Wiegert, H. P. Menner, M. Maier, and L. Kirste, Journal of Applied Physics **103**, 23706 (2008).

[57]O. Ambacher, J. Majewski, C. Miskys, A. Link, M. Hermann, M. Eickhoff, M. Stutzmann, F. Bernardini, V. Fiorentini, V. Tilak, B. Schaff, and L. F. Eastman, J. Phys.: Condens. Matter **14**, 3399 (2002).

[58]X. -G. He, D. -G. Zhao, and D. -S. Jiang, Chinese Phys. B **24**, 67301 (2015).

[59]B. J. Rodriguez, W. -C. Yang, R. J. Nemanich, and A. Gruverman, Appl. Phys. Lett. **86**, 112115 (2005).

[60]P. M. Bridger, Z. Z. Bandić, E. C. Piquette, and T. C. McGill, Appl. Phys. Lett. **74**, 3522 (1999).

[61]M. S. Tyagi, in Metal-Semiconductor Schottky Barrier Junctions and Their Applications, edited by B. L. Sharma, Springer US, Boston, MA, pp. 1–60, (1984).

[62]E. T. Yu, X. Z. Dang, P. M. Asbeck, S. S. Lau, and G. J. Sullivan, J. Vac. Sci. Technol. B **17**, 1742 (1999).

[63]O. Ambacher, J. Smart, J. R. Shealy, N. G. Weimann, K. Chu, M. Murphy, W. J. Schaff, L. F. Eastman, R. Dimitrov, L. Wittmer, M. Stutzmann, W. Rieger, and J. Hilsenbeck, Journal of Applied Physics **85**, 3222 (1999).

[64]F. Bernardini, V. Fiorentini, and D. Vanderbilt, Phys. Rev. B **56**, R10024-R10027 (1997).

[65]J. Piprek, Nitride semiconductor devices: Principles and simulation, edited by Joachim Piprek, Wiley-VCH; Chichester: John Wiley, Weinheim, (2007).

[66]M. A. Khan, J. N. Kuznia, J. M. van Hove, N. Pan, and J. Carter, Appl. Phys. Lett. **60**, 3027 (1992).

[67]D. A. Neamen, Semiconductor physics and devices: Basic principles, McGraw-Hill, New York NY, (2012).

[68]E. T. Yu, G. J. Sullivan, P. M. Asbeck, C. D. Wang, D. Qiao, and S. S. Lau, Appl. Phys. Lett. **71**, 2794 (1997).

[69]M. Gassoumi, A. Helali, M. Gassoumi, C. Gaquiere, and H. Maaref **13**, 211 (2017).

[70]C. Zhou, Q. Jiang, S. Huang, and K.J. Chen, IEEE Electron Device Lett. **33**, 1132 (2012).

[71]B. Lu, E. L. Piner, and T. Palacios, in 68th Device Research Conference, Notre Dame, IN, USA, 21/06/2010 - 23/06/2010, IEEE, pp. 193-194, (2010).

[72]W. D. Callister and D. G. Rethwisch, Materials science and engineering: An introduction, Wiley, Hoboken NJ, (2014).

[73]J. L. Lyons, A. Janotti, and C. G. van de Walle, Appl. Phys. Lett. **97**, 152108 (2010).

[74]J. L. Lyons, A. Janotti, and C. G. van de Walle, Phys. Rev. B **89**, G3 (2014).

[75]Y. K. Noh, S. T. Lee, M. D. Kim, and J. E. Oh, Journal of Crystal Growth **460**, 37 (2017).

[76]K. Laaksonen, M. G. Ganchenkova, and R. M. Nieminen, J. Phys.: Condens. Matter **21**, 15803 (2009).

[77]E. Arslan, S. Bütün, Y. Şafak, H. Çakmak, H. Yu, and E. Özbay, Microelectronics Reliability **51**, 576 (2011).

[78]D. Yan, J. Jiao, J. Ren, G. Yang, and X. Gu, Journal of Applied Physics **114**, 144511 (2013).

[79]E. Arslan, S. Altındal, S. Özçelik, and E. Ozbay, Semicond. Sci. Technol. **24**, 75003 (2009).

[80]S. K. Cheung and N. W. Cheung, Appl. Phys. Lett. **49**, 85 (1986).

[81]E. Arslan, S. Bütün, Y. Safak, H. Uslu, İ. Taşçıoğlu, S. Altındal, and E. Özbay, Microelectronics Reliability **51**, 370 (2011).

[82]G. Dutta, N. DasGupta, and A. DasGupta, IEEE Trans. Electron Devices, 1 (2017).

[83]S. Ganguly, A. Konar, Z. Hu, H. Xing, and D. Jena, Appl. Phys. Lett. **101**, 253519 (2012).

[84]L. Lugani, M. A. Py, J. -F. Carlin, and N. Grandjean, Journal of Applied Physics **115**, 74506 (2014).

[85]O. Mitrofanov and M. Manfra, Journal of Applied Physics **95**, 6414 (2004).

[86]E. Arslan, S. Bütün, and E. Ozbay, Appl. Phys. Lett. **94**, 142106 (2009).

[87]D. K. Schroder, Semiconductor material and device characterization, Wiley Interscience, New York, Chichester, (2006).

[88]W. L. Liu, Y. L. Chen, A. A. Balandin, and K. L. Wang, Journal of Nanoelectronics and Optoelectronics **1**, 258 (2006).

[89]R. Stoklas, D. Gregušová, J. Novák, A. Vescan, and P. Kordoš, Appl. Phys. Lett. **93**, 124103 (2008).

[90]E. J. Miller, X. Z. Dang, H. H. Wieder, P. M. Asbeck, E. T. Yu, G. J. Sullivan, and J. M. Redwing, Journal of Applied Physics **87**, 8070 (2000).

[91]V. Ratnikov, R. Kyutt, T. Shubina, T. Paskova, E. Valcheva, and B. Monemar, Journal of Applied Physics **88**, 6252 (2000).

[92]N. V. Safriuk, Semicond. Phys. Quantum Electron. Optoelectron. **16**, 265 (2013).

[93]B. Liu, R. Zhang, Z. L. Xie, H. Lu, Q. J. Liu, Z. Zhang, Y. Li, X.Q. Xiu, P. Chen, P. Han, S. L. Gu, Y. Shi, Y. D. Zheng, and W. J. Schaff, Journal of Applied Physics **103**, 23504 (2008).

[94]M. Frentrup, L. Y. Lee, S. -L. Sahonta, M. J. Kappers, F. Massabuau, P. Gupta, R. A. Oliver, C. J. Humphreys, and D. J. Wallis, J. Phys. D: Appl. Phys. **50**, 433002 (2017).

[95]K. Inaba, S. Kobayashi, K. Uehara, A. Okada, S.L. Reddy, and T. Endo, AMPC **03**, 72 (2013).

[96]S. Kalinin and A. Gruverman, Scanning probe microscopy: Electrical and electromechanical phenomena at the nanoscale, edited by Sergei Kalinin, Alexei Gruverman, Springer, New York, (2007).

[97]B. Bhushan, Scanning Probe Microscopy in Nanoscience and Nanotechnology, Springer Berlin Heidelberg, Berlin, Heidelberg, (2010).

[98]B. S. Simpkins, D. M. Schaadt, E. T. Yu, and R. J. Molnar, J. Appl. Phys. **91**, 9924 (2002).

[99]W. Melitz, J. Shen, A. C. Kummel, and S. Lee, Surface Science Reports **66**, 1 (2011).

[100]F. Werner, Journal of Applied Physics **122**, 135306 (2017).

[101]T. Matsumura and Y. Sato, JMP **01**, 340 (2010).

[102]Z. -Q. Fang, D. C. Look, B. Claflin, S. Haffouz, H. Tang, and J. Webb, phys. stat. sol. (c) **2**, 2757 (2005).

[103]D. C. Look, Z. -Q. Fang, W. Kim, Ö. Aktas, A. Botchkarev, A. Salvador, and H. Morkoç, Appl. Phys. Lett. **68**, 3775 (1996).

[104]D. K. Schroder, Semiconductor material and device characterization, Wiley Interscience, New York, Chichester, (2006).

[105]M. A. Reshchikov and H. Morkoç, Journal of Applied Physics **97**, 61301 (2005).

[106]M. A. Reshchikov, D. O. Demchenko, A. Usikov, H. Helava, and Y. Makarov, Phys. Rev. B **90**, 97 (2014).

[107]B. Monemar, S. Khromov, G. Pozina, P. Paskov, P. Bergman, C. Hemmingsson, L. Hultman, H. Amano, V. Avrutin, X. Li, and H. Morkoç, Jpn. J. Appl. Phys. **52**, 08JJ03 (2013).

[108]S. Wang, D. Mao, Z. Jin, S. Peng, D. Zhang, J. Shi, and X. Wang, Nanotechnology **26**, 405706 (2015).

[109]X. -F. Zhang, L. Wang, J. Liu, L. Wei, and J. Xu, Chinese Phys. B **22**, 17202 (2013).

[110]D. K. Kim, J Mater Sci: Mater Electron **19**, 471 (2008).

[111]L. Zhang, Y. Shao, Y. Wu, X. Hao, X. Chen, S. Qu, and X. Xu, Journal of Alloys and Compounds **504**, 186 (2010).

[112]Y. Zhang, Z. Xing, Z. Ma, Y. Chen, G. Ding, P. Xu, C. Dong, H. Chen, and X. Le, Sci. China Phys. Mech. Astron. **53**, 465 (2010).

[113]V. S. Kopp, V. M. Kaganer, M. V. Baidakova, W. V. Lundin, A. E. Nikolaev, E. V. Verkhovtceva, M. A. Yagovkina, and N. Cherkashin, J. Appl. Phys. **115**, 73507 (2014).

[114]C. Romanitan, R. Gavrila, and M. Danila, Materials Science in Semiconductor Processing **57**, 32 (2017).

[115]L. Lu, Z. Y. Gao, B. Shen, F. J. Xu, S. Huang, Z. L. Miao, Y. Hao, Z. J. Yang, G. Y. Zhang, X. P. Zhang, J. Xu, and D. P. Yu, Journal of Applied Physics **104**, 123525 (2008).

[116]A. Krtschil, A. Dadgar, and A. Krost, Appl. Phys. Lett. **82**, 2263 (2003).

[117]A. Chakraborty, K. C. Kim, F. Wu, J. S. Speck, S. P. DenBaars, and U.K. Mishra, Appl. Phys. Lett. **89**, 41903 (2006).

[118]H. Witte, M. Wieneke, A. Rohrbeck, K. -M. Guenther, A. Dadgar, and A. Krost, J. Phys. D: Appl. Phys. **44**, 85102 (2011).

[119]A. Fariza, A. Lesnik, S. Neugebauer, M. Wieneke, J. Hennig, J. Bläsing, H. Witte, A. Dadgar, and A. Strittmatter, Journal of Applied Physics **122**, 25704 (2017).

[120]G. Callsen, M. R. Wagner, T. Kure, J. S. Reparaz, M. Bügler, J. Brunnmeier, C. Nenstiel, A. Hoffmann, M. Hoffmann, J. Tweedie, Z. Bryan, S. Aygun, R. Kirste, R. Collazo, and Z. Sitar, Phys. Rev. B **86**, G3 (2012).

[121]B. Monemar, P. P. Paskov, J. P. Bergman, A. A. Toropov, T. V. Shubina, S. Figge, T. Paskova, D. Hommel, A. Usui, M. Iwaya, S. Kamiyama, H. Amano, and I. Akasaki, Materials Science in Semiconductor Processing **9**, 168 (2006).

[122]R. Armitage, Q. Yang, and E. R. Weber, Journal of Applied Physics **97**, 73524 (2005).

[123]M. Kubota, T. Onuma, Y. Ishihara, A. Usui, A. Uedono, and S. F. Chichibu, J. Appl. Phys. **105**, 83542 (2009).

[124]N. Killat, M. J. Uren, D. J. Wallis, T. Martin, and M. Kuball, Appl. Phys. Lett. **101**, 153505 (2012).

[125]M. Azize, M. Leroux, M. Laugt, P. Gibart, and Z. Bougrioua, phys. stat. sol. (a) **203**, 1744 (2006).

[126]J. A. Freitas, M. Gowda, J. G. Tischler, J. -H. Kim, L. Liu, and D. Hanser, Journal of Crystal Growth **310**, 3968 (2008).

[127]S. Chevtchenko, X. Ni, Q. Fan, A. A. Baski, and H. Morkoç, Appl. Phys. Lett. **88**, 122104 (2006).

[128]S. Halas and T. Durakiewicz, J. Phys.: Condens. Matter **10**, 10815 (1998).

[129]G. Koley and M. G. Spencer, Journal of Applied Physics **90**, 337 (2001).

[130] T. E. Cook, C. C. Fulton, W. J. Mecouch, K. M. Tracy, R. F. DavisE. H. Hurt, G. Lucovsky, and R. J. Nemanich, Journal of Applied Physics **93,** 3995 (2003).

[131] D. Cherns, C. G. Jiao, H. Mokhtari, J. Cai, and F. A. Ponce, phys. stat. sol. (b) **234**, 924 (2002).

[132] G. Verzellesi, L. Morassi, G. Meneghesso, M. Meneghini, E. Zanoni, G. Pozzovivo, S. Lavanga, T. Detzel, O. Haberlen, and G. Curatola, IEEE Electron Device Lett. **35**, 443 (2014).

[133] M. J. Uren, M. Caesar, S. Karboyan, P. Moens, P. Vanmeerbeek, and M. Kuball, IEEE Electron Device Lett. **36**, 826 (2015).

[134] M. Rudziński, V. Desmaris, P. A. van Hal, J. L. Weyher, P.R. Hageman, K. Dynefors, T. C. Rödle, H. F. F. Jos, H. Zirath, and P. K. Larsen, phys. stat. sol. (c) **3**, 2231 (2006).

[135] J. Cai and F. A. Ponce, phys. stat. sol. (a) **192**, 407 (2002).

[136] H. Choi, E. K. Koh, Y. M. Cho, J. Jin, D. Byun, and M. Yoon, Microelectronics Journal **36**, 25 (2005).

[137] X. Li, Ö. Danielsson, H. Pedersen, E. Janzén, and U. Forsberg, Journal of Vacuum Science and Technology B, Nanotechnology and Microelectronics: Materials, Processing, Measurement, and Phenomena **33**, 21208 (2015).

[138] G. Malegori and G. Ferrini, Wavelet Transforms in Dynamic Atomic Force Spectroscopy INTECH Open Access Publisher, (2012).

[139] M. Wosko, B. Paszkiewicz, R. Paszkiewicz, and M. Tlaczala, Optica Applicata **43** (2013).

[140] S. Gustafsson, J. -T. Chen, J. Bergsten, U. Forsberg, M. Thorsell, E. Janzen, and N. Rorsman, IEEE Trans. Electron Devices **62**, 2162 (2015).

[141] I. Chatterjee, M. J. Uren, S. Karboyan, A. Pooth, P. Moens, A. Banerjee, and M. Kuball, IEEE Trans. Electron Devices **64**, 977 (2017).

[142] H. -C. Chiu, S. -C. Chen, J. -W. Chiu, B. -H. Li, R. Xuan, C. -W. Hu, and K. -P. Hsueh, Journal of Vacuum Science & Technology B, Nanotechnology and Microelectronics: Materials, Processing, Measurement, and Phenomena **35**, 41205 (2017).

[143] S. -M. Koo and M. -S. Kang, Materials Research Bulletin **58**, 178 (2014).

[144] E. Arslan, S. Bütün, Y. Şafak, and E. Ozbay, Journal of Electronic Materials **39**, 2681 (2010).

[145] C. Mizue, Y. Hori, M. Miczek, and T. Hashizume, Jpn. J. Appl. Phys. **50**, 21001 (2011).

[146] C. Tang and J. Shi, Semicond. Sci. Technol. **29**, 125004 (2014).

[147] Y. Chen, K. Zhang, M. Cao, S. Zhao, J. Zhang, X. Ma, and Y. Hao, Appl. Phys. Lett. **104**, 153509 (2014).

[148] A. M. Cowley and S. M. Sze, J. Appl. Phys. **36**, 3212 (1965).

[149] D. Donoval, A. Chvála, R. Šramatý, J. Kováč, J. -F. Carlin, N. Grandjean, G. Pozzovivo, J. Kuzmík, D. Pogany, G. Strasser, and P. Kordoš, Appl. Phys. Lett. **96**, 223501 (2010).

[150] F. -C. Chiu, Advances in Materials Science and Engineering **2014**, 1 (2014).

[151] S. Yang, S. Huang, H. Chen, M. Schnee, Q. -T. Zhao, J. Schubert, and K. J. Chen, Appl. Phys. Lett. **99**, 182103 (2011).

[152] M. F. Romero, A. Jimenez, J. Miguel-Sanchez, A. F. Brana, F. G. Posada, R. Cuerdo, F. Calle, and E. Munoz, IEEE Electron Device Lett. **29**, 209 (2008).

[153] S. A. Awan and R. D. Gould, Thin Solid Films **423**, 267 (2003).

[154] R. M. Chu, Y. G. Zhou, K. J. Chen, and K. M. Lau, phys. stat. sol. (c) **0**, 2400 (2003).

[155] M. Zhao and X. -Y. Liu, Chinese Phys. Lett. **32**, 48501 (2015).

[156] H. Jiang, C. Liu, Y. Chen, X. Lu, C.W. Tang, and K. M. Lau, IEEE Trans. Electron Devices **64**, 832 (2017).

[157] Z. -Q. Fang, D. C. Look, X. -L. Wang, J. Han, F. A. Khan, and I. Adesida, Appl. Phys. Lett. **82**, 1562 (2003).

[158] S. Yang, C. Zhou, Q. Jiang, J. Lu, B. Huang, and K. J. Chen, Appl. Phys. Lett. **104**, 13504 (2014).

Publications

- **A. Fariza**, A. Lesnik, J. Bläsing, M.P. Hoffmann, F. Hörich, P. Veit, H. Witte, A. Dadgar, and A. Strittmatter, *On reduction of current leakage in GaN by carbon-doping,* Applied physics letters **109**, 212102 (2016)
- A. Lesnik, M.P. Hoffmann, **A. Fariza**, J. Bläsing, H. Witte, P. Veit, F. Hörich, C. Berger, J. Hennig, A. Dadgar, and A. Strittmatter, *Properties of C-doped GaN,* Phys. Status Solidi B **254**, 1600708 (2017)
- **A. Fariza**, A. Lesnik, S. Neugebauer, M. Wieneke, J. Hennig, J. Bläsing, H. Witte, A. Dadgar, and A. Strittmatter, *Leakage currents and Fermi-level shifts in GaN layers upon iron and carbon-doping,* Journal of applied physics **122**, 025704 (2017)

Conference contributions

- 28th DGKK workshop Illmenau, Germany. 5-6 December 2013, *Defect characterization in AlInN/AlN/GaN HEMT structures on Si(111),* Aqdas Fariza, Hartmut Witte, Jonas Hennig, Oliver Krumm, Jürgen Bläsing, Armin Dadgar, and Alois Krost
- DPG spring Meeting Dresden, Germany. 30 March -04 April 2014, *Defect characterization in AlInN/AlN/GaN HEMT structures on Si(111),* Aqdas Fariza, Hartmut Witte, Jonas Hennig, Oliver Krumm, Jürgen Bläsing, Armin Dadgar, and Alois Krost
- IWN Wroclaw, Poland. 24-29 August 2014, *Electrical properties of defects in AlInN/AlN/GaN HEMT structures on Si (111),* Aqdas Fariza, Hartmut Witte, Jonas Hennig, Martin Gottschalk, Martin Goldschmidt, Jürgen Bläsing, Armin Dadgar, and Alois Krost
- 29th DGKK workshop Magdeburg, Germany. 11-12 December 2014, *Impact of in-situ SiN passivation on AlInN/AlN/GaN HEMT structures on Si(111),* Aqdas Fariza, Hartmut Witte, Jonas Hennig, Martin Goldschmidt, Jürgen Bläsing, Armin Dadgar, and Andre Strittmatter
- DPG spring Meeting Berlin, Germany. 15-20 March 2015, *Thermal defect spectroscopy in AlInN/AlN/GaN heterostructures on Si(111),* Aqdas Fariza, Hartmut Witte, Jonas Hennig, Jürgen Bläsing, Armin Dadgar, and Andre Strittmatter
- DPG spring Meeting Regensburg, Germany. 5-11 March 2016, *Structural*

characterization and scanning surface potential microscopy (SSPM) of C-doped GaN layers on sapphire, Aqdas Fariza, Hartmut Witte, Andreas Lesnik, Jürgen Bläsing, Peter Veit, Armin Dadgar, and André Strittmatter

- 31st DGKK workshop in Duisburg, Germany. 8-9 December 2016, *Comparative study of surface properties in p-type, n-type, and semi-insulating GaN layers on Sapphire,* Aqdas Fariza, Andreas Lesnik, Silvio Neugebauer, Matthias Wieneke, Jürgen Bläsing, Hartmut Witte, Armin Dadgar, and André Strittmatter
- DPG spring Meeting Dresden, Germany. 19-24 March 2017, *Surface properties of p-type, n-type, and semi-insulating GaN layers on sapphire,* Aqdas Fariza, Andreas Lesnik, Silvio Neugebauer, Matthias Wieneke, Jürgen Bläsing, Hartmut Witte, Armin Dadgar, and André Strittmatter
- CSW 2017 Berlin, Germany. 14-18 May 2017, *Poster presentation: Surface properties of n-, p-, and semi-insulating GaN layers on sapphire,* Aqdas Fariza, Silvio Neugebauer, Andreas Lesnik, Matthias Wieneke, Jürgen Bläsing, Hartmut Witte, Armin Dadgar, and André Strittmatter
- 32nd DGKK workshop in Freiburg, Germany. 7-8 December 2017, *Comparison of C- and Fe- doped GaN buffer layers and HEMT structures,* Aqdas Fariza, Andreas Lesnik, Silvio Neugebauer, Matthias Wieneke, Seshagiri Rao Challa, Jürgen Bläsing, Hartmut Witte, Armin Dadgar, and André Strittmatter
- SPIE OPTO 2018 San Francisco, California United States. 27- January - 1 February 2018, *Leakage currents and Fermi-level shifts in C- and Fe-doped GaN,* Aqdas Fariza, Silvio Neugebauer, Andreas Lesnik, Matthias Wieneke, Jürgen Bläsing, Hartmut Witte, Armin Dadgar, and André Strittmatter

Eidestattliche Erklärung

Hiermit erkläre ich, dass ich die von mir eingereichte Dissertation zum dem Thema

Surface and electrical properties of GaN layers Impact on GaN/AlInN FETs

selbständig verfasst, nicht schon als Dissertation verwendet habe und die benutzten Hilfsmittel und Quellen vollständig angegeben wurden.

Weiterhin erkläre ich, dass ich weder diese noch eine andere Arbeit zur Erlangung des akademischen Grades doctor rerum naturalium (Dr. rer. nat.) an anderen Einrichtungen eingereicht habe.

Magdeburg, den. 07 Juni 2018

M.Sc. Aqdas Fariza